A Complete Portable and Low-Cost Micro-opto-fluidic Raman Spectroscopic Measurement and Characterization System

by

Emily E. Storey

A thesis submitted in conformity with the requirements
for the degree of Master of Applied Science
Graduate Department of Electrical and Computer Engineering
University of Toronto

Abstract

A Complete Portable and Low-Cost Micro-opto-fluidic Raman Spectroscopic Measurement and Characterization System

Emily E. Storey
Master of Applied Science
Graduate Department of Electrical and Computer Engineering
University of Toronto
2019

There is a glaring, unmet demand for a healthcare analysis method which is non-invasive, rapid, portable, and flexible, to provide consistent results for novice and expert users alike. Such a technique would facilitate access to health solutions in rural settlements, where population health can suffer due to limited specialized facilities. Raman spectroscopy of biological fluids is ideal for this task. Widespread adoption requires a robust collection system and a model which can withstand routine spectrum variability, but current methods place the end-user in charge of these remedies.

In this thesis we present a point-of-care system for fluidic analysis using Raman which eliminates sample preparation and optimizes analysis, independent of end-user proficiency. A micro-opto-fluidic device greatly enhances the Raman signal, and accompanying machine-learning suite optimizes preprocessing methods to compensate for routine signal variation. We demonstrate performance on artificial human tears and whole-blood, achieving user-independent predictive concentration precision below 500 μM.

Acknowledgements

My years at the University of Toronto have been a phenomenal learning experience. I must express my deepest gratitude to my advisor, Professor Helmy. Thank you for giving me a space and time to learn, explore, and create something new.

A profound thank you goes out to everyone in the Helmy group, past and present, and all of the facilities staff at Toronto Nanofabrication Center. Thank you for listening, teaching, and helping to navigate the finer details of academic research.

Finally, my partner Robert. For making me eat when I forget. For making me laugh when I am ready to cry. For never letting me give up. I love you.

Contents

List of Publications and Conference Presentations

Journal Publications

[1] Emily E. Storey and Amr S. Helmy. Optimized Pre-processing and Machine Learning for Quantitative Raman Spectroscopy in Biology. *Journal of Raman Spectroscopy*, 2019. Accepted for publication 3 March 2019

[2] Emily E. Storey, Duxuan X. Wu, and Amr S. Helmy. Point-Of-Care Noninvasive Biofluid Diagnostics using Raman. 2019. In Preparation to Submit on or before 16 April 2019

International Conferences

[3] Emily E Storey, Manuchehr Ebrahimi, Basil G Eleftheriades, Bhargava Ravoori, Steven Rutledge, Tuyen Tran, Marie Tripp, and Amr S Helmy. Semiconductor Contaminant Quantification via Raman Spectroscopy. In *Semiconductor Research Corporation (SRC) TechCon 2017*, Austin, Texas, USA, 2017

[4] Emily E Storey, Duxuan X Wu, and Amr S Helmy. Optofluidic Analysis System with Machine Learning for User-Independent Biofluid Diagnostics. In *Conference on Lasers and Electro-Optics (CLEO) 2019*, San Jose, California, USA, 2019. Accepted to present in May 2019

Local Conferences

[5] Emily E Storey, Duxuan X. Wu, and Amr S Helmy. Enhanced Raman Analysis of Biofluids on Microfluidic Waveguides on Chip. In *Ontario Networking Event (ONE) in Biophysics 2018*, University of Toronto Mississauga, Ontario, Canada, 2018

List of Tables

List of Figures

Chapter 1

Introduction

1.1 Motivation

In this thesis we seek to promote access to a reliable healthcare diagnostics platform which boasts three key advantages over current methods:

1. Minimizes operator expertise for sample preparation and interpretation.
2. Maximizes patient comfort and compliance.
3. Sufficiently portable and cost-effective for widespread public adoption.

Glucose monitoring excellently illustrates the public need for this system. Reliable and routine measurements of blood glucose concentration is essential for diabetes monitoring and facilitating this process is the source of extensive research [6, 7]. Tears offer an attractive alternative for routine glucose monitoring compared to current methods. Finger-pricking is the traditional standard for blood glucose concentration determination, but it is invasive and uncomfortable for the patient. Tears, on the other hand, can be collected non-invasively and are continuously available compared to some other biofluids. Most importantly, correlation has been demonstrated between blood and tear glucose levels which validates their potential [8]. Non-invasive glucose monitoring has great potential impact; worldwide more than 400 million persons suffer from diabetes and nearly 4 million deaths were directly or indirectly attributed to it in 2012 [9]. Disease management can be further complicated by a lack of affordable treatment options. Diabetes deaths disproportionately affect persons of lower income which can place families and local health-care facilities under great financial strain, further fueling the need for a low-cost non-invasive and reliable diagnostic device [9].

Raman spectroscopy is an ideal tool to accomplish the nondestructive analysis of fluids. It has high chemical specificity and requires no physical interaction with the sample, though several innate drawbacks hamper its widespread adoption [10]. The phenomenon occurs with a frequency at least six orders of magnitude lower than its counterpart, elastic Rayleigh scattering, which manifests as a faint Raman signal highly subject to obstruction by noise or fluorescence [11]. Aqueous samples suffer in particular due to lower density of molecules to scatter the excitation laser. A high laser power may be employed to overcome these signal issues, however this may cause samples to heat or evaporate which alters the Raman signature from that which we wish to observe.

This thesis is motivated by the lack of available resources to enhance and facilitate the collection of Raman spectra from aqueous samples, with a focus on biological applications. Many techniques which

currently exist are destructive, expensive to implement, and require significant operator training which discourages widespread adoption. In this work we report for the first time a non-invasive physiological monitoring system; our methods greatly extend the sensitivity of Raman in biological fluids for mobile healthcare diagnostics.

1.2 Summary of Current Characterization Techniques

On-site rapid and routine health monitoring which maximizes patient comfort is becoming increasingly crucial in medical analysis and diagnostics. Biofluids such as urine and whole-blood are prime candidates for this task as they can generally be collected non-invasively and with minimal skill. Recent research has shown urine's potential for prostate cancer detection and diagnosis, allowing the patient to avoid an uncomfortable rectal examination or biopsy [12]. Blood is a valuable diagnostic tool which has the potential to reveal biomarkers of acute myocardial infarctions, where rapid diagnosis is crucial [13]. Unfortunately traditional diagnostics require clinical laboratory tests which often necessitate multiple samples each with unique treatments for different tests, ruining the sample for further analysis [7]. If a patient falls ill and these facilities are unavailable, the quality of treatment they receive will suffer considerably. It is in the interest of patient comfort and survival that an analysis method is available which hastens results and minimizes the amount of invasive sample collection.

A fluidic Raman constituent analysis system is not bound to a single purpose; so long as the device and fluid are chemically compatible and the sample is Raman active, this technique can be adapted to suit an dazzling array of applications. This thesis will focus on biological samples though it is important to acknowledge that the work could equally impact environmental water monitoring, manufacturing of chemicals and consumables, or industrial quality control. Industrial manufacturing has a rising demand for contaminant detection and monitoring, particularly in the semiconductor field where yield and performance can be gravely affected by impurities. Properties such as strain or defects in the crystal lattice can have a profound impact on device performance, but be difficult to characterize due to their size [14]. As devices continue to shrink it becomes increasingly crucial to characterize defects on a comparable scale and Raman's ability to non-destructively inspect the physical and chemical characteristics of a sample has led to a great amount of progress in the field. Tip-enhanced Raman spectroscopy, for example, couples laser light to a metallic tip in order to increase the likelihood of Raman scattering in a confined region. This method has enabled spatial resolution below 10 nm, whereas traditional Raman measurements are bound by the diffraction limit (typically on the order of micrometers) [14, 15]. A second technique to ensure high quality semiconductor devices is to perform preemptive monitoring of processing liquids for contaminants which may deposit on to the device and affect its yield. Semiconductor manufacturing often requires the use of strong acids which necessitate careful handling by trained personnel and a method which can probe these fluids in a safe manner would be a great benefit to operator safety.

1.3 Objective

For this thesis we propose a comprehensive method which enhances fluidic Raman spectra using liquid-core waveguides (LCWs) in order to detect, identify, and quantify trace analytes and contaminants. This is accomplished in two parts, using both hardware and software components.

Hardware consists of a micro-opto-fluidic device to enhance the Raman spectrum, contain the sample from its environment, and ensure optimal optical coupling to the excitation laser. A set of custom-designed 3D-printed parts accompanies this device and allows it to be readily used on any standard microscope stage. Our low-cost dual-syringe pump provides sample recirculation to mitigate damaging heating effects, and enables sample recovery with minimal reliance on laboratory equipment. Optofluidic devices are well-studied in open literature as individual components of larger analysis systems. We strive to overcome the requirement for a large system by designing a device which can be manufactured and operated with variable expertise, and as a stand-alone unit which relies minimally on external sample processing facilities.

Software consists of a custom spectrum analysis graphical user interface (GUI). Novel methods are introduced which minimize user expertise required to perform meaningful quantitative concentration predictions. A series of statistical F-tests optimize the preprocessing methods and allow the operator to obtain the most accurate analysis, independent of their experience with Raman spectroscopy. We validate these techniques using biofluid phantom solutions designed to mimic human tears and whole human blood. These fluids are of paramount importance to diagnostics and monitoring of diabetes, infectious diseases, degenerative diseases, conjunctivitis, and a wealth of others [16–21]. In these experiments we demonstrate the applicability of our system to analyze and facilitate diagnostics of a wide breadth of biofluids, from the optically transparent to the highly turbid.

1.4 Thesis Organization

This thesis is divided into 8 chapters.

Chapter

2 An introduction to Raman spectroscopy. The theory of Raman scattering is described using both classical and quantum mechanics, and common enhancement methods in current literature will be discussed with a focus on biological applications.

3 A discussion of the applicability of Raman to detecting diagnostically-relevant analytes in particular biofluids. We introduce our micro-opto-fluidic measurement system for Raman spectrum enhancement.

4 Predictive diagnostics using principal component analysis (PCA) will be discussed. We present our novel algorithm to statistically-optimize spectra for predictive diagnostics.

5 Expanding access to analytical techniques with a custom-built GUI which facilitates non-expert operators to confidently perform meaningful analysis

6 A presentation of the full process of microfluidic device fabrication, sample spectrum collection, and analysis using the techniques we have developed and presented in chapters 3 through 5.

7 Experimental demonstration of the performance achieved by our statistical algorithm, and specific diagnostic potential at the levels of precision which we obtain.

8 Broad implications and future directions of this measurement system.

Chapter 2

Raman Spectroscopy

Four classes of events can result when a ray of light meets an interface, which are illustrated in figure 2.1. These cases are not mutually exclusive [22]. If the ray is incident on a substance which is fully optically transparent then it is transmitted through the first boundary of the substance and out the second interface with no loss of intensity. When the substance is not fully optically transparent the ray is reflected back along the plane of incidence. Absorption occurs when there is an energy exchange between the substance and the ray of light, either partially or fully reducing its intensity. Scattering involves the absorption and re-emission of all or part of the ray's energy. This thesis is devoted to scattering, of which there are two distinct subsets: elastic (Rayleigh) or inelastic (Raman).

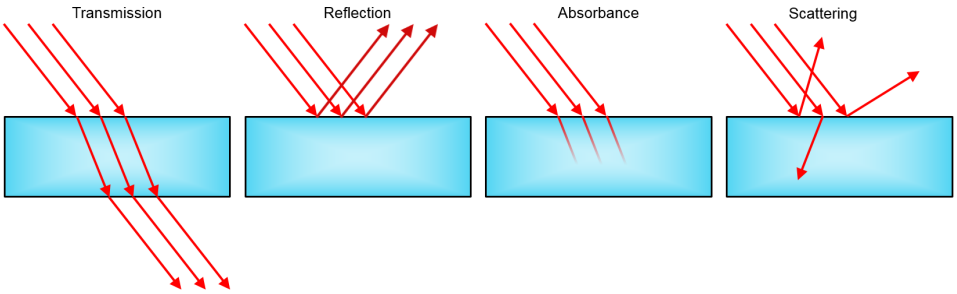

Figure 2.1: Light-matter interaction events.

The most probable outcome in a scattering interaction is elastic, with involved photons suffering no loss or gain in energy. Approximately one time in ten million, however, an energy exchange occurs which alters the configuration of occupied energy levels in the molecule and the frequency of outgoing radiation. This low probability of occurrence manifests as a very weak Raman signal. Raman scattering offers a unique non-destructive method to gain insight into a material's structure and composition, but its faint signal can be problematic. This chapter will provide an introduction to Raman Scattering, explain its limitations, and introduce some methods to overcome them.

2.1 Theory

2.1.1 Classical Theory of Raman Scattering

Classical physics can provide an approximate explanation for Raman scattering at the macroscopic level [23]. To obtain a model for this interaction, we need to consider the oscillations of both the electromagnetic field and the molecule or lattice.

An electromagnetic wave's electric field $\mathbf{E}$ can be expressed as a function of time using equation 2.1, and the molecular charges within a substance upon which this field is incident will experience an induced dipole moment $\mathbf{p}$, given in equation 2.2.

$$\mathbf{E} = \mathbf{E}_0 \cos(2\pi\nu_i t) \tag{2.1}$$

$$\mathbf{p} = \alpha \cdot \mathbf{E} \tag{2.2}$$

$\mathbf{E}$: Electric field
$\mathbf{E}_0$: Amplitude of electric field
$\mathbf{p}$: Dipole moment
α : Polarizability tensor
ν_i : Frequency of propagation of the electric field
t : time

The factor of proportionality α in equation 2.2 is the molecule's polarizability tensor, which quantifies the displacement potential of a charge distribution. The light which scatters due to this interaction will contain three distinct frequencies [24]. The value which α takes is a function of bond geometry, so we must consider atomic structure and its nuclear displacement in order to derive these frequencies [25].

Nuclear displacement in a simple molecular system may be modelled as a harmonic oscillator, as in equation 2.3.

$$\mathbf{Q} = Q_0 \cos(2\pi\nu_n t) \tag{2.3}$$

$\mathbf{Q}$: Nuclear displacement
Q_0 : Amplitude of nuclear oscillation
ν_n : Frequency of nuclear oscillation

To derive the interaction frequencies we must first expand the polarizability tensor around $\mathbf{Q}$ using a Taylor's series, where the subscript 0 denotes the system's equilibrium position.

$$\begin{aligned} \alpha &= \alpha_0 + \left(\frac{\partial\alpha}{\partial\mathbf{Q}}\right)_0 \mathbf{Q} + \frac{1}{2}\left(\frac{\partial^2\alpha}{\partial\mathbf{Q}^2}\right)_0 \mathbf{Q}^2 + \dots \\ &\approx \alpha_0 + \alpha'\mathbf{Q} \end{aligned} \tag{2.4}$$

Substituting equations 2.1, 2.3, and 2.4 into 2.2 and using trigonometric identities, we obtain equation 2.5 which contains three distinct frequencies as needed.

$$\begin{aligned}\mathbf{p} &= \alpha \cdot \mathbf{E} \\ &= \left(\alpha_0 + \left(\frac{\partial \alpha}{\partial \mathbf{Q}}\right)_0 \mathbf{Q}\right) \cdot (\mathbf{E}_0 \cos(2\pi\nu_i t)) \\ &= \alpha_0 \mathbf{E}_0 \cos(2\pi\nu_i t) + \left(\frac{\partial \alpha}{\partial \mathbf{Q}}\right)_0 Q_0 \cos(2\pi\nu_n t)\mathbf{E}_0 \cos(2\pi\nu_i t) \\ &= \alpha_0 \mathbf{E}_0 \cos(2\pi\nu_i t) + \frac{1}{2}\left(\frac{\partial \alpha}{\partial \mathbf{Q}}\right)_0 Q_0 \mathbf{E}_0 \left[\cos(2\pi(\nu_i + \nu_n)t) + \cos(2\pi(\nu_i - \nu_n)t)\right]\end{aligned} \tag{2.5}$$

The frequencies in equation 2.5 correspond to three possible scattering events when an electromagnetic wave and molecule meet. Rayleigh scattering corresponds to ν_i. Raman scattering is evident in the terms containing frequency shifts, $(\nu_i + \nu_n)$ and $(\nu_i - \nu_n)$. These energy changes, designated anti-Stokes and Stokes respectively, are depicted in figure 2.2 in the spectrum of a silicon wafer. Energy shifts in Raman spectroscopy are conventionally denoted in units of wavenumbers, defined in equation 2.6 in relation to wavelength:

$$w = \left(\frac{1}{\lambda_i} - \frac{1}{\lambda_n}\right)\left(\frac{10^7 \text{nm}}{\text{cm}}\right) \tag{2.6}$$

w : Wavenumber shift (cm^{-1})
λ_i : Wavelength of excitation laser (nm)
λ_n : Wavelength of scattered light (nm)

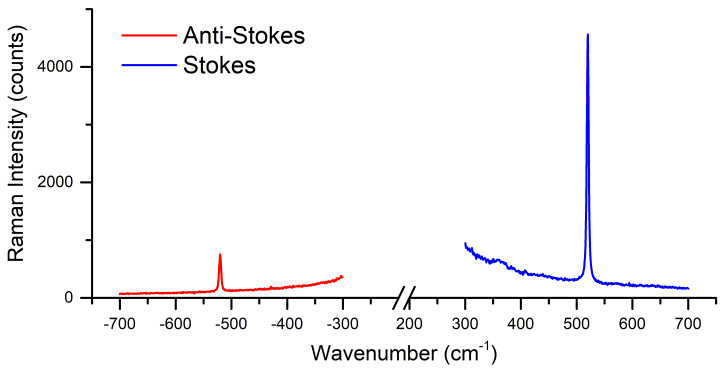

Figure 2.2: Raman spectra of a silicon wafer, showing both Stokes and anti-Stokes lines of the silicon mode at $\pm$ 520 cm^{-1}.

2.1.2 Quasi-Quantum Theory of Raman Scattering

The classical theory of Raman scattering is not fully descriptive; quantum mechanics is required for a complete characterization of the phenomenon. A molecule's rotational frequencies are not derived in the classical approach, and neither is the relationship between α and the frequency of incident light [26]. Moreover, a description is needed which explains shifts in Raman modes as a result of strain or thermal excitation [24]. A quasi-quantum mechanical treatment demonstrates the relationship between Raman modes and occupied electronic energy states.

An extensive and thorough quantum-mechanical description of Raman scattering can be found in literature; the basics can be understood with an energy transfer model [26]. Here we model an electromagnetic wave as a collection of photons, each with a discrete energy given by equation 2.7:

$$E = h\nu_i \tag{2.7}$$

E : Energy of photon
h : Planck's constant
ν_i : Incident light frequency

In classical mechanics an electromagnetic field is expressed by a plane wave as in equation 2.1, whereby in quantum mechanics the plane wave is a collection of quantized photons whose energies are described by equation 2.7. In a similar manner the nuclear displacements in a molecular lattice take a plane wave form in classical mechanics (equation 2.3), whereas their normal modes of vibration are discrete in quantum mechanics. These quanta of vibrational lattice modes are called phonons and have their energies described by equation 2.8.

$$E = h\nu_n \tag{2.8}$$

E : Energy of phonon
ν_n : Phonon vibration frequency

Energy conservation dictates that the sum of energies prior to and following the light-matter-interaction must be equal. Prior to the interaction the electromagnetic wave contains n_i photons of frequency ν_i, where ν_i is not an allowed value for ν_n. We denote the initial energy state of the molecule as E_i. Following the interaction there is one fewer photon with frequency ν_i, and the creation of a scattered photon of frequency ν_s. The molecule must shift to a new energy state in order to balance this equation and satisfy energy conservation.

$$\begin{aligned} n_i h\nu_i + E_i &= (n_i - 1)h\nu_i + h\nu_s + E_i + \Delta E \\ n_i h\nu_i - (n_i - 1)h\nu_i - h\nu_s &= \Delta E \\ h(\nu_i - \nu_s) &= \Delta E \end{aligned} \tag{2.9}$$

The frequency of ΔE must correspond to a transition to a phonon mode (equation 2.8) in order for a Raman scattering event to occur. When there is no equality between equations 2.8 and 2.9, Rayleigh scattering results and the system remains unperturbed. These three possibilities for electronic transition are illustrated in figure 2.3. The frequency of scattered light increases in the anti-Stokes case as energy is transferred from the lattice, and conversely in Stokes scattering there is a decrease in frequency of scattered light as energy is transferred to the lattice.

2.2 Methods of Spectrum Enhancement for Aqueous Samples

Raman spectroscopy in its native form produces a faint signal due to the low frequency of Raman scattering relative to Rayleigh. This effect is pronounced when there is a lower density of molecules to

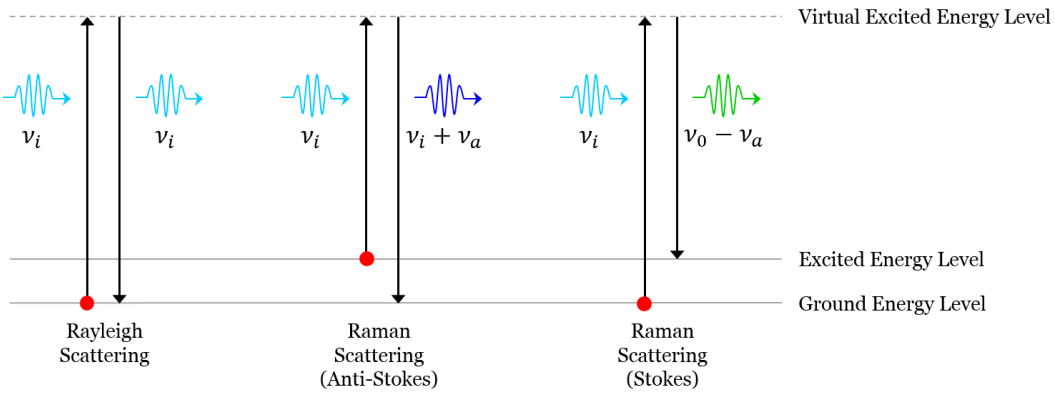

Figure 2.3: Energy levels and scattered light frequencies in Raman and Rayleigh scattering

scatter the incident light. The Raman signal may be reduced even further as a function of the molecular Raman scattering cross-section, which describes the scattering efficiency of the scattering particle [27]. Many techniques are currently available to enhance Raman spectroscopy. Here we will discuss these methods, with a focus on the biological context.

2.2.1 Surface Enhanced Raman Spectroscopy

Compared to traditional Raman spectroscopy, surface-enhanced Raman spectroscopy (SERS) can provide an enhancement up to a factor of approximately 10^6. The sample is brought into contact with a substrate which meets a specific criteria; typically a roughened metal surface. The technique is ideal for analyzing specific molecules or samples which can form a thin film on the substrate. These features make SERS well-suited to aqueous samples, and multiple studies have demonstrated its ability to quantify human biofluids [28]. Two separate factors contribute to the SERS effect: a chemical and an electric field enhancement [23].

Up to 100× enhancement of the Raman signal is due to chemical interactions of the sample and metal surface. A thin film on the substrate can result in increased density of scattering centers close to the surface which increases the Raman signal. In addition, a bond may be created between the substrate and analyte that creates a surface species which increases the sample's polarizability [11]. The remaining factor of 10^4 which SERS provides over conventional Raman is attributed to an enhancement of the electromagnetic field in the vicinity of nanoscale surface features. This effect is due to electrons of the metal substrate oscillating in phase with the incident laser radiation via resonance with surface plasmon frequencies [29]. Since the Raman signal is proportional to the strength of the electromagnetic field (equation 2.5), the addition of this in-phase oscillation enhances the Raman signal. This condition requires that the substrate and incident frequency be paired appropriately.

SERS provides a sizeable enhancement to the Raman signal, but requires significant preparation. The substrates themselves must be carefully prepared to ensure they are pure, their surfaces free from contamination, and that there is sufficient adhesion between the substrate and analyte. Optimal SERS substrates are often unstable over long periods of time due to surface oxidation [11].

2.2.2 Drop-Coating Deposition Raman Spectroscopy

Drop-coating deposition Raman spectroscopy (DCDRS) begins with a small volume of fluid deposited on to a substrate. The solvent is evaporated and Raman spectroscopy is performed on the residual precipitate [30]. DCDRS is an attractive technique for Raman spectroscopy of biofluids. Proteins in particular remain hydrated through DCDRS, producing Raman spectra which resemble aqueous solutions rather than the spectrum of a crystalline or denatured sample [31]. This is not universally applicable, however, as some smaller molecules may appear in the spectrum as their saturated forms, and some as crystalline.

DCDRS has been shown to produce a highly reproducible spectrum which remain stable for several weeks [30]. This can pose a great benefit for prolonged studies. The structures left behind following evaporation may also exhibit unique spatial variability, which can provide additional diagnostic information. Figure 2.4 illustrates the stark contrast between blood samples from healthy and diseased patients [32]. Common features include "coffee-rings", cracking, and crystalline formations. Coffee-ring features result due to capillary flow pushing suspended particles towards the periphery as the droplet dries. Cracks and crystals can result from different phase changes occurring simultaneously in complex fluids, where the drying fluid becomes a solid or a gel [33]. The presence of these physical features is dependent on the sample's composition, so they can be a useful diagnostic tool to complement Raman spectroscopy.

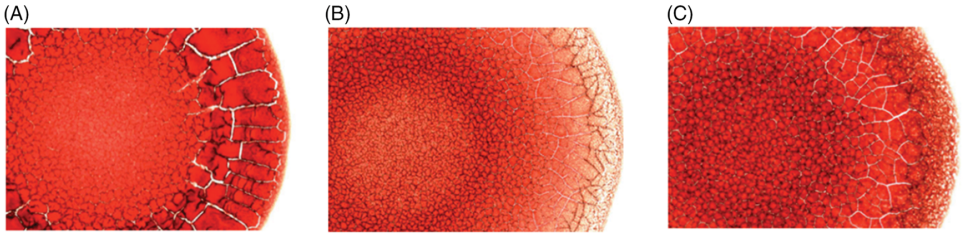

Figure 2.4: Dried blood drop patterns from patients who are (A) healthy, or diagnosed with (B) anemia or (C) hyperlipideamia. Distinct drying patterns are evident in (B) and (C) which differentiate them from a healthy blood sample. Reproduced with permission from [32].

Despite the benefits, DCDRS remains a destructive technique which requires trained personnel and an extended period of sample preparation. Resulting spectra do not reflect analyte concentration in the original fluid which makes quantitative analysis challenging. Further to this point, specific solutes may only be deposited in a given region of the droplet, hindering their detection. Physical patterns can vary significantly unless strict drying conditions are maintained. Figure 2.5 shows the drastic variation in patterns that can occur in a blood droplet dried under different levels of relative humidity.

2.2.3 Optofluidic Raman Spectroscopy

SERS and DCDRS provide significant enhancement to a conventional fluidic Raman signal, but both destroy the sample. In biological situations it can be crucial that this does not occur. Optofluidics takes advantage of differences in indices of refraction between the sample and some surrounding cladding materials [35]. Confining the aqueous sample inside the cladding material allows total internal reflection (TIR) to occur, which increases the total volume of laser-sample interaction. This configuration gives a great advantage in that the sample remains unaltered by reagents, and can be recovered after analysis.

A detailed derivation of the conditions required for an optofluidic waveguide will be covered in section

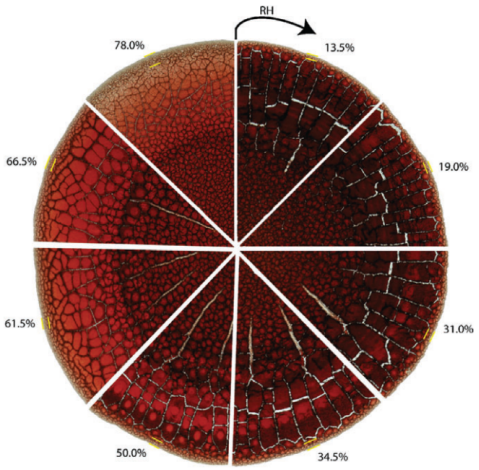

Figure 2.5: Variation in the drying patterns of a blood droplet under different levels of relative humidity (RH). Reprinted from [34], with permission from Elsevier.

2.3. In brief, a low-refractive-index material surrounds the fluidic sample which enables TIR if laser light is coupled into the core within a certain acceptance angle. Three types of materials are commonly-used, pictured in figure 2.6 from left to right: air, Teflon capillary tubes (TCTs), and hollow-core photonic crystal fibers (HC-PCFs).

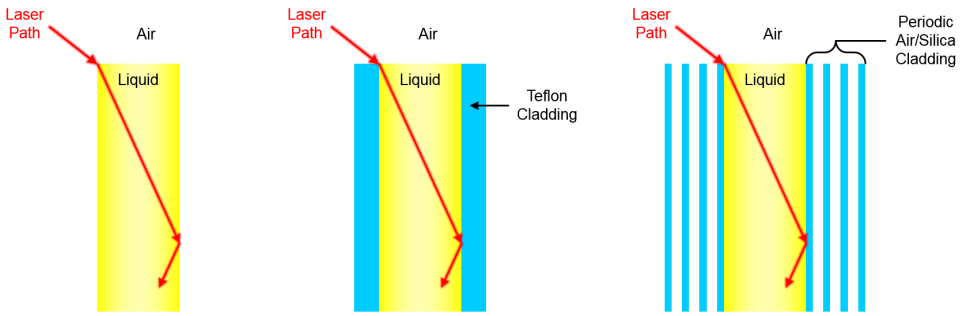

Figure 2.6: Optofluidic cladding materials. From left to right: air cladding, Teflon capillary tube (TCT), and hollow-core photonic crystal fiber (HC-PCF).

Raman enhancement is proportional to the difference in index of refraction between the sample and cladding, so we desire the lowest-index cladding material. An air cladding ($n = 1.0$) can be achieved by exciting lengthwise down a laminar water-jet, however the stream cannot exceed a critical length before breaking up [36]. This configuration also poses potential for evaporation and environmental contamination. HC-PCFs have the next lowest index of refraction ($n < 1.2$), followed by TCTs ($n = 1.29 - 1.31$) [37]. In this thesis we have investigated both HC-PCFs and TCTs for on-chip Raman enhancement.

2.3 Liquid Core Waveguide Spectroscopy

LCWs rely on the appropriate pairing of a liquid core and outer cladding whose indices of refraction ensure TIR within the core. This section will derive the conditions for this phenomena to occur, and

methods to optimize the signal.

A ray of light which is transmitted from one material to another is bent along the normal axis of the interface. This bending is the result of a requirement that the ray's wavefronts remain continuous at the boundary [22]. In figure 2.7 we illustrate a ray travelling from the interior of waveguide to the cladding, respectfully denoted with subscripts Co and Cl. The new direction is defined according to Snell's law in equation 2.10

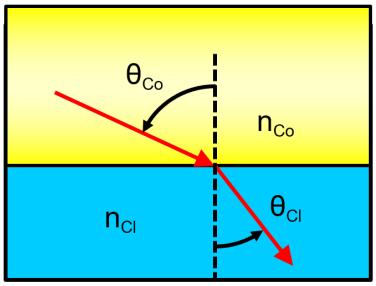

Figure 2.7: A beam of light, indicated with a red arrow, travelling across the interface from the core of a waveguide (Co) to the cladding material (Cl). The beam is bent along the normal axis as a function of its angle of incidence θ and the material indices of refraction n.

$$n_{\mathrm{Co}} \sin(\theta_{\mathrm{Co}}) = n_{\mathrm{Cl}} \sin(\theta_{\mathrm{Cl}}) \tag{2.10}$$

n_{Co} : Index of refraction of liquid core
θ_{Co} : Angle of incidence within the core
n_{Cl} : Index of refraction of cladding material
θ_{Cl} : Angle of transmittance into the cladding

Rearranging equation 2.10 to solve for θ_{Cl}, we find that a case may arrive in which there is no solution. If $n_{\mathrm{Cl}} < n_{\mathrm{Co}}$, it is possible that the solution for $\sin(\theta_{\mathrm{Cl}})$ requires a value greater than 1. The ray is not transmitted through the cladding in this case, but rather reflects off the interface back into the core. We define the angle at which this begins to occur and $\sin(\theta_{\mathrm{c}}) = 1$ as the critical angle.

$$\sin(\theta_{\mathrm{Cr}}) = \frac{n_{\mathrm{Cl}}}{n_{\mathrm{Co}}} \tag{2.11}$$

θ_{Cr} : Critical angle of incidence within the core

A ray of light entering and traveling within a LCW will interact with three different media (external environment, fluidic sample, cladding material), illustrated in figure 2.8. This configuration allows us to define the maximum acceptance angle which will satisfy the conditions for TIR within the waveguide.

To derive the maximum value for θ_{Ac} and the LCW's numerical aperture (NA), we define θ_{Cr} in terms of θ_{Co} and substitute equations 2.11 and 2.12 into Snell's law at the interface between the core and the external environment:

$$\theta_{\mathrm{Cr}} = \frac{\pi}{2} - \theta_{\mathrm{Co}} \tag{2.12}$$

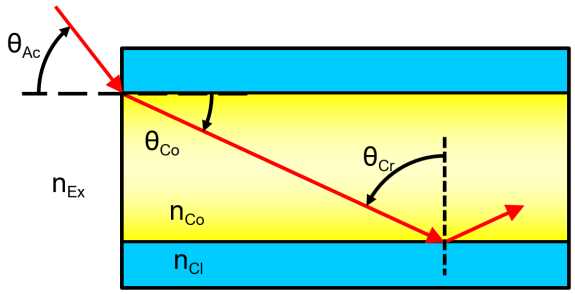

Figure 2.8: Total internal reflection within an optofluidic fiber.

$$\begin{aligned} n_{\mathrm{Ex}} \sin(\theta_{\mathrm{Ac}}) &= n_{\mathrm{Co}} \sin(\theta_{\mathrm{Co}}) \\ &= n_{\mathrm{Co}} \sqrt{1 - \cos^2(\theta_{\mathrm{Co}})} \\ &= \sqrt{n_{\mathrm{Co}}^2 - n_{\mathrm{Co}}^2 \sin^2(\theta_{\mathrm{Cr}})} \\ &= \sqrt{n_{\mathrm{Co}}^2 - n_{\mathrm{Co}}^2 (n_{\mathrm{Cl}}/n_{\mathrm{Co}})^2} \\ &= \sqrt{n_{\mathrm{Co}}^2 - n_{\mathrm{Cl}}^2} \\ &= \mathrm{NA} \end{aligned} \tag{2.13}$$

θ_{Co} : Angle of transmittance within the core
θ_{Ac} : Maximum acceptance angle to preserve TIR
n_{Ex} : Index of refraction of the external environment
NA : Numerical aperture of the fiber

Equation 2.13 defines the maximum acceptance angle of a LCW as a function of the indices of refraction, and is a necessary consideration for Raman signal enhancement with LCWs. In order to maximize the Raman signal, it is crucial to pair the waveguide with an objective whose NA is appropriate.

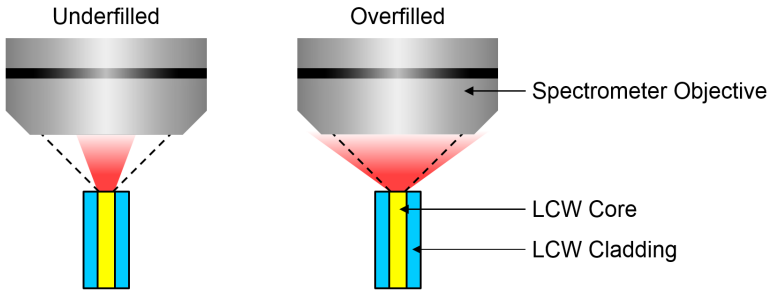

Figure 2.9: Pairing between numerical apertures of a spectrometer objective and a liquid-core waveguide (LCW). Objective aperture boundary is indicated by a dotted black line, and the waveguide aperture region is indicated by a shaded red region.

Figure 2.9 depicts the two extremes which may occur if an LCW and objective are not properly matched. On the left the LCW has a smaller NA than the objective. Some of the excitation light is not coupled into the waveguide and available for Raman scattering. The resulting signal will suffer a loss of intensity as the detector is underfilled. On the right the LCW has a larger NA than the objective. All excitation light is successfully coupled into the waveguide, but the back-scattered signal cannot all be

captured and a loss of intensity occurs as the detector is overfilled.

LCWs greatly increase the interaction length between excitation source and sample, amplifying the Raman signal. The magnitude of this enhancement is determined by the configuration in which the scattered light is collected. Six possible geometries are illustrated on the left of figure 2.10, with their corresponding relative Raman enhancements on the right. Intensities are given in units of cell length, also sometimes referred to as attenuation length, which is the inverse of the waveguide loss coefficient. These values for HC-PCFs and TCTs are listed in table 2.1.

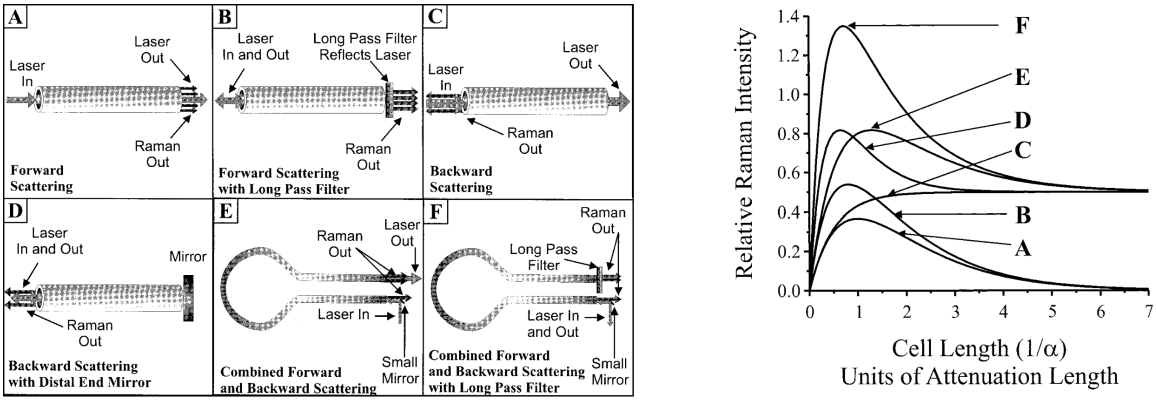

Figure 2.10: Left: Scattering geometries for liquid-core waveguides (LCWs). Right: Relative Raman scattering enhancements for each corresponding geometry [38].

Table 2.1: Hollow-core waveguide attenuation lengths [39]

Waveguide	**Attenuation Length** (cm)
TCT	144
PCF	267

The in-house spectrometer on which the work in this thesis was performed is configured to excite and collect Raman scattered light from the same objective. A full schematic is included in section 2.4. The simplest LCW geometry to implement in this configuration is back-scattering, labeled item **C** in figure 2.10. This arrangement allows us to achieve a Raman scattering intensity according to equation 2.14 [38].

$$I = P_o \rho \sigma \pi (\mathrm{NA}) \left(\frac{1 - e^{-2\alpha L}}{2\alpha} \right) \tag{2.14}$$

P_o : Laser power
ρ : Raman scattering cross-section
σ : Number of scattering centers per unit volume
α : Waveguide loss coefficient
L : Waveguide length

From equations 2.14 and 2.13 it is evident that Raman enhancement can be achieved in different ways depending on the specimen's qualities or needs. A highly-turbid sample such a whole blood will have

a shorter optical penetration depth due to its high scattering coefficient, so it may not be possible to enhance this spectrum by elongating the waveguide [40]. Delicate and heat-sensitive samples may suffer damage if an attempt is made to enhance the spectrum by increasing laser power. Nevertheless these spectra could still be amplified by ensuring a sufficient refractive index contrast between the sample and the environment.

2.4 Spectrometer Setup & Operation

All Raman measurements in this thesis are collected on a Horiba Jobin Yvon LabRam HR800 spectrometer. Figure 2.11 depicts the optical setup. Control of the density filters, confocal hole diameter, and grating switching and operation is automated through an accompanying software package (LabSpec version 5.78.24). Switching the laser, excitation-line filter(s), and objective lenses is accomplished manually.

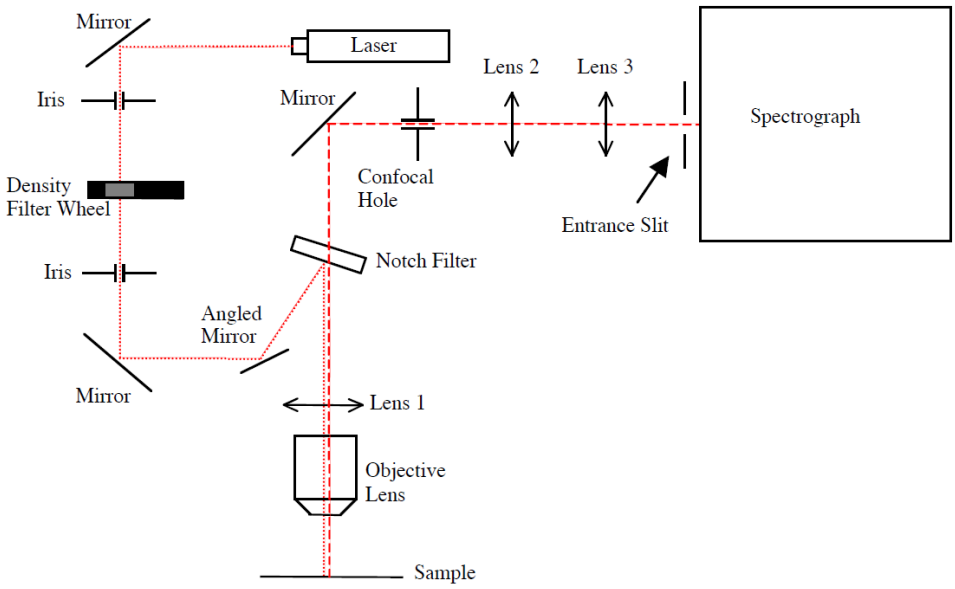

Figure 2.11: Horiba LabRAM HR800 Spectrometer Setup [41].

Laser

The spectrometer is equipped with two lasers. An internal Helium Neon laser of 20 mW, centered at 632.817 nm. An additional 200 mW diode laser, centered at 785 nm, is coupled externally into the spectrometer.

Density Filters

An adjustable density filter wheel with available optical density (OD) values of 0.3, 0.6, 1, 2, 3, 4. Output laser power (P_{out}) is given as a function of the input laser power (P_{in}) in equation 2.15.

$$P_{out} = P_{in} 10^{-\mathrm{OD}} \tag{2.15}$$

Objective Lenses

Four Olympus M Plan achromat objective lenses are equipped for optical alignment, coupling the excitation laser, and collecting back-scattered light from the sample. Available magnifications and their respective NAs and working distances are listed in table 2.2.

Table 2.2: Objective lenses equipped on the in-house Horiba Raman spectrometer.

Magnification	Numerical Aperture	Working Distance (mm)
10×	0.25	10.6
20×	0.40	1.2
100×	0.80	2

Filter

A holographic edge filter excludes the 633 nm interal laser line. Drop-off Stokes edge is <120 cm^{-1}. A notch filter excludes the 785 nm external laser line, allowing us to collect both Stokes and Anti-Stokes Raman modes using this wavelength.

Confocal Hole

Adjustable from 0 to 1103 μm. A confocal pinhole increases spatial discrimination by restricting the focal volume. Light originating shallower or deeper will come to focus before or after the pinhole and can be blocked from reaching the detector.

Spectrograph

An asymmetric Czerny-Turner spectrograph, 800mm focal length, optimized for flat-field. Two gratings are equipped, 600 lines/mm and 1800 lines/mm, which separates the back-scattered light into a spectrum of frequencies.

Detector

Silicon air-cooled CCD, 1024 $\times$ 256 pixels, each of 26 μm.

Chapter 3

Biological Analysis

Continuous advancement in science and medicine is strongly coupled to an ongoing desire for increased sensitivity and specificity in the detection, identification, and quantification of biofluids. These fluids include urine, tears, blood, sweat, and saliva. They can provide a wealth of information about a patient's health and most of them can be collected non-invasively. They are valuable for rapid diagnostics or monitoring while simultaneously maximizing patient comfort by minimizing invasive sample collection.

As an illustrative example, consider a toddler who has been brought to a remote urgent care clinic. The child is ill after ingesting something, but their guardian is not certain what they consumed. It is crucial in this situation that medical staff be able to detect the presence of a toxin, and it is generally preferable to do this with as little discomfort to the child as possible. Responders must be able to quickly bring a tool to the child which can rapidly identify what was ingested and at what level, in order to guide the appropriate course of treatment. Remote clinics often lack significant funding and specialized personnel, so we desire a method which can achieve this with as little cost and reliance on trained operators.

Raman spectroscopy is an ideal tool for detailed quantitative analysis of biofluids. It provides excellent chemical specificity with minimal sample preparation, and can preserve the test fluid for further analysis. These features make it well suited not only to critical situations like the one described above, but to routine analysis. Its rapid response and potential for portability make well suited for regular monitoring applications.

In this chapter we will discuss applications of Raman spectroscopy to diagnostics using different biofluids. Following this, we will discuss current methods to enhance Raman spectra and push the limits of detection. Finally, the design and performance of our micro-opto-fluidic device with an integrated waveguide will be detailed.

3.1 Raman Spectroscopy in Biological Fluids

Biofluid analysis is invaluable to a large range of applications. Fluids such as tears, saliva, and urine can be collected non-invasively, which may introduce a significant quality of life increase to the patient. In this section we aim to provide an overview of Raman spectroscopy's suitability towards biofluids, and its value in patient comfort and diagnostics.

3.1.1 Blood

Blood delivers nutrients, removes waste, maintains a balance of electrolytes, and protects the body from infection [21]. Each day millions of blood tests are performed for diagnostics and general health monitoring [16]. The chemical specificity of Raman spectroscopy makes it an ideal candidate for blood analysis. Clinical laboratory tests often require that the sample be pretreated with reagents or by centrifuging. This leaves the sample unusable after the test is complete, requiring further samples from the patient if the first set of tests are insufficient. It is in the interest of patient comfort that a method is available which minimizes the amount of blood required.

Glucose Monitoring

Diabetes is a prominent disorder affecting hundreds of millions of people worldwide which requires regular blood glucose monitoring, and facilitating this process has been the source of extensive research [7]. Liquid core waveguides used with Raman spectroscopy have been investigated for this purpose, as they help to overcome Raman's weak signal. Researchers have designed a method to sequentially collect a Raman spectrum of blood serum followed by a white-light spectra to correct for distortions in the Raman signal due to changes in absorption [7]. Glucose concentrations were predicted using partial least squares (PLS), a linear regression modelling technique [42]. Reference versus predicted concentrations are compared using a Clarke error grid for both the raw and white-light-corrected spectra, illustrated in figure 3.1. The Clarke grid uses ratios of predicted-versus-actual blood glucose concentration to assess ramifications on error in prediction. Clinical accuracy for blood glucose requires any monitoring system to be able to accurately predict levels within 20% for concentrations ranging from 70 mg/dL to over 400 mg/dL [43]. Thus a blood glucose measurement device must be accurate to at least within 14 mg/dL. Predictions in zones A or B of figure 3.1 are considered clinically accurate, while the remaining zones C to E could lead to potentially dangerous over- or under-correction of the patient's blood glucose.

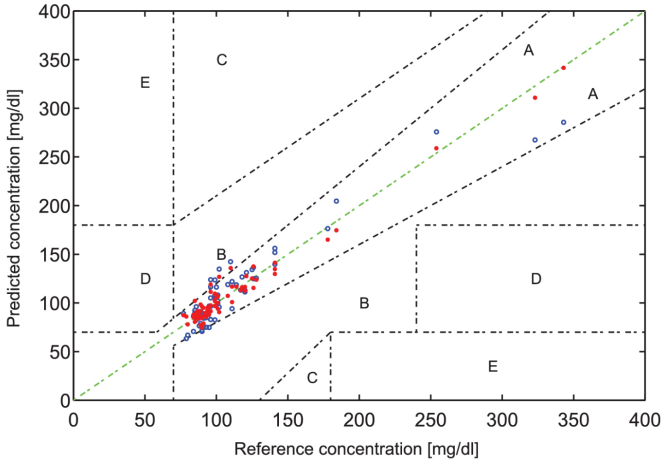

Figure 3.1: Glucose concentration predictions in blood serum versus reference concentrations, presented on a Clarke error grid. Solid red circles denote predictions made with raw Raman spectra. Open blue circles represent predictions made using white-light-corrected spectra. Reprinted with permission from [7], Optical Society of America Publishing.

In both raw and white-light corrected Raman cases, all glucose predictions fell within clinically

acceptable ranges, zones A and B. Using the raw spectra led 11 samples to fall in zone B, representing an error in prediction greater than 20% but which will not lead to an error in treatment. The number of samples classified in zone B falls to just 4 when the white-light-corrected spectra are used. Extending this to whole-blood glucose quantification has proven itself to be a significantly more difficult task due high-scattering red blood cells and glucose's small Raman scattering cross-section [16, 44]. Achieving a method which simplifies blood glucose determination by eliminating clinical sample preparation would greatly expedite diagnostics and treatment.

Alzheimer's and Dementia

Worldwide, 35 million people were estimated to be living with dementia in 2010. By 2050 this number is estimated to rise to 115 million [45]. Disease progression is frequently gradual which complicates diagnosis, but early treatment and intervention can help patients remain functional and independent as long as possible. To assist in this regard, a preliminary study used Raman spectroscopy to compare the blood of Alzheimer's and dementia patients versus those who were either healthy or suffered from other degenerative diseases [18]. Raman signatures of dried blood samples were analyzed using artificial neural networks. Researchers demonstrated a high probability to assign a single subject to the correct diagnostic category, and identified spectroscopic markers consistent with reported biomolecules of Alzheimer's and dementia [18]. In this situation Raman spectroscopy has not only provided evidence that it may serve as a diagnostic tool for Alzheimer's and dementia, but also as a verification tool in the search for disease biomarkers in general. Some attempt was made to control for variables such as current medication regimes in the experiment, but further study is needed to validate the method as a large-scale screening technique.

3.1.2 Tears

Human tear fluid protects and provides nutrients to the eye. Variation in its composition can be an indicator of ocular disease and illness in the human body as a whole [17]. Owing to its ease of collection relative to biofluids such as blood, it is an optimal candidate for use in a non-invasive biological analysis system. Tears may be sampled continuously and are less susceptible to dilution than urine or saliva [8]. Human tear analysis must be approached with caution, however, as its constituent concentrations have been shown to vary with collection method [17].

Protein Indicators of Ocular Diseases

Human tears contain more than 400 different proteins, although three in particular comprise approximately 99% of the total concentration [30]. The individual concentrations of these three proteins, lysozyme, lactoferrin, and tear-specific prealbumin, vary with infections and have been extensively studied as possible indicators of ocular diseases [17,46]. DCDRS is commonly applied to enhance the spectrum of human tears, yielding very high signal to noise spectra without extensive acquisition times. A direct comparison between solution-phase measurements and DCDRS showed that DCDRS could be used to predict protein concentration with an error below 1 mg/mL [17]. While Raman modes from the three major proteins are present in solution-phase measurements at physiologically relevant concentrations, the signal to noise ratio is quite poor. Peak assignments are associated with significant error, which lowers the confidence in determining composition. This is particularly problematic if we require analysis

on one of the >99% of proteins present in significantly lower concentrations. DCDRS, by contrast, yields a high signal-to-noise ratio. Additional tear components such as lipids and urea were observed to take on a unique spatial distribution in the dried pattern, offering another dimension for solute analysis. Due to the destructive nature of the technique, however, DCDRS can only reveal relative constituent concentrations. Methods have been proposed which would allow absolute quantities to be determined, but they require the inclusion of an additional reference measurement [47]. This may be undesirable for some facilities which wish to avoid additional processing time, sample preparation, and instrumentation.

Conjunctivitis

Absolute concentration determination is not always necessary for diagnostics. DCDRS in conjunction with SERS, together known as drop-coating deposition surface-enhanced Raman spectroscopy (DCD-SERS), has demonstrated the ability to detect three specific Raman modes in human tears which are markers of adenoviral conjunctivitis infection [19]. Conjunctivitis has several possible causes (viral infection, bacterial infection, allergies), and proper treatment requires the root cause to be accurately determined. Cell culturing and polymerase chain reactions are currently employed to provide this diagnosis, but require access to a laboratory and processing times of several weeks [19, 48]. The infection may worsen during this waiting period, causing discomfort to the patient and risk of infecting others. DCD-SERS has demonstrated high signal to noise spectra in detecting adenovirus Raman modes, by analyzing ratios of principal component (PC) loadings at three particular wavenumbers. Thus it is not necessary in this situation to be able to explicitly correlate volume of analyte with a particular Raman mode intensity. In addition, the researchers observed greater prediction accuracies in certain DCDRS zones, leading to a potential for zonal spectrum differences to serve as a secondary diagnostic tool [19]. Tears collection was performed by placing a polyester-fiber rod in contact with the eye for up to 5 minutes and then centrifuging the rod [19]. This collection method can pose significant patient discomfort and is not feasible when facilities are limited, but the test itself has demonstrated success at providing a rapid response relative to clinical assessment.

3.1.3 Urine

Excess concentration of urine components such as creatine or uric acid can be caused by muscular dystrophy, cardiovascular disease, kidney stones, or a wealth of other diseases and disorders [49]. Urine analysis with Raman spectroscopy has the potential to serve as a valuable diagnostic tool for widespread and often fatal health issues which are either difficult to diagnose, or require constant routine monitoring. The following two examples will illustrate how Raman spectroscopy can be used to correctly classify biosamples without the need to explicitly quantify analyte concentrations.

Diabetes and Hypertension

Diabetes mellitus and hypertension are two of the most common diseases in industrialized nations. Long-term complications include blindness, renal failure, and an increased risk of cardiovascular disease [6]. Periodic monitoring of the glomerular filtration rate can mitigate these risks, but the standard monitoring method requires a significant time commitment from the patient in terms of a 24 hour collection of urine, which is then submitted to a lab for analysis [6]. Real-time results via Raman spectroscopy would simplify the procedure for both patient and healthcare provider. A recent study performed Raman

analysis on three potential biomarkers (urea, creatine, glucose) in groups of patients both with and without complications from diabetes mellitus or hypertension [6]. The study showed a good capacity in using discriminant analysis to correctly distinguish between patients who were healthy, low-risk, high-risk, or suffering from renal failure. The average correct classification rate in this study was 70% but the minimum correct classification rate for one group of patients was a mere 32%, proving that there is ample room for technique improvement.

Prostate Cancer

Prostate cancer has high rates of occurrence, misdiagnosis, and mortality [12,50]. Diagnosis and screening can involve uncomfortable rectal examinations, and there is concern that current screening methods are leading to over-diagnosis, as the rate of detection is increasing but the survival rate is not [12]. SERS was performed on the urine samples of patients with and without prostate cancer, and spectrum differences analyzed between the two groups. Using a mixture of PCA and linear discriminant analysis, which maximizes between-group variability relative to within-group variability, researchers achieved an overall diagnostic accuracy of 95% [12, 42]. These study results are promising, however the experiment was performed on a small cross section of the population ($n = 18$) and samples were filtered and centrifuged to remove components which may interfere with the spectrum [12]. A method which eliminates these processing steps would reduce reliance on costly equipment and turnaround time, streamlining the analysis process.

3.1.4 Saliva

Saliva is one of the easiest biofluids to collect, and a valuable biological indicator. Insight can be gained into system immunity due to the range of antibodies present, molecular biomarkers which can assist in diagnosis, and detection of trace environmental toxins that can ensure threats to public health are promptly identified and addressed [51].

Periodontal Disease

Periodontal diseases are chronic inflammations of tissues surrounding teeth. Untreated, health implications include tooth loss and cardiovascular disease, and they affect 20-50% of people worldwide [52] [53]. There is currently no simple and rapid test for detection, diagnosis, and monitoring of periodontitis [54]. Clinical assessment is the current standard, despite its potential for patient discomfort and heavy reliance on trained staff to interpret results. Resonant Raman spectroscopy (RRS) of saliva has recently been investigated for early periodontitis detection [55]. Researchers performed RRS on samples of dried saliva with excitation wavelengths chosen to produce resonance with the carotenoids beta-carotene and lycopene, as heightened carotenoid content in saliva has been linked to periodontitis. This method has the potential to improve early detection of periodontitis, though several drawbacks exist. Requiring that the saliva sample be dried before analysis increases the processing time and need for trained personnel, and does not provide a quantitative measure of disease progression. In addition, RRS by definition requires predefined knowledge of the modes under investigation. This limits the instrumentation's flexibility for other analysis, which is undesirable for facilities with limited space and budget.

Drug Metabolism Monitoring

Real-time metabolism monitoring during drug administration requires achieving both identification and quantification of analytes in a solution. A common-prescribed chemotherapy drug (5-Fluorouracil), for example, exhibits variation in the dominant metabolic pathway. Resulting fluctuations in the drug's effectiveness at disrupting cancerous and normal cells alike requires that dosing be carefully monitored to prevent potentially fatal reactions [56]. Raman spectroscopy on saliva has been investigated to reduce the need for blood plasma analysis in metabolism monitoring. Compared to traditional blood plasma analysis, saliva collection is non-invasive, carries a drastic reduction in risk of HIV infection, and demonstrates similar drug metabolism [57]. Drug concentrations in saliva vary from 0.1 μg/mL up to 28 μg/mL. Researchers have successfully observed a limit of detection of 2 μg/mL using SERS on saliva samples doped with 5-fluorouracil, falling within this physiologically relevant range [58]. SERS was also performed on two major metabolites of 5-fluorouracil, 5-fluorouridine and 5-fluoro-2'-deoxyuridine, providing promising evidence in favor of the technique. Biofluids cannot be recovered after SERS, which is problematic when specimens are difficult to replenish. Obtaining significant repeated saliva samples from a chemotherapy patient can be uncomfortable and challenging due to common dry mouth side effects [59].

3.2 Portable Non-Destructive Sample Analysis

Common themes amongst the research in section 3.1 include lengthy sample or substrate preparation, the need for specialized equipment and personnel, and sample destruction. Increasing accessibility to meaningful and reliable diagnostics requires a method which is cost-effective, has excellent chemical specificity, and can be adapted to quantitatively analyze a wide range diagnostically relevant fluids with sensitivity at or exceeding μM. To this end we have developed a microfluidic device with integrated waveguide for non-destructive biofluid analysis using Raman spectroscopy, to achieve fully non-invasive physiological monitoring for the first time.

3.2.1 Microfluidic Design Considerations

A schematic of the complete device is illustrated in figure 3.2. The microfluidic component (figure 3.3) is comprised of a section of patterned poly(dimethylsiloxane) (PDMS) (Sylgard 184 from Dow Chemical Company, purchased from Krayden Canada) bonded to a square glass coverslip (VWR brand, 22 or 25 mm side length, thickness 0.13 to 0.16 mm, purchased from University of Toronto Medical Store). PDMS is an optically transparent and biocompatible elastomer which is readily available, inexpensive, and easy to work with [60]. Four ports are punched in the PDMS which allow tubing and both ends of a section of TCT to be connected directly to the microfluidic channels. This configuration ensures that the sample remains in a sterile enclosed environment throughout the duration of Raman collection. Sample destruction is eliminated in part because the tubing which exits the microfluidic device can be connected to a second syringe for collection, and in part because constant recirculation mitigates heating and evaporation which can damage or alter the sample.

Microfluidic channels are sized to match the cross-sectional area of the TCT, minimizing sudden flow rates and pressure changes. Integrating both ends of the TCT in the microfluidic device ensures that the setup fits neatly on microscope stages without requiring equipment reconfiguration.

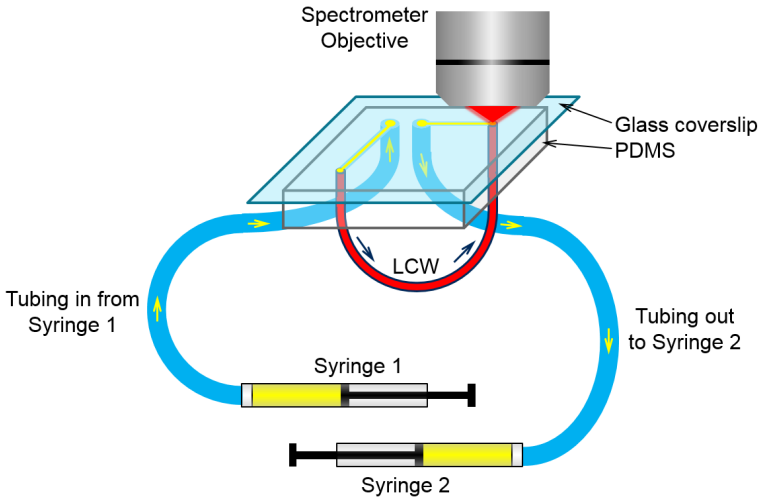

Figure 3.2: Micro-opto-fluidic-waveguide setup schematic

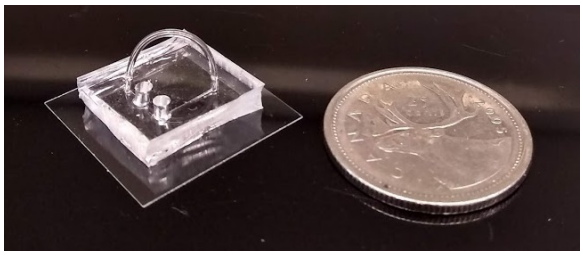

Figure 3.3: Micro-opto-fluidic device detail and scale.

The microfluidic device photomask (figure 3.4) was designed with the following considerations:

- Two ports diameter 2.0 mm, approximately matching outer diameter of silicone tubing (Cole-Parmer platinum-cured silicone tubing, item RK-95802-00, outer diameter 1/12" = 2.1 mm). A slightly smaller diameter ensures a snug fit when the tubing is inserted.
- Two ports match outer diameter of TCT (Biogeneral AF2400, outer diameter 0.032" = 813 μm). Holes are punched at 750 μm ensuring a snug fit for the TCT in PDMS.
- Microfluidic channels are sized 200 μm wide to match the inner diameter of TCT (Biogeneral AF2400, inner diameter 0.008" = 203 μm).
- Separation between ports for the TCT ensures that it exceeds its 4 mm minimum bend radius when the two ends of the waveguide are inserted into the device.

3.2.2 Micro-Opto-Fluidic Device Mount

The device rests slide-side-up on a 3D-printed microscope stage adapter whose design is pictured in figure 3.5. All pieces are printed out of polylactic acid (PLA) with a layer height of 0.1 mm. Narrow grooves in the base pinch tubing connections slightly, allowing the device to be pulled to rest flat. Grooves which hold the microfluidic coverslip are enlarged by 0.25 mm in each dimension so that it is snug but can be

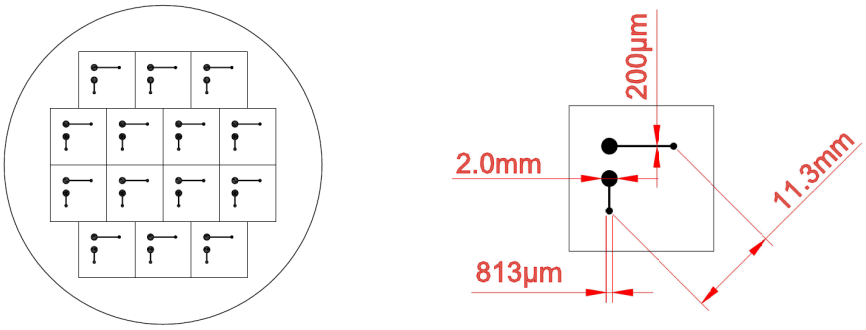

Figure 3.4: Microfluidic device mask design dimensions. Left: Device layout on a 4" Silicon wafer. Right: Channel dimensions on each microfluidic device. Areas which become raised channels in poly(dimethylsiloxane) (PDMS) are indicated with solid black fill.

inserted flat without catching on a print layer and breaking. This configuration is illustrated in figure 3.6

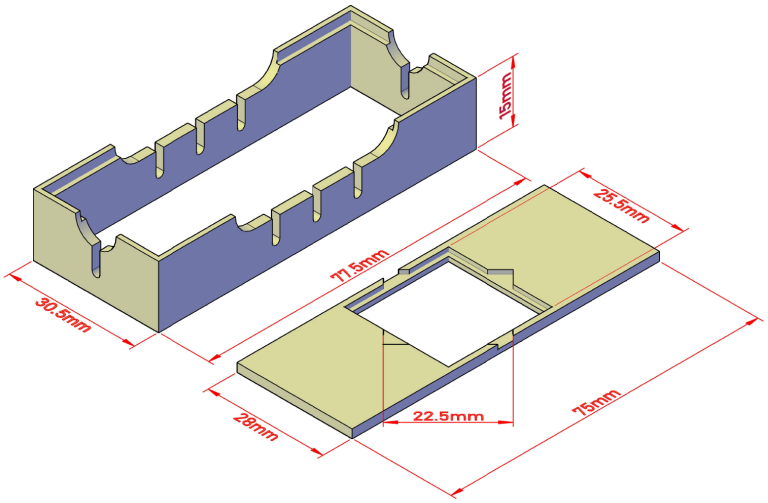

Figure 3.5: Designs for a 3D printed microscope stage adapter. This configuration allows micro-opto-fluidic devices on 22 mm or 25 mm glass coverslips and all tubing connections to rest neatly on a microscope stage.

A 10× objective is first used to optically align the microscope and one end of the TCT. Fluid is slowly injected from syringe 1 to minimize air bubbles. Once the fluid has been injected through the full length of the TCT, a syringe pump is activated for and the laser is turned on. We collect a rapid set of successive spectra to determine the optimal depth of focus. This mitigates small changes in spectra which may arise between different devices when the distance between slide surface and TCT is variable. Figure 3.7 demonstrates the signal differences which may arise if the spectrometer is not correctly focused to the waveguide. Focal depth is used to describe the vertical position of the focal point, relative to the surface of the microfluidic coverslip. Spectra appear considerably different over 20 μ. If the focal point is too shallow we observe silica modes from the glass coverslip which distorts the sample's Raman modes. If the focal point is too deep then the objective cannot effectively couple all of the excitation light and the waveguide is under-filled. The optimal focal depth avoids these issues.

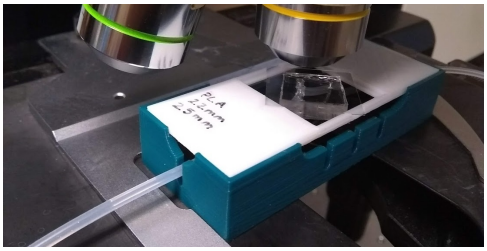

Figure 3.6: A 22 mm micro-opto-fluidic device in use on a Horiba LabRam HR800 Spectrometer

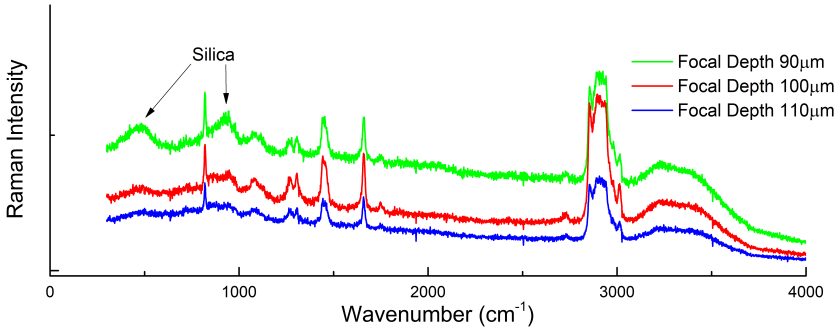

Figure 3.7: Spectrum differences which arise due to changes in focal depth. Shallower focus contains Raman modes from the glass coverslip. Deeper focus compromises fiber-objective coupling which reduces Raman mode intensity. Sample is a solution of 5% isopropyl alcohol (IPA), 75% Intralipid, and 20% deionized water (DIW) (% v/v)

A custom software suite and miniature dual-syringe pump have been created to accompany the microfluidic setup and permit post-measurement sample retrieval. Chapter 5 details the software interface.

3.2.3 Dual-Syringe Pump

A low-cost dual syringe pump named Raman Microfluidic Pump (RaMP) was designed and built to accompany the microfluidic device and is pictured in figure 3.8. The pump housing and attachments are 3D printed out of either PLA or acrylonitrile butadiene styrene (ABS) with either 0.1 mm or 0.2 mm layer height. Material was chosen based on the filament which had previously been loaded into the printer.

All components were designed in AutoCAD and printed on a MonoPrice Maker Select V2.1 personal 3D printer. 3D models and their design considerations will be detailed in this section.

Figure 3.9: a deep platform with rests for two syringe barrels and a trough to wedge the barrel flange. This piece is wide enough for two syringes to rest side by side, and long enough to support their barrels. Two circular cutouts in the motor-facing side of the 3D printed piece act as a support for the threaded rod which controls the syringe plungers. Underneath there are two depressions to insert hexagonal nuts which have had their threads sanded out, permitting them to free spin on the threaded rod and acting as a crude bearing.

Figure 3.10: a section to support both motors. A slight 0.8 mm depression allows the motor mounting holes to overlap and keep the motors close together while remaining parallel. This reduces the device footprint.

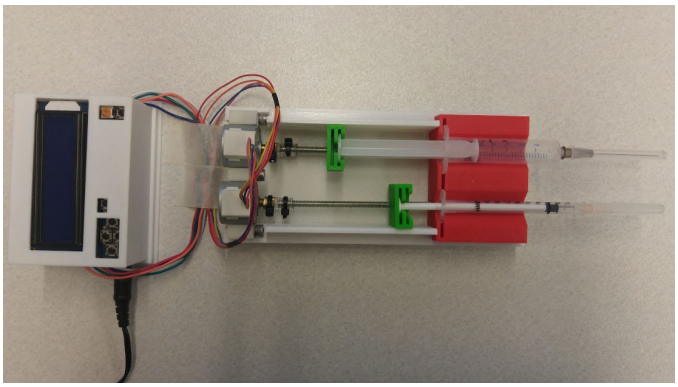

Figure 3.8: Assembled dual-syringe pump.

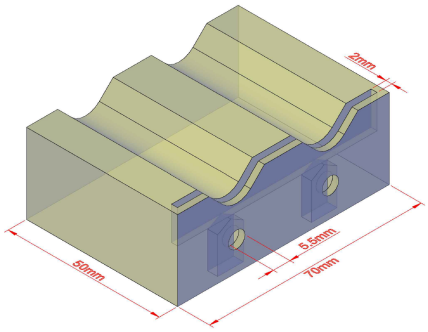

Figure 3.9: Support piece for syringe barrels and threaded rod.

Figure 3.11: a piece to depress the syringe plunger flange as the threaded rod turns. Two slots allow the plunger of either a 1 mL or 6 mL Becton Dickinson syringe to be held firmly. Below, a cutout slips over a hexagonal nut. This piece is designed so that the plunger position along the threaded rod can easily be changed by removing the piece and free spinning the nut along the rod length, then replacing the piece. To remain upright during pumping, the width of each piece ensures that it is abutting the edge of the syringe pump base.

Figure 3.12: A printed base for the device. Each component which has been discussed is overlaid on the model.

We opted to use Arduino to power the pump since they are widely available and relatively inexpensive, with well-documented resources for any necessary modifications. Stepper motors were selected to provide precise control over the syringe plunger position and therefore the pumping rate. The desired pumping rate is achieved by taking one step with each motor followed by a timed rest. As such there is no minimum pumping rate. The maximum pump rate for a 1 mL Becton Dickinson syringe is 0.9 μL/minute. Resulting fluid flow pulses slightly but no issues have been observed. Syringe pump materials which were not 3D printed are detailed below.

- Arduino Uno R3 purchased from Adafruit Industries.
- Adafruit Motor/Stepper/Servo Shield for Arduino v2 Kit purchased from Adafruit Industries.
- LCD Shield Kit with 16x2 Character Display purchased from Adafruit Industries.
- 2× Hobby stepper motors (Radio Shack 2730767) purchased from Sayal Electronics.

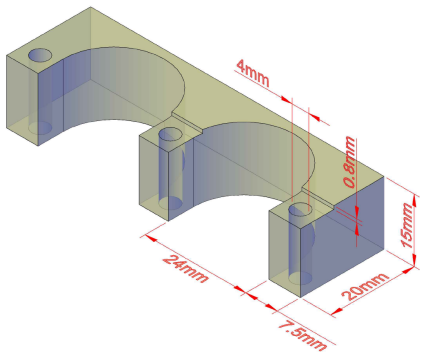

Figure 3.10: Support piece for syringe barrels and threaded rod.

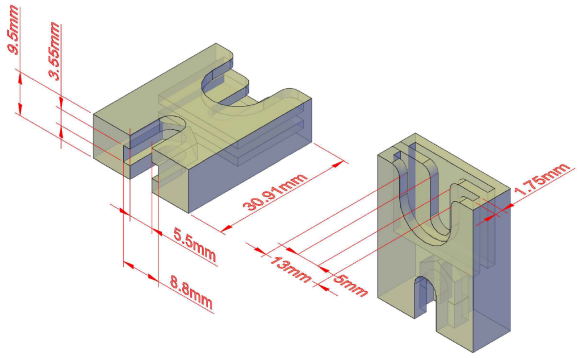

Figure 3.11: Syringe plunger flange adapter

- 3× Screws to attach motors to a base (found in lab, source unknown).
- Threaded rod type C-8-32, 32 threads per inch, purchased from Canadian Tire.
- 4× hexagonal nuts type 8-32, purchased from Canadian Tire. Two nuts are drilled or sanded to remove their threads.
- 2× 1" lengths of rubber tubing (scrap pieces found in lab, approximate inner diameter 5 mm, approximate outer diameter 7 mm, source unknown).
- 4× zip-ties (source unknown).
- 12 V 6W AC/DC barrel power adapter, purchased from DigiKey.

Threaded rod and hex nuts were selected for the smallest diameter and highest number of threads per inch which was readily obtainable. Rubber tubing and zip-ties are used to couple the stepper motors to the threaded rod as pictured (figure 3.13) using a technique inspired by low-cost 3D printer builds [61].

The setup which we have described may be integrated with a portable Raman spectrometer to achieve rapid, mobile, and inexpensive analysis of biofluids.

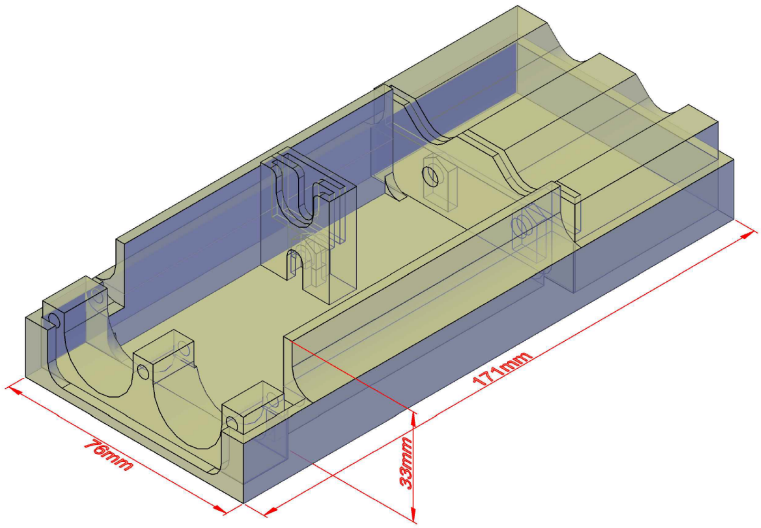

Figure 3.12: 3D printed syringe pump base, with all printed components overlaid to show their position

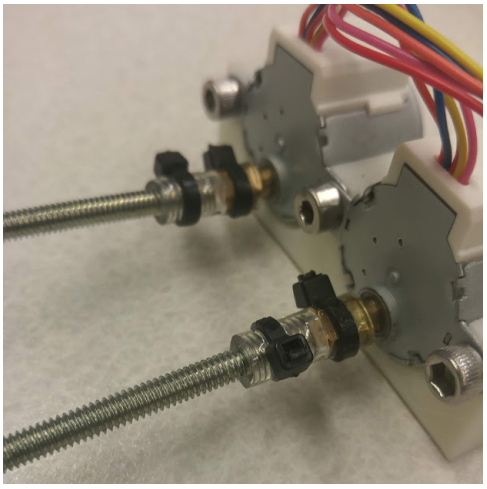

Figure 3.13: Coupling between the stepper motors and threaded rod with a piece of rubber tubing and zip ties.

Chapter 4

Predictive Diagnostics via Principal Component Analysis

Quantitative analysis of Raman spectra requires that we observe and monitor trends within and across a range of spectra. However this can be prohibitive when each spectrum contains several thousand data points. PCA is a widespread technique in spectroscopy and chemometrics to reduce dimensionality and facilitate quantification of such information [62]. PCA is accomplished by forming a set of PCs which are themselves mutually orthogonal, linear functions of the original data, and which maximize variability within the set.

Figure 4.1 and equation 4.1 illustrate the relationship between PCs and the original data set. Throughout this discussion we will use the convention of upper-case bold to denote matrices, lower-case bold for column vectors, and lower-case italics for scalars. A superscript ($^\intercal$) is used to indicate the matrix or vector transpose. Table 4.1 details all notation and variables used in this chapter.

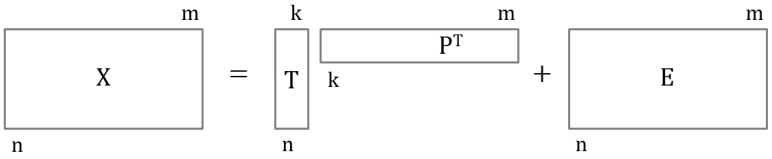

Figure 4.1: Visualization of the relationship between a data set and its principal components (PCs). Modified from [63].

$$\begin{aligned} \mathbf{X} &= \mathbf{T}\mathbf{P}^\intercal + \mathbf{E} \\ &= \mathbf{t}_1\mathbf{p}_1^\intercal + ... + \mathbf{t}_k\mathbf{p}_k^\intercal + \mathbf{E} \end{aligned} \tag{4.1}$$

The data matrix $\mathbf{X}$ consists of rows of independent samples (Raman spectra) and columns of variables (wavenumbers). Each spectra in the set can be expressed as a linear sum of k PCs, which are themselves the product of basis vectors and an associated weighting factor. The terms loading vectors and scores are often used in place of basis vectors and weighting factors respectively. Modeling the spectra with respect to its PCs presents the opportunity to form a regression prediction model used to gain insight into an unknown spectra's composition.

Table 4.1: Notation reference for chapter 4.

$\|.\|$	Vector norm
ε	NIPALS convergence tolerance
i	Dummy indexing variable
j	Dummy indexing variable
k	Number of principal components
m	Number of data points within each sample
n	Number of independent samples in the reference data set
q	Number of unique constituents in regression estimation
r	Number of independent samples in the unknown data set
$\mathbf{1}_m$	Vector of ones (size $m \times 1$)
$\mathbf{p}$	Vector of loadings (size $m \times 1$)
$\mathbf{t}$	Vector of scores (size $n \times 1$)
$\mathbf{x}_j$	Vector formed from the j-th column of $\mathbf{X}$
$\mathbf{B}$	Regression coefficient matrix (size $q \times k$)
$\mathbf{C}$	Known concentration matrix (size $q \times n$)
$\mathbf{C_{est}}$	Estimated concentration matrix (size $q \times r$)
$\mathbf{E}$	Matrix of residuals (size $n \times m$)
$\mathbf{I}_n$	Identity matrix (size $n \times n$)
$\mathbf{P}$	Matrix of loading vectors (size $m \times k$)
$\mathbf{T}$	Matrix of scores (size $n \times k$)
$\mathbf{X}$	Matrix of training spectra (size $n \times m$)
$\mathbf{X_{est}}$	Matrix of unknown spectra (size $r \times m$)

PCs are functions of the original data set, so they are excellent tools to reveal trends which may not be apparent upon manual inspection. These trends can be put to use in predictive multivariate linear regression models like principal component regression (PCR), significantly simplifying and expediting quantitative analysis of Raman spectra. It simultaneously means that PCs are highly subject to outliers and missing data, unintentionally correlating with experimental artefacts. Highest order PCs, for example, commonly describe signal noise. PC and artefact correlation does not always pose a disadvantage. We demonstrate how this can be used to our benefit in section 4.3.2 and chapter 6.

In this chapter we will first discuss the PCs themselves and how they are formulated. Following this, we will elaborate on how they can be used in a predictive capacity for diagnostic purposes, and as a tool to statistically identify and exclude processing techniques which are inappropriate to the data. This chapter contains material which has been accepted for publication [1].

4.1 Calculation of Principal Components

The task of determining PCs from a data can be accomplished several different ways. If all PCs are desired, singular value decomposition (SVD) is a computationally-efficient option.

Performing the SVD of our data matrix $\mathbf{X}$ yields the decomposition:

$$\mathbf{X} = \mathbf{ULA}^\intercal \tag{4.2}$$

$\mathbf{A}$: Orthonormal matrix such that $\mathbf{A}^\intercal\mathbf{A} = \mathbf{I}_r$ (size $m \times r$)
$\mathbf{L}$: Diagonal matrix of singular values (size $r \times r$)
$\mathbf{U}$: Orthonormal matrix such that $\mathbf{U}^\intercal\mathbf{U} = \mathbf{I}_r$ (size $n \times r$)
r : Rank of $\mathbf{X}$

When all PCs are required for analysis we set $k = r$ and obtain the scores and loadings by setting $\mathbf{T} = \mathbf{UL}$ and $\mathbf{P} = \mathbf{A}$ respectively. An extensive and thorough derivation of SVD can be found in literature [62, 64, 65]. In spectroscopic regression analysis, it is more often the case that only the PCs of highest variance are desired in order to minimize insignificant spectral variation. Data sets may come to contain hundreds of independent spectra; it is computationally prohibitive to calculate dozens of PCs which will never be required for analysis. Non-iterative partial least squares (NIPALS) has been shown to reduce computation time in these situations [66].

NIPALS iteratively calculates each set of weights and loadings by repeatedly regressing $\mathbf{X}$ on to a weighting matrix to obtain improved loading vectors, and then regressing the $\mathbf{X}$ on to the improved loading vectors to obtain improved weightings. When the PC converges it is removed from the associated error matrix for the calculation of successive scores and loadings (equation 4.3). The algorithm may be terminated once sufficient variance is described, so it is ideal for cases where the highest order PCs are irrelevant [63].

$$\mathbf{E}_i = \mathbf{E}_{i-1} - \mathbf{t}_i\mathbf{p}_i^\intercal \tag{4.3}$$

To initialize NIPALS, we set $i = 1$, $\mathbf{E}_0 = \mathbf{X}$, $\mathbf{t}_{i1} = \mathbf{x}_j$ ($j \in [1, m]$), and define an error tolerance (ε) for convergence.

1. Obtain a loading vector by projecting $\mathbf{E}_{i-1}$ on to the score vector: $\mathbf{p}_i^\intercal = \mathbf{t}_{n1}^\intercal\mathbf{E}_{i-1}(\mathbf{t}_{i1}^\intercal\mathbf{t}_{i1})^{-1}$
2. Normalize the loading vector: $\mathbf{p}_i^\intercal = \mathbf{p}_i^\intercal/\|\mathbf{p}_i^\intercal\|$
3. Obtain a score vector by projecting $\mathbf{E}_{i-1}$ on to the loading vector: $\mathbf{t}_{i2} = \mathbf{p}_i\mathbf{E}_{i-1}$
4. Terminate if $|\mathbf{t}_{i2} - \mathbf{t}_{i1}| < \varepsilon$, and let $\mathbf{t}_i = \mathbf{t}_{i2}$. If the inequality is not satisfied, let $\mathbf{t}_{i1} = \mathbf{t}_{i2}$ and return to step 1.

The principle behind NIPALS rests in the fact that it is an eigenvector equation. The denominators in both steps 1 and 2 are scalar, allowing them to be merged into a single constant c. These equations can then be combined to reveal the eigenvector equation [63]:

$$\begin{aligned} c\mathbf{p}_i^\intercal &= \mathbf{t}_i^\intercal\mathbf{E}_i \\ &= (\mathbf{E}_i\mathbf{p}_i)^\intercal\mathbf{E}_i \\ &= \mathbf{p}_i^\intercal\mathbf{E}_i^\intercal\mathbf{E}_i \\ (c\mathbf{I}_n - \mathbf{E}_i\mathbf{E}_i^\intercal)\mathbf{p}_i &= 0 \end{aligned} \tag{4.4}$$

NIPALS has been shown to reduce computation time when only the PCs of highest variance are desired [66]. While faster algorithms are available, NIPALS has demonstrated itself to be a reliable tool with which to precisely calculate PC loading vectors, as well as being easily modified to handle missing data. These features make NIPALS an excellent candidate for use in a robust user-independent analysis suite [67, 68].

Higher order PCs can represent noise or experimental artifacts within the data set, and may not pose a positive contribution to the predictive model. Including these variables in a model introduces risks such as over-fitting to the parameter being predicted, or compromising the model's performance when applied to new samples [69]. Cross validation may be used to assess the predictive ability of PCR models. It is an excellent tool to account for sample-specific errors and generate a reproducible predictive model [70]. Though it can be computationally expensive in large data sets we shall demonstrate how the addition of a statistical F-test (section 4.4) can preemptively reject pre-treatment methods which lead to an ineffective model.

4.2 Principal Component Regression

Once the PCs have been defined, they may be used as predictors in a multivariate linear regression model. For the purposes of this thesis, the predicted item is concentration of an analyte, however the process is equally applicable to a wide range of predictions such as the solubility of peanut protein, or to positioning error in GPS [71, 72]. Two independent data sets are required for PCR: a reference set whose concentrations are known, and a set whose concentrations are unknown.

Starting with the data set with known composition, the algorithm NIPALS is used to obtain the weighting and loading vectors. Score, loading, and concentration matrices are multiplied as shown in equations 4.5 and 4.6 to obtain the regression coefficients and an estimation for constituent concentrations ($\mathbf{C_{est}}$) [63].

$$\mathbf{B} = \mathbf{T}^\intercal \mathbf{C} (\mathbf{T}^\intercal \mathbf{T})^{-1} \tag{4.5}$$

$$\begin{aligned} \mathbf{C_{est}} &= \mathbf{B}\mathbf{T}^\intercal \\ &= \mathbf{B}(\mathbf{X_{est}}\mathbf{P})^\intercal \end{aligned} \tag{4.6}$$

PCR significantly simplifies and expedites quantitative analysis of Raman spectra. Limitations stem from PCA, whose PCs are highly sensitive to outliers in the data set and may unintentionally correlate with experimental artifacts. PCR's capability to repeatedly provide reliable and meaningful predictions can be significantly hampered by the presence of these spectral features.

4.3 Data Pre-Processing

Raw Raman data often contains undesirable features which can hamper PCR's ability to provide meaningful insight. A fluctuating fluorescent background and amplitude differences due to variance in coupling into a waveguide are two very common features which, when compensated for, improves PCR's ability to form a robust model for the spectra itself. Several techniques, such as amplitude scaling and mean centering, are standard PCA preprocessing methods and will be discussed in this section [73]. Following the discussion on preprocessing techniques we shall introduce our novel mass-processing baseline removal approach, exploiting spectrum features in PCs which are typically a drawback.

The optimal preprocessing method for a training set can be determined by trial and error or by design of experiments [74]. Neither approach is generic or robust, and does not indicate suitability to

future predictions. Both methods can also prove to be lengthy processes when multiple techniques are being tested simultaneously [74, 75]. As such, there is still a real lack of a dependable, automated and sufficiently generic approach to render PCR immune from its limitations and enable it to fulfill its power of quantitatively analyzing Raman spectra, from real life biofluidic samples.

4.3.1 Standard Methods

Amplitude Normalization

Amplitude normalization is often required prior to PCR to ensure consistency between spectra. Among experiments, or even within one, slight changes in path-length or focal point can manifest as differences in the amplitude of Raman peaks, negatively impacting the results of PCR. Three straightforward techniques to accomplish amplitude normalization are scaling based on reference peak height, by standard deviation using standard normal variate transform (SNV), or by percentile with the robust normal variate transform (RNV) [73].

If all spectra within a set are known to contain a common constituent in a given concentration, this may be used as a ruler by which to scale the Raman spectra. This method requires considerable confidence in the reference parameter's consistency between samples. Mistakenly overlooking variance of the ruler parameter can lead to significant errors propagating through analysis.

Barring the presence of a common reference peak, amplitude normalization can be performed under the assumption that the distribution of peak amplitudes will be approximately normal. In this case it may be appropriate to use the SNV. SNV scales each spectrum by the standard deviation of its amplitudes, after mean-centering to compensate for amplitude shift (equation 4.7).

$$\mathbf{x_{adj}} = \frac{\mathbf{x} - \mu(\mathbf{x})}{\sigma(\mathbf{x})} \tag{4.7}$$

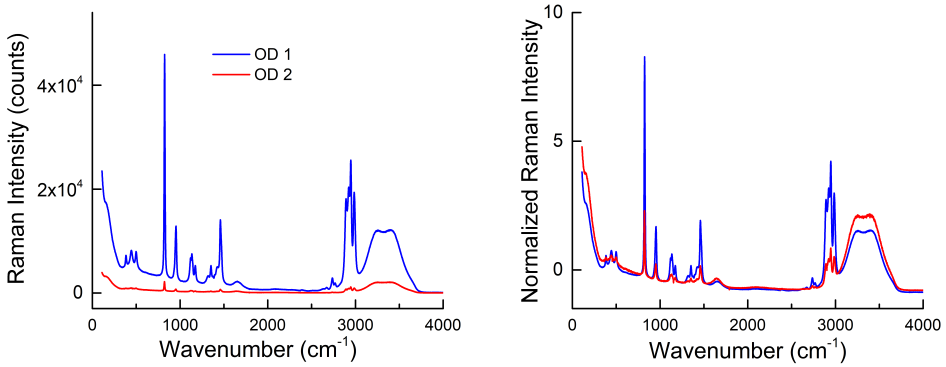

Figure 4.2: Graphical representation of the standard normal variate transform. Left: Two spectra are collected for a two different samples using different optical density (OD) filters, as defined in section 2.4 equation 2.15. Right: The spectra after standard normal variate transform (SNV) is applied. The corrected scale allows Raman mode intensities to be properly assessed relative to each other. Sample collected with filter OD1 is composed of 30% isopropyl alcohol (IPA) and 70% deionized water (DIW) (% v/v). The sample collected with filter OD2 is composed of 10% IPA and 90% DIW.

RNV, similar to SNV, scales spectrum data based on an assumption about its distribution. It was introduced as the solution to a closure problem [76]. Closure, in statistics, indicates that the sum of a

set is equal to a certain number, therefore if one value in the set increases, another must decrease to compensate. As an SNV spectrum is mean-centered, its sum is zero and the set is closed. This can have the unwanted effect of introducing artificial variance in some wavenumbers in an attempt to maintain closure [76]. RNV modifies SNV by using percentiles rather than means and standard deviations:

$$\mathbf{x_{adj}} = \frac{\mathbf{x} - pct(\mathbf{x})}{\sigma[\mathbf{x} \leq pct(\mathbf{x})]} \tag{4.8}$$

An immediately apparent benefit to RNV is the reduced influence of outliers. If the distribution of response measurements for one variable is skewed in any way, the percentile will be a more robust descriptor of tendencies within the data set than the standard deviation [77]. A downside of this technique is that it requires percentile optimization to provide the best possible prediction model. One approach to accomplish this is to perform a preliminary series of regressions at coarse percentile increments, comparing the results to those obtained using SNV [76].

Mean Centering

Mean-centering (MC) is a traditional and often-used form of preprocessing for multivariate modeling. It is particularly suitable for removing common offsets in a data set [78]. MC can also provide a rapid determination of the intercept constant in regression models, if both the spectrum and constituent concentrations have been centered [79].

MC is performed as follows. A vector $\mathbf{x_{mean}}$, size $m \times 1$, is formed such that its j-th element is the mean of the j-th column of $\mathbf{X}$. Centered data matrix $\mathbf{X_{adj}}$ is then calculated using equation 4.9:

$$\mathbf{X_{adj}} = \mathbf{X} - \mathbf{1}_m \mathbf{x_{mean}}^\intercal \tag{4.9}$$

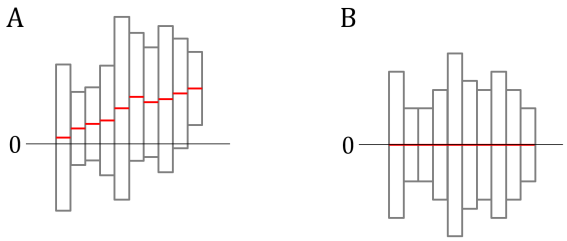

Figure 4.3: Graphical representation of mean-centering (MC). Variability in intensity at each wavenumber is denoted by a vertical rectangle, with mean intensity marked with a red line. After centering, the mean value for each wavenumber is zero.

MC has been shown to worsen a PCR model in particular situations, such as no present baseline in the data, or missing measurements dispersed throughout the set [78, 79]. Cases where MC is ill-suited are well-documented in this section's references, and a short literature review can pre-emptively qualify or exclude MC as a suitable preprocessing method for a specific case of PCR.

Smoothing

Noise in the Raman signal can greatly affect the robustness of of a PCR model. We desire a model which describes the Raman response, not the artifacts within it. Smoothing is often required to remove systematic detector noise.

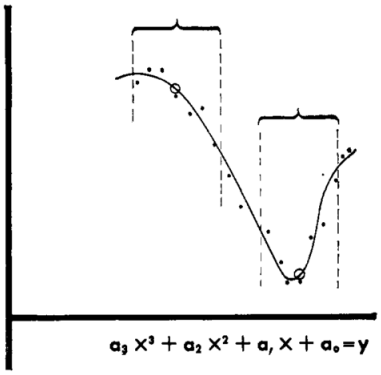

Figure 4.4: Graphical representation of Savitzky-Golay (SG) smoothing. Each block of seven data points is fitted to a function y as shown. The signal at centre point x is replaced by the value of $y(x)$, indicated by an open circle. The process is repeated for the next block of seven data points. Adapted with permission from [80]. Copyright 1964 American Chemical Society.

Savitzky-Golay (SG) is one of the most widely-used smoothing algorithms [73]. A moving window of points is successively fitted to a polynomial using the method of least squares, illustrated in figure 4.4. Each point in the data set is evaluated and replaced by the value of the polynomial which provides the best fit to the group of points currently inside this moving window [80]. The SG algorithm is well-suited to removing noise, but it can negatively affect the spectrum in the vicinity of sharp peaks. These modes may become distorted if the polynomial order is insufficient or the window too wide, clipping some amplitude from the peak tip. The size of the moving-window and polynomial degree must therefore be optimized on a case-to-case basis.

Differentiation

Differentiation can compensate for certain systematic trends in a spectrum. Just as taking the first derivative of a function will remove a scalar constant, an offset baseline is removed with the first derivative of a spectrum. Likewise, a linearly sloped baseline is removed via the second derivative, and so on [73]. Manual baseline removal requires that the operator use their best judgment to decide if a region of the spectrum is a baseline, or a collection of broad peaks. Derivatives can alleviate some of this ambiguity, suiting it for inclusion in a system designed to be accessible for non-expert users.

No single preprocessing method will universally improve PCR. In each case it is paramount to consider the data set's distribution and opt for a method which corrects unwanted artefacts without introducing new ones. A statistical technique which we have developed to speed up the assessment of a preprocessing method's suitability will be discussed in section 4.4.

4.3.2 Baseline Correction via Principal Components

The PCs of a data set are formed as function of the data, and as such can represent experimental artefacts such as spectral features like baseline shift. This can be used to our advantage in order to perform a baseline removal.

A collection of similar spectra often includes slight variation in the baseline. As the PCs represent variance in the spectra as a whole, we can use this to decompose spectra $\mathbf{X}$ into two separate components: one for the signal due to Raman scattering ($\mathbf{S}_R$) and one for the signal due to baseline shift ($\mathbf{S}_B$).

Extending this logic, we can express the PCs themselves as having the same two components. The PCA equation for $\mathbf{X}$ may be rearranged as follows:

$$\begin{aligned}\mathbf{X} &= t_1 p_1 + t_2 p_2 + ... \\ &= t_1(p_{1,R} + p_{1,B}) + t_2(p_{2,R} + e_{2,B}) + ... \\ &= (t_1 e_{1,R} + t_2 e_{2,R} + ...) + (t_1 e_{1,B} + t_2 e_{2,B} + ...) \\ &= \mathbf{S}_R + \mathbf{S}_B\end{aligned} \tag{4.10}$$

$$\mathbf{S_R} = \mathbf{X} - \mathbf{S_B} \tag{4.11}$$

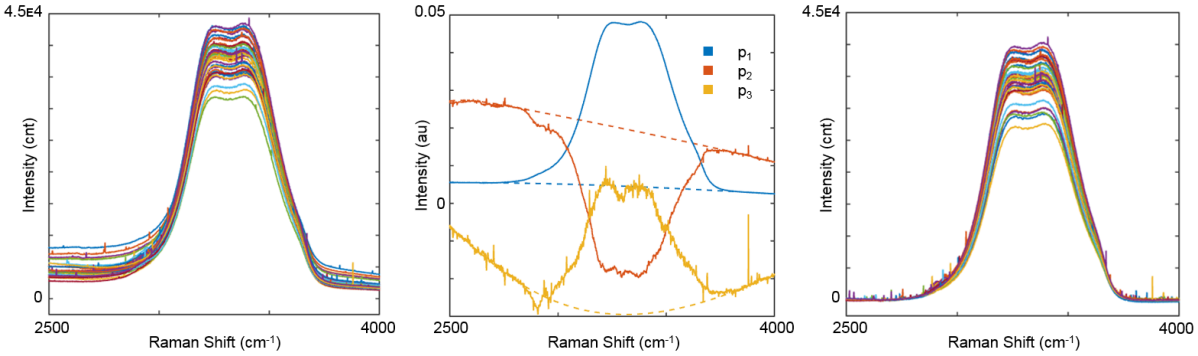

Figure 4.5: Baseline removal from a data set, using principal components (PCs). Left: Collection of 39 spectra, each containing some degree of systematic baseline shift. Middle: First three loading vectors (solid), with their respective fitted baselines (dashed). Right: Collection of 39 spectra after the fitted baselines are subtracted using equation 4.11

As shown in equations 4.10 and 4.11, an individual baseline for each loading vector allows us to subtract off that portion of the spectra, once the scores are known. This technique can be applied in isolation to one sample with multiple measurements and a consistently present but varying baseline, or to a group of spectra as a whole rather than fitting the baseline for each spectrum individually. The process is illustrated in figure 4.5: the method greatly expedites preprocessing in a large data set and allows the user to prioritize analysis.

4.3.3 Independent Interference Reduction

Throughout our analysis, a technique which has proved extremely useful for removing unwanted portions of a data set is independent interference reduction (IIR) [81]. Introduced in 2001, IIR is suited to sets of spectra in which the component of interest is present in low concentrations, and whose Raman signal may be masked by more dominant components. In this case many spectra may be required to form a robust model for PCR, so an alternative solution is desired which reduces the number of calibration spectra needed.

IIR requires two data sets: $\mathbf{X_{simple}}$ which has variation in all parameters except the one of interest, and $\mathbf{X_{special}}$ which has variation in all parameters. It is performed as follows:

1. Obtain PCs from $\mathbf{X_{simple}}$

2. Project spectra from $\mathbf{X_{special}}$ on to the PCs from $\mathbf{X_{simple}}$ to obtain a matrix of scores
3. Subtract the projections from $\mathbf{X_{simple}}$, leaving behind only parts of the spectra which are not described by the PCs.

The PCs from a data set describe its variation. Thus, when the component of interest is either absent or is present in constant quantities, it should not be described by the PCs. The residual which remains following step 3 should reveal the spectrum of the component of interest. Figure 4.6 illustrates the procedure of IIR, and the spectrum it reveals. Interference reduction was applied to a spectrum whose sample composition is 10% Isopropyl-alcohol, 80% Intralipid fat emulsion, 10% Deionized Water (% v/v). Composition of samples for $\mathbf{X_{simple}}$ and $\mathbf{X_{simple}}$ are provided in tables 4.2 and 4.3.

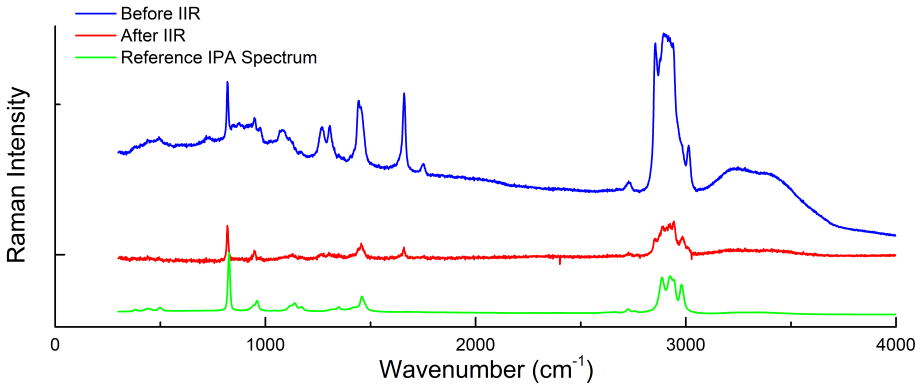

Figure 4.6: The process of independent interference reduction (IIR). Sample composition is 10% isopropyl alcohol (IPA), 80% Intralipid fat emulsion, 10% deionized water (DIW) (% v/v). The parameter of interest is IPA, whose reference spectrum is plotted for comparison to the sample's spectra before and after it has been interference-reduced.

Table 4.2: Composition of samples in $\mathbf{X_{simple}}$

Concentration (% v/v)		
Intralipid	**IPA**	**DIW**
75	5	20
80	5	15
85	5	10
90	5	5
95	5	0

4.4 Statistical Determination of Principal Components and Model Pre-Processing

To most effectively perform PCR, the number of PCs must be determined which minimize computation time while maximizing PCR prediction accuracy. In addition, a preprocessing step is often necessary to remove insignificant sources of variation and further improve the regression model. The number of possible combinations of PCs and preprocessing methods rapidly becomes prohibitive to assess, particularly

Table 4.3: Composition of samples in $\mathbf{X_{special}}$

Concentration (% v/v)		
Intralipid	**IPA**	**DIW**
80	15	5
75	20	5
65	25	10

for large data sets. We have developed a two step process, consisting of cross-validation followed by a statistical F-test, to quickly determine the optimal combination of PCs and preprocessing methods.

Unlike PCA and PCR, cross-validation is not a function of the data set, but rather the predictive potential of the model [82]. We have chosen leave-one-out cross validation (sometimes called row-wise cross validation in literature) to assess the predictive ability of PCR models. It is an excellent tool to account for sample-specific errors and generate a reproducible predictive model [70]. Though it can be computationally expensive in large data sets, we demonstrate how it can be used in conjunction with a statistical F-test to pre-emptively reject data pre-treatment methods which lead to an ineffective model.

Full leave-one-out cross-validation begins with the matrix $\mathbf{X}$, calibration spectra whose concentrations are known. In turn each spectrum is removed and the remaining $n-1$ spectra are used to predict the composition of removed spectrum using 1 through $n-2$ PCs. Exceeding $n-2$ PCs presents the possibility that each spectrum forms its own basis vector, negating PCA dimension reduction. Following PCR, error is calculated using predicted residual sum of squares (PRESS) as in equation 4.12. Note that $\mathbf{C}$ and $\mathbf{C_{est}}$ are vectors sized $q \times 1$ during cross validation.

$$PRESS = \sum_{i=1}^{q} (\mathbf{C_{est},}_i - \mathbf{C}_i)^2 \tag{4.12}$$

Cross-validation yields a matrix sized $n \times k$ of PRESS values. On this we perform a statistical F-test to compare variability within one PC to that between different PCs [77]. An F-test gives a statistical measure of whether differences in prediction are meaningful or simply due to sampling. This is essential during cross-validation in order to assess future applicability of the model.

Significance determination begins with the null hypothesis (H_0) that the mean PRESS values for each PC are equal, and an alternative hypothesis (H_a) that they are not all equal. A measure of the variability within each PC is first required. This is explained using a modified sum of sum of squares of errors (SSE) (equation 4.13). The modification comes about due to equal sample size within each PC, allowing term which corrects for this to be factored out. Secondly, we require a measurement for the variation caused by using different PC. This is explained using the sum of squares of treatmentss (SSTs) (equation 4.14).

$$SSE = \sum_{j=1}^{k} \sum_{i=1}^{n} (x_{i,j} - \overline{x}_j)^2 \tag{4.13}$$

$$SST = n \sum_{j=1}^{k} (\overline{x}_j - \overline{x})^2 \tag{4.14}$$

An F-statistic (equation 4.15) is determined from SST and SSE, after normalizing each factor by

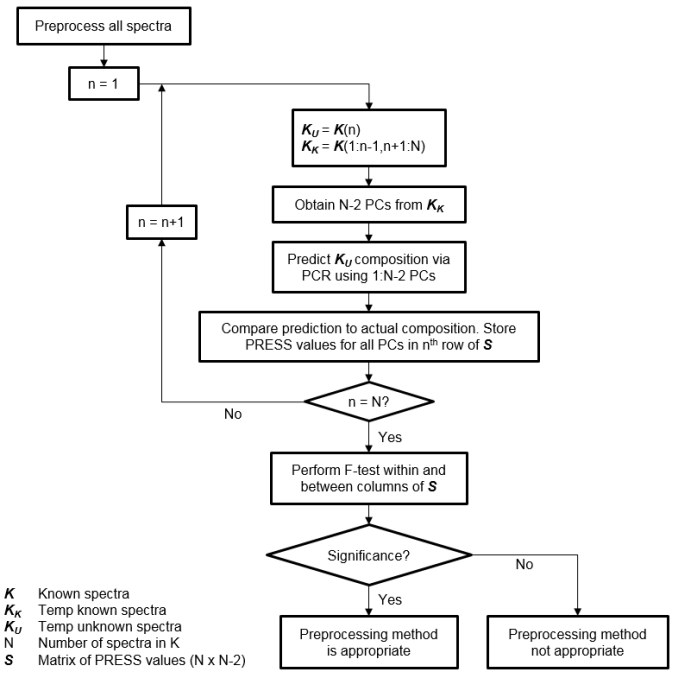

Figure 4.7: The flow chart of preprocessing statistical significance algorithm.

their respective degrees of freedom.

$$F = \frac{SST/(k-1)}{SSE/(n-k)} \tag{4.15}$$

Statistical significance of F is determined by referencing a table of values for a chosen significance level α, which represents the probability of erroneously rejecting the null hypothesis. If $F > F_\alpha$ we reject H_0. In our custom analysis interface (chapter 5), F-test computations and significance determination using equations 4.13-4.15 are performed with MatLAB's `anova1` function from the Statistics and Machine Learning Toolbox at a significance level of α=0.05. The full algorithm is outlined in figure 4.7.

When using a different number of PCs leads to a statistically significant difference in concentration prediction ($F > F_\alpha$), we single out the PCs which show significance relative to the PC with highest prediction error. From this subset we select the PC with the lowest product of error in prediction and measure of significance to be the optimal PC for a regression model. In the case that we fail to reject H_0 the user is alerted and we opt for the PC with lowest PRESS value. We have observed that a lack of significance is not a function of the data set itself. Instead it indicates an inappropriate selection in preprocessing treatment. Thus this technique allows us to immediately reject a preprocessing method and rapidly proceed to the processing techniques most suited to the particular data set. Figure 4.8 illustrates this point. All plots begin with an identical data set. The data in the left plots is preprocessed using first derivative and the data in the right plots is preprocessed using baseline removal and RNV at the 90^{th} percentile. A difference in pre-treatment method leads the second plot to significantly greater variation in predictions as a function of the number of PCs. To demonstrate the statistical determination algorithm's efficacy we plot these PRESS values in the top row compared to the actual residual sum of squares (RSS) of the unknown spectra in the bottom row. A red circle indicates the optimal PC as indicated by our algorithm.

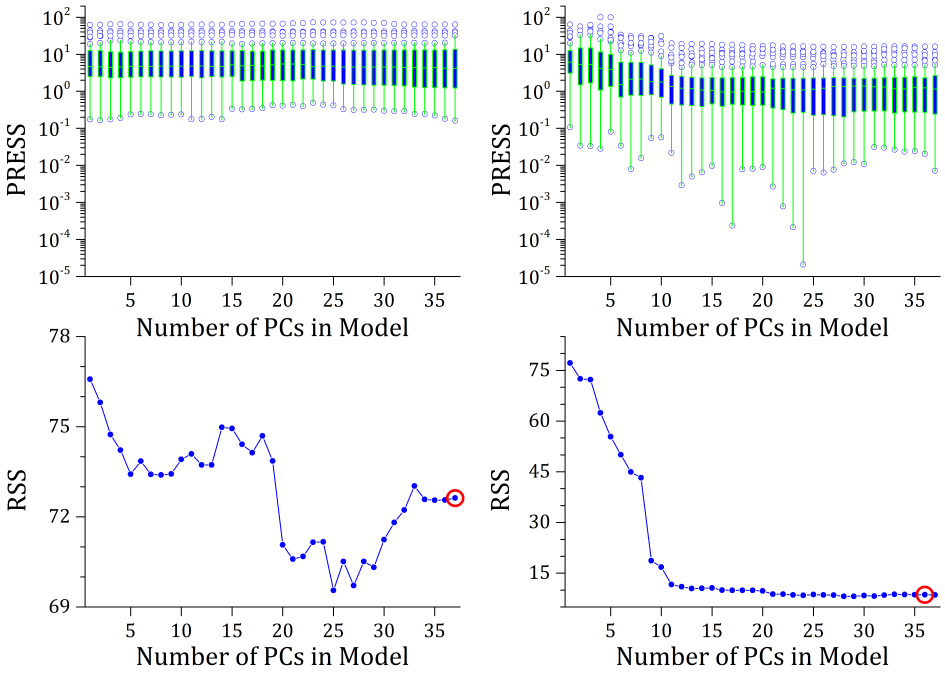

Figure 4.8: Variation within predicted residual sum of squares (PRESS) values for each number of principal components (PCs), caused by using a different Raman spectra as the unknown in a cross-validation training model. Top Left: Spectra preprocessed using the first derivative. Little change is observed in PRESS values as the number of PCs is altered, indicating that the preprocessing method is ill-suited for a principal component regression (PCR) model. Top Right: Preprocessing using baseline removal and robust normal variate transform (RNV) at the 90^{th} percentile. As the number of PCs is altered, PRESS values consistently improve significantly. We expect that this pre-treatment method will yield a well-performing PCR model. Bottom: Actual residual sum of squares (RSS) values for the data sets above. The optimal PC as identified by our algorithm is outlined in red.

Variability in the PRESS matrix will occur in two dimensions: for each spectrum which acts as the unknown in the cross validation model there will be variation as a function of the number of PCs, and within each PC there will be variation as a function of the spectrum which is used as the unknown. We demonstrate this variability using a box plot. A filled rectangle shows the interquartile range, the area between 25th and 75th percentiles, with the median value marked within. A thin solid line extends to the minimum and maximum points which are not considered outliers, which are depicted as open circles and defined by the criteria that they lie further from the 25th or 75 percentile than 1.5 times the interquartile range [77].

Chapter 5

Custom Processing Interface

To facilitate a complete analysis system for optofluidic Raman spectroscopy, one of the products of this thesis is a custom GUI. The GUI facilitates many routine processing steps which otherwise require significant manual intervention.

Simply importing a collection of spectra for normalization by SNV and plotting requires:

1. Import the files containing the spectral data into a matrix
2. Identify wavenumber and amplitude dimensions within the data matrix
3. Normalize all spectra to a consistent wavenumber domain and interpolate the amplitude responses to match
4. Calculate the mean of each spectrum
5. Subtract the mean from each amplitude point within a spectrum, and divide each value by the mean
6. Plot wavenumber versus normalized amplitude response.

A purpose-built GUI reduces the above process to a few mere mouse clicks, making the process more accessible to non-expert users and allows the operator to focus on meaningful analysis rather than menial data processing. The GUI is programmed in and runs on MATLAB versions R2015a and newer.

5.1 Graphical Interface Introduction

The GUI contains three primary classes of functions: iterative peak fitting, manual spectrum alterations, and principal component analysis and regression. Each of these classes of functions will be discussed in detail in sections 5.2-5.4. This section will give a brief introduction to the interface and the role of each component in facilitating Raman analysis of fluidic samples which is straightforward for both experienced and non-expert users alike.

The initial GUI screen is shown in figure 5.1. A complete data set complete with previously defined concentration and preprocessing treatments may be retrieved by selecting `Load Data Set`. Spectra may be added to the GUI using `Select Spectra`. In this case the user is given the option to either replace all loaded data, or append to the set. Individual spectra may be re-classified as 'known' or 'unknown', allowing the user to evaluate the robustness of a PCR model when presented with different amplitude responses. These features give the user the ability to work with an evolving data set, working towards

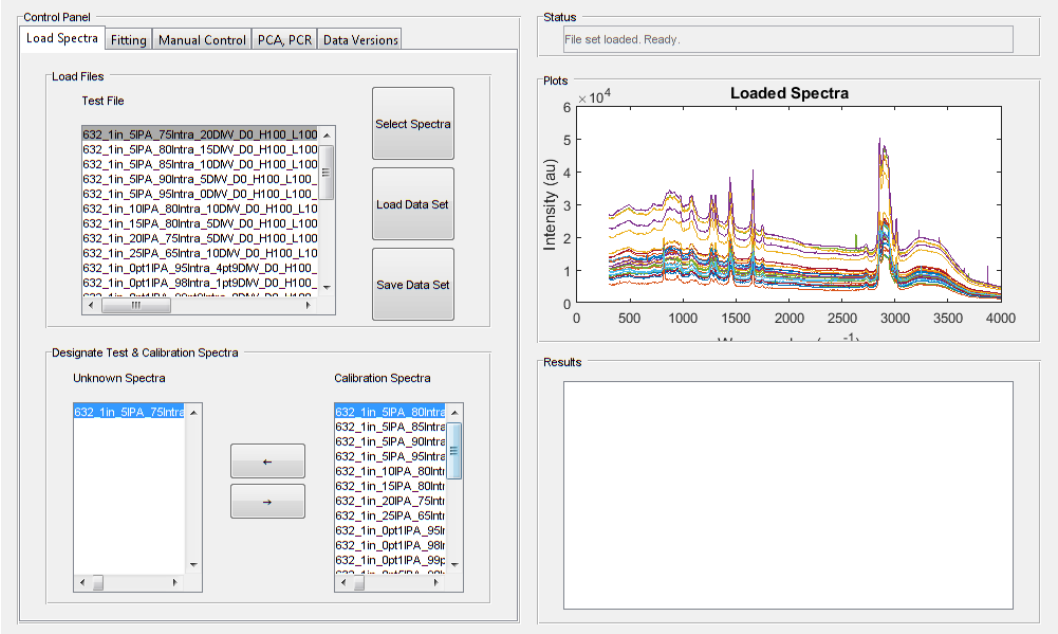

Figure 5.1: Loading spectra files or data sets, and classifying them as either 'known' or 'unknown' for principal component regression (PCR) purposes.

strengthening a regression model or comparing several processing methods from a common initiation point. Over time we wish to streamline the techniques which lead to an optimal model for predictive analysis; providing to the ability to observe treatments which consistently succeed or fail for a particular collection of spectra presents the opportunity accomplish this.

5.2 Manual Control

Four manual processing elements are incorporated into the GUI: wavelength range selection, peak assignment, preprocessing, and baseline removal. Each technique is saved along with a data set from the main GUI page so that they can be preserved for future processing sessions.

5.2.1 Wavelength Range Selector

Certain regions of the Raman spectrum may be more prone to systematic noise, interference, or fluorescence. In some cases specific wavenumber region selection can significantly improve specificity in spectroscopic regression models [83, 84]. PCR results may be improved by choosing to include only regions of the spectrum whose variation is relevant.

5.2.2 Manual Peak Assignment

Broad Raman modes may be difficult for a peak fitting algorithm to assign - particularly if they occur in the neighbourhood of another mode. As such, manual intervention may be required to assign the initial parameters in the peak fitting search algorithm, or to expedite the process if a peak in the spectrum is already known.

5.2.3 Preprocessing

PCs are highly sensitive to outliers in the data set and may unintentionally correlate with experimental artifacts such as a fluorescent background, detector noise, and drift-based amplitude variations. Thus PCR's capability to repeatedly provide reliable and meaningful predictions can be significantly hampered by the presence of these spectral features, which are omnipresent in Raman spectra obtained from real-life biofluids. Correcting and accounting for artifacts is of particular importance in biological analysis where samples are inherently variable from one patient to the next [85]. Compensating for these aberrations with a preprocessing step can drastically improve PCR's ability to form a robust model.

Normalization algorithms SNV and RNV, as well as the preprocessing methods MC and SG, previously discussed in section 4.3, are built in to the GUI. In addition to these methods, the GUI includes functions to take spectrum derivatives and remove cosmic spikes.

SG smoothing can have a negative impact on regions of the spectrum with sharp peaks, if the algorithm is not properly configured in regards to window width and polynomial number. These decisions rely on user experience to select parameters which will sufficiently conform to the shape of a narrow peak, without fitting to noise. As a compromise, for non-expert users we have additionally included a moving-window cosmic ray filter. Each amplitude value in the spectrum is evaluated to determine if it is an outlier relative to a window of points centered on the value.

5.2.4 Baseline Removal

To accomplish consistent and reliable data processing for both experienced and non-expert users, we have prioritized the integration of a completely or semi-automated baseline removal algorithm. In particular we sought a method capable of fitting either the spectrum itself or the loading vectors of a group of spectra, allowing it to be used for our batch-baseline removal technique which was previously discussed in section 4.3.2. The search for an optimal method is complicated by the fact that peaks in loading vectors may fall either above or below the baseline. Here we will provide an overview of several automated algorithms under consideration.

Iterative Polynomial Smoothing

The first baseline fitting method was developed to address challenges in biomedical Raman spectroscopy [86]. An autofluorescent background may overpower the Raman signal, but polynomial fitting to remove this baseline may introduce arbitrary effects due to user-dependent selection. The modified multi-polynomial fitting algorithm addresses this by repeatedly fitting the spectrum to a polynomial and truncating the most extreme peaks [86].

1. Fit input spectrum (O) to a polynomial (P)
2. Calculate the residual (R = O - P)
3. Calculate the standard deviation of R (σ)
4. Where O > P + σ, replace with O = P + σ
5. Return to step 1. Terminate when further iterations do not continue to improve σ

Ultimately this method cannot truly operate independently of a user; it requires a manual decision of the polynomial order for the baseline. Additionally, it does not perform well on spectra with multiple overlapping peaks. Most biofluids of diagnostic interest are aqueous, containing broad water modes

between 3000cm^{-1} and 3600cm^{-1}. We have observed that this algorithm often confuses these modes with a baseline, making it ill-suited for our primary intended use. These water modes can be observed in figures 4.2 and 4.6. Despite this, the algorithm has potential for baseline fitting of loading vectors (section 4.3.2) which do not tend to contain broad peaks; the algorithm can easily be modified to replace sections of the spectrum both above *and* below the baseline region plus σ.

Mathematical Morphology

The second baseline fitting method under consideration is based on mathematical morphology operations of erosion and dilation, coupled with a smoothing spline [87]. Erosion and dilation are the result of the interaction between a spectrum and a structuring element that defines a neighbourhood around which each data point will be evaluated. Both erosion and dilation center the structuring element on a data point of the original function. Erosion replaces the data point with the minimum value of the function found within the structuring element. Dilation performs the opposite: replacing the data point with the maximum value of the function found within the structuring element. These processes are depicted in figure 5.2 using a structuring element which is a window of 100 data points.

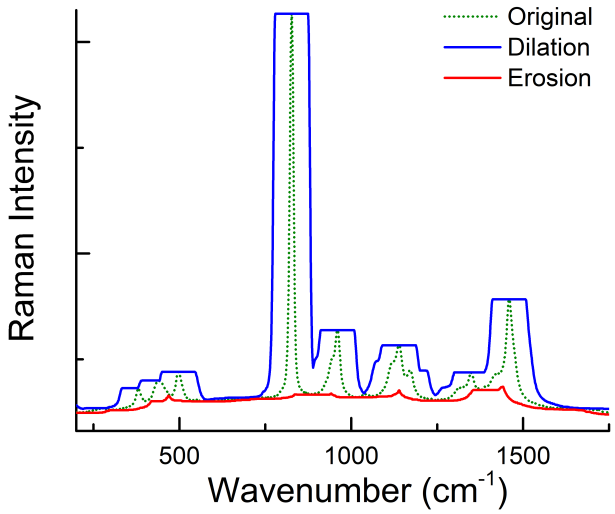

Figure 5.2: Erosion and dilation operations on a Raman spectrum of an 100% isopropyl alcohol (IPA) solution.

Subsequent applications of erosion and dilation serve to connect nearby elements along the baseline, removing positive peaks. The morphology method was ultimately deemed unsuitable for our use. Similar to iterative polynomial smoothing, the morphology algorithm does not perform well in spectral regions with broad or overlapping peaks [86]. Local minima in between overlapping modes are often deemed to be baseline points, distorting the peaks upon removal.

Iterative Curve Fitting

The method of automated baseline fitting which was adopted in the GUI is a genetic algorithm which simultaneously fits spectrum peaks and baseline by pseudo-randomly mutating peak parameters in order to minimize the residual [88].

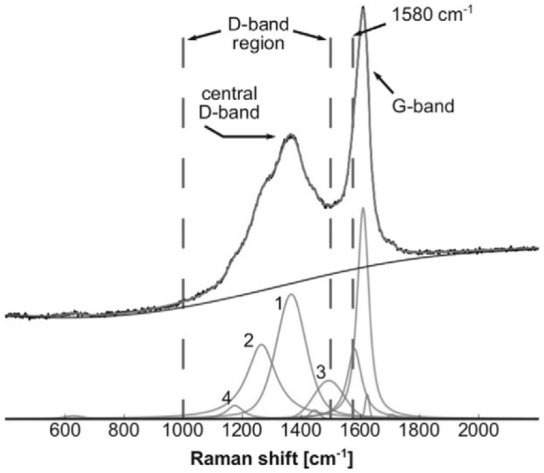

Figure 5.3: Iterative baseline and peak fitting algorithm. Reprinted from [88], with permission from Elsevier.

Iterative fitting of Raman spectra (IFORS), named by its authors, outperforms each method of automated baseline removal which we assessed. Broad regions of many overlapping peaks are not an issue, as depicted in figure 5.3. IFORS repeatedly iterates through three main steps:

1. Remove a baseline estimate and any peaks which are known or have previously been estimated
2. Analyze the residual and add new peak possibilities
3. Randomly mutate peak intensity, position, width, and shape parameters to further reduce the residual

Manual baseline removal

After careful consideration of many automated baseline removal algorithms, we opted to include a manual baseline fitting routine alongside any automated algorithms. A manual feature allows the user to bypass the peak fitting routine, which may be unnecessary. Although manual baseline correction introduces user-dependent variation in a data set, this can be mitigated to a degree by incorporating the method of removing baseline via principal components, described in section 4.3.2. Separating a data set into its principal components can isolate peak groups which are otherwise overlapping, making the baseline more apparent.

The manual baseline correction method in the GUI can function either on the spectra themselves or the PCs. The operator is prompted to select a series of anchor points which lie on the baseline, and a smooth curve is interpolated between them.

5.3 Peak Fitting

The automated baseline fitting algorithm IFORS was chosen for our GUI due to its ability to simultaneously fit both a baseline and Raman modes [88]. It is also crucial that the algorithm is able to resolve overlapping Raman peaks. Biological samples contain a dazzling array of Raman-active molecules; proper diagnosis necessitates the ability to reliably discern relative changes in Raman modes.

Each Raman mode in the fitting routine is described by a pseudo-voight function (pV, equation 5.1) whose parameters are stored in the rows of a model matrix (MM) [88].

IFORS begins by normalizing the spectrum and repeatedly iterating through the following steps:

1. Remove a baseline estimate and peaks in the MM.
2. Analyze the residual and extend the MM to include new peaks.
3. Mutate the elements in MM in an effort to further reduce the residual.

$$pV = I_0 \left(\frac{\eta}{1 + \frac{(x-x_0)^2}{w^2}} + (1-\eta) e^{\left(-ln(2) \frac{(x-x_0)^2}{w^2} \right)} \right) \tag{5.1}$$

I_0 : Peak amplitude
η : Shape factor
x_0 : Peak center
w : Peak half-width

$$MM = \begin{bmatrix} I_{0,1} & \eta_1 & x_{0,1} & w_1 \\ I_{0,2} & \eta_2 & x_{0,2} & w_2 \\ \vdots & \vdots & \vdots & \vdots \end{bmatrix} \tag{5.2}$$

Each mutation randomly selects an element in MM and alters it by a value δ, drawn from a normal distribution whose standard deviation is controlled by the corresponding element in a sigma matrix (SM). SM is maintained with the same dimensions as MM and new entries are initialized with default values. The element which is randomly selected for mutation is determined by converting SM into a probability density function.

If the new mutated value further minimizes the residual, it is accepted and replaces the value in MM. The corresponding element in SM is increased slightly by dividing by α, where $\alpha < 1$. Since the mutation had a positive effect on the model, it is assumed that further alterations of comparable magnitude will perform similarly. Increasing the value of the element in SM increases the probability that it will again be selected for mutation.

If the new mutated value does not minimize the residual, it is rejected and MM remains unchanged. The corresponding element in SM is reduced slightly my multiplying it by α. As the mutation did not have a positive effect, we proceed under the assumption that either finer modifications are required, or that the value of the parameter is already optimized. Decreasing the element in SM ensures that future mutations occur with smaller values of δ, and that the element has a lower probability of being selected for mutation.

Parameters required for peak and baseline fitting using IFORS are configurable in the GUI, shown in figure 5.4.

We have made several modifications to IFORS in order to suit the specific needs of our GUI. The user may choose to perform peak fitting alone, or to fit the baseline as well. Additionally, the algorithm may be run on the spectrum directly, or on a number of PCA loading vectors. Our modifications will be discussed in the following subsections.

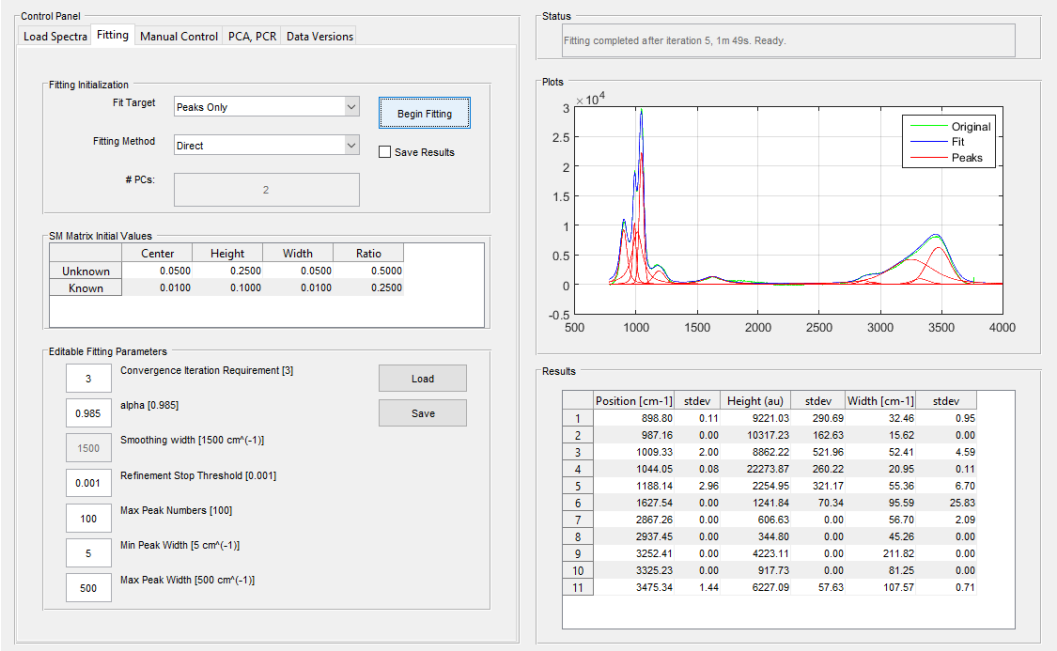

Figure 5.4: Automated peak fitting on a spectrum of 40% Sulfuric Acid 60% deionized water (DIW) (% v/v) using the graphical user interface (GUI)

SM Matrix Initial Values

IFORS was written with identical initial values for each value in the SM matrix, meaning that each peak parameter is given equal likelihood of adjustment. The element chosen for adjustment is influenced by a random number selected from the interval between zero and the sum of all elements in SM. In addition we have chosen to give the user the option to adjust the initial SM values, prompting the routine to preferentially adjust certain peak parameters over others. SM values initialize with lower values for modes that have been manually assigned which cause them to have a lower chance of being selected for adjustment relative to a mode that was assigned by the algorithm.

Editable Fitting Parameters

Convergence Iteration Requirement

Due to its intentionally random nature, the genetic algorithm will lead to slight variance in each peak parameter on every iteration. To compensate for this, we have modified IFORS to refrain from permanently including a peak in the MM until its parameters are consistent within error for a selected number of iterations. This feature provides us with a confidence level for each Raman mode as its parameters continue to be refined. This iteration requirement additionally serves to terminate the algorithm when the designated number of iterations elapse without any new peaks being transferred to the MM.

Alpha & Refinement Stop Threshold

Values within SM are modified as a function of whether a mutation successfully decreases the residual sum of squares of the spectrum as well as of its derivatives. This ensures that each peak fitting routine

strives to match both the spectrum and its points of inflection, which is crucial to compensating for a broad baseline. Each refinement iteration of the peak fitting algorithm will terminate once the sum of elements within SM fall below a threshold value. Allowing the user the option to modify these values provides them with coarse control over the number of mutations that IFORS will undertake each iteration.

In addition we have implemented a set of forbidden changes which constrains a peak mutation in IFORS. The primary function is a logical vector whose dimensions match the wavenumber indices, and which acts to forbid new peaks from being initialized or moved into regions occupied by successfully-placed peaks or into regions which are determined to contain no peaks. This is assessed as a function of the distribution of the residual in the wavenumber's vicinity. Following a successful peak mutation this logical vector is dilated using a 3-point structuring element which further urges the algorithm to look away from existing peak regions when deciding where to initialize a new peak. Morphological dilation is defined in section 5.2.4. Forbidding certain modifications also allows us to handle edge cases such as a mutation wishing to move the peak to a completely different part of the spectrum.

Smoothing Width

IFORS outperforms many semi-automated baseline fitting algorithms by not relying on the user to define a polynomial order for the baseline. Rather, we perform a wide-window low-degree SG smoothing of the spectrum in order to remove the most extreme peaks and provide an estimation for the underlying background.

Peak Width Constraint

To allow IFORS's peak fitting routine to competently include narrow peaks but exclude cosmic spikes, or to include broad Raman modes but exclude a curved baseline, we place limitations on the range of widths that a mode may occupy. These parameters, along with the smoothing width, allows the algorithm to excellently handle spectra with broad peaks, a spectrum feature which often causes other algorithms to fail.

A restriction is also placed on the number of Raman modes which may be assigned, in order to prevent runaway situations in noisy spectra.

5.4 PCA & PCR

The highlight feature of this software is the ability to perform analysis on biofluids to determine composition and perform diagnostics.

Each loaded spectra is displayed in one of two windows on on the `PCA/PCR` tab, dependent on their classification as either 'calibration' or 'unknown' spectra. By default no analytes are specified but may be added or removed using the buttons within the `Concentration Information` panel below the tables (figure 5.5). Individual concentrations may then be typed in each table. This information will follow a spectra if its known status is re-classified, and is also retained with the data set when it is saved. Concentration information for the unknown samples may be left blank. If it is specified, the regression will calculate and display the error.

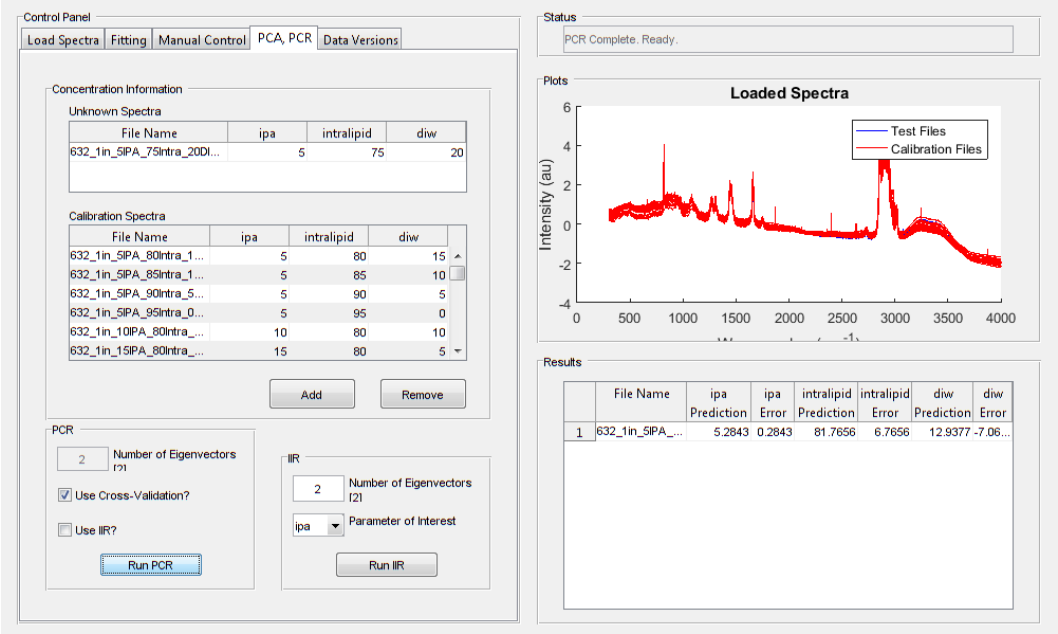

Figure 5.5: Principal component analysis and regression using the graphical user interface (GUI), on a set of spectra who have been preprocessed using standard normal variate transform (SNV)

Once concentration information is finalized the user may initialize conditions for regression in the lower right `PCR` panel (figure 5.5). The number of PCs may be specified or our statistical F-test algorithm may be used to determine the optimal number of components and assess preprocessing method suitability.

IIR is also controlled in this panel. One of the analytes present in the samples gets specified as the parameter of interest. In our implementation of IIR the GUI automatically groups spectra into respective $\mathbf{X_{simple}}$ and $\mathbf{X_{simple}}$ matrices in as many different ways as possible given the concentration information provided. The resulting interference-reduced spectrum is the mean of these different interference-reductions.

Chapter 6

Facile Experimental Usability

In this chapter we shall describe the entire process of using our noninvasive analytical monitoring system, from device fabrication to concentration determination. We will highlight the design choices which remove significant portions of operation from manual processing, and detail how the elements work together towards our end goal of reliable constituent spectrum collection and analysis with minimal user intervention or expertise.

6.1 Microfluidic Fabrication

This section will detail the process of micro-opto-fluidic device fabrication. This procedure can be carried out with variable user training and access to specialized equipment. Our microfluidic master mould is a silicon wafer patterned with 170 μm thick SU-8 2050 negative photoresist [89]. Silicon wafer master mould fabrication requires a fair amount of user-training and access to specialized equipment (table 6.1), but the mould may be re-used indefinitely. Fabrication protocol is detailed in literature [89].

Table 6.1: Specialized equipment requirements for Silicon wafer poly(dimethylsiloxane) (PDMS) master mould fabrication.

Equipment	Use
Fumehood	Ventilation of photoresist and developer
Oxygen Plasma Barrel Asher	Clean the wafer for photoresist deposition
Wafer Spinner	Produce a uniform-thickness coating of photoresist
Mask Aligner	Align the photomask to the wafer and expose it with 350 nm ultraviolet radiation

Barring access to the facilities listed in table 6.1, low-cost cleanroom-free methods are available which significantly facilitate master mould fabrication using a standard home laser printer and polystyrene thermoplastic sheets [90].

PDMS preparation and curing

PDMS (Sylgard 184 from Dow Chemical Company) is obtained from Krayden Canada, and designed to be used in a 10:1 base to curing agent ratio [91]. In fabrication we use a 11:1 ratio. The base and

curing agent are supplied in a set with sufficient volume of each component for the recommended ratio of 10:1 but we have found that slight routine measurement errors cause the curing agent to be used up first. Young's modulus of PDMS increases with the mixing ratio; we have found that high mixing ratio PDMS becomes too soft to easily insert tubing and waveguides [92]. A 11:1 ratio produces devices with sufficient rigidity to insert these components, while allowing us to fabricate the most devices from purchased supplies. 27.5g of polymer base and 2.5g of curing agent on a 4" diameter wafer produces 14 microfluidic devices sized approximately 15 mm × 15 mm × 3 mm (L × W × H).

Mixed PDMS is poured on to a foil-surrounded master mould and placed inside a vacuum chamber for 15 to 30 minutes to remove trapped air which may cause leaks inside the cured polymer. This process is illustrated in figure 6.1. This step may also be carried out with a hand-held kitchen mixer if a vacuum chamber is not accessible [93].

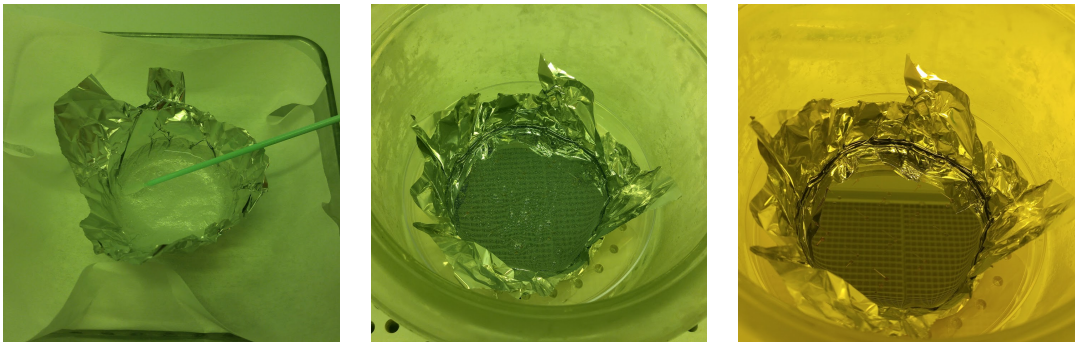

Figure 6.1: Poly(dimethylsiloxane) (PDMS) mixing and vacuum dessication process. Left: PDMS base and curing agent are mixed together thoroughly in a tinfoil vessel. Middle: PDMS mixture is poured on to the foil-surrounded silicon wafer master mould, and placed inside a glass dessicating chamber. Right: The PDMS mixture has had all bubbles and air pockets removed after 25 minutes.

Following vacuum dessication, the foil-wrapped wafer is transferred to a 150°C hot plate for 10 minutes. Alternatively the polymer may be cured at room temperature for 48 hours [91]. After cooling to room temperature the foil and PDMS are peeled from the silicon wafer mould. PDMS is placed feature-side down on to a fresh piece of aluminum foil to ensure the patterned surface remains clean. This method also makes fluidic channels easy to see with the naked eye, facilitating the process of cutting out individual devices. Figure 6.2 shows the curing and wafer-removal process.

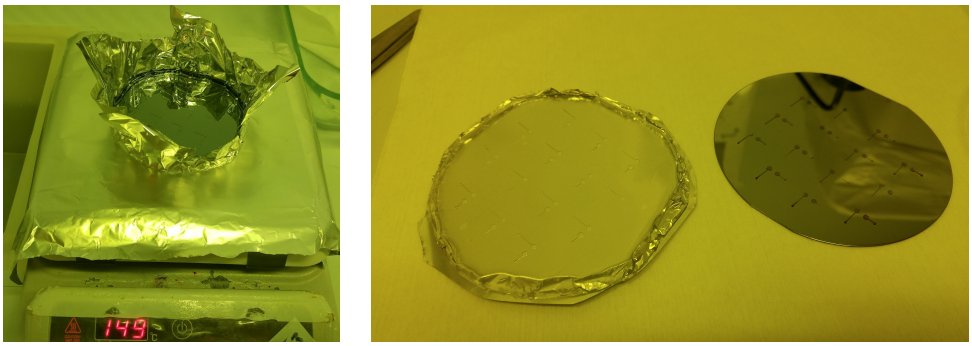

Figure 6.2: Left: Poly(dimethylsiloxane) (PDMS) curing on a hot plate. Right: Cured PDMS has been removed from the master mould and placed on a sheet of aluminum foil.

Microfluidic device assembly

Individual microfluidic devices are cut out from the cured PDMS with scissors and a biopsy punch is used to bore cylindrical holes for waveguide and tubing connections. Biopsy punches are purchased from Robbins Instruments; a 0.75 mm diameter punch is used for the TCT and a 2.0 mm punch for the tubing connections. PDMS and square glass microscope coverslips are rinsed with acetone, IPA, DIW, and dried under a stream of nitrogen. This order ensures that both polar and non-polar contaminants can be rinsed from each device surface with no residue to contaminate the sample.

PDMS is permanently adhered to glass by oxidizing each surface by plasma before bringing them into contact with each other [94]. In our experiments this is accomplished with an TePla Technics 100-E oxygen plasma asher in the Toronto Nanofabrication Center (TNFC). Pieces are exposed for 15 seconds to a plasma of 100 Watts at 0.25 Torr. An affordable alternative to an oxygen barrel asher is a hand-held corona plasma treater. This tool uses the electric field of a spark at the tip of an electrode to modify the surface chemistry of the glass and PDMS [95]. The pieces of each device are brought into contact following plasma exposure and baked on a hot plate at 75°C for ten minutes. We have found that this post-plasma bake strengthens the bond by encouraging PDMS self-adhesion. After this bake the waveguide and tubing may be inserted into the device, and fluid pumped through with high pressure without risk of detachment between the glass and PDMS. These fabrication steps are shown in figure 6.3

Figure 6.3: Left: Individual poly(dimethylsiloxane) (PDMS) devices cut from a larger disc. Middle: Post-bake following oxygen plasma exposure. Right: A completed microfluidic chip with waveguide inserted. A coin is provided for scale.

6.2 Sample Preparation and Spectrum Collection

In this section we shall detail the process of spectrum collection using microfluidic hardware and and the portable dual-syringe pump for sample recovery. Design of the 3D printed components and syringe pump are covered in section 3.2.3.

Sample Preparation and Microfluidic Setup

To prepare a fluidic sample for analysis, it is drawn into an appropriately-sized syringe with an attempt to minimize bubbles in the solution. A high proportion of bubbles or gases trapped in the solution may accumulate within the microfluidic device during prolonged sample collection. If an air pocket is

allowed to develop in the vicinity of the objective focal volume then coupling into the waveguide can be compromised, affecting spectrum enhancement.

The microfluidic device itself is prepared as in figure 6.4. Tubing and waveguide are inserted into the appropriate ports of the device, which is then placed glass-side-up on a 3D-printed microscope stage adapter. The entire adapter is then set on to the spectrometer's microscope stage and an objective used to optically align one end of the waveguide. This step particularly crucial if the solution is opaque, such as with whole human blood or intralipid fat emulsion, as the waveguide core will no longer be visible once the channels are filled.

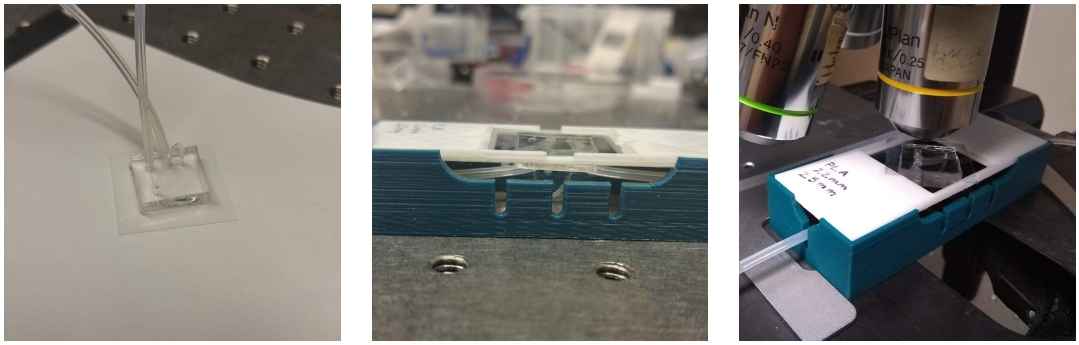

Figure 6.4: Left: tubing and waveguide inserted into a microfluidic device on a 25 mm square coverslip. Middle: The microfluidic device is inserted slide-side-up on to a 3D-printed microscope stage adapter. Narrow cutouts in the base of the adapter pinch tubing slightly allowing it to be pulled taut, ensuring that the device rests flat. Right: A microfluidic device on a 22 mm square coverslip in use on the spectrometer stage.

Syringe Pump Setup and Operation

Our portable modular dual syringe-pump, named RaMP, is illustrated in figure 6.5 in both its assembled and deconstructed forms. All 3D printed parts are press-fit together.

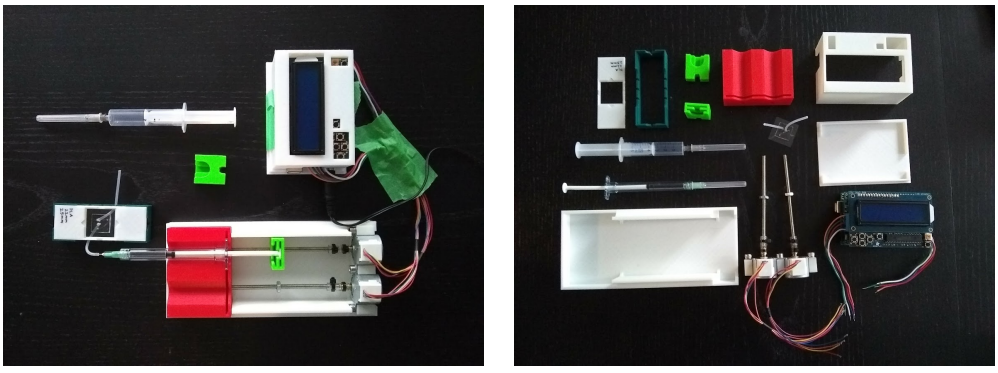

Figure 6.5: Left: assembled syringe pump and all components necessary for operation. Right: disassembled syringe pump. Individual components can be redesigned and re-printed as necessary with minimal cost using a standard consumer 3D printer. Two different syringes are pictured to illustrate that the plunger-depressor component (bright green) is sized to accommodate a range of syringes. In practice two of the same syringe must be used to ensure flow-rate matching.

Full syringe pump design and programming is detailed in section 3.2.3. Operation is designed to be

as straightforward as possible. Default parameters have a pump rate of 0.05 μL/min for a 1 mL Becton Dickinson syringe and both motors acting in opposite directions, enabling one syringe to pump and the other to withdraw. We have found this flow rate to be sufficient for mitigating the effects of laser heating during prolonged measurements of artificial human tears and a whole-blood phantom. Each individually editable parameter (and the values it may take) is outlined in figure 6.6.

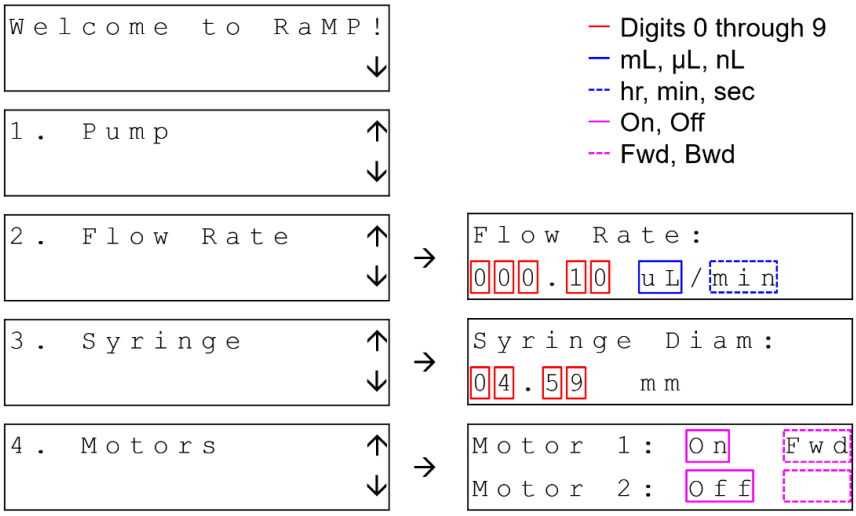

Figure 6.6: Syringe pump operation. Editable fields are outlined, and may take on the values indicated in the legend.

Once the pumping parameters are acceptable the user is only required to attach microfluidic device tubing to each syringe and start the pump. Prior to spectrum collection we obtain a rapid-series of spectra while adjusting the z-focus position of the microscope stage, to optimize the correct focal depth. The Raman spectrum can now be collected as usual.

6.3 Post-processing

In this section we shall guide the process of sample analysis using our custom software suite. This discussion shall proceed under the assumption that a set of calibration spectra whose compositions are known has previously been collected and saved to a data set.

To begin analysis the user opens the GUI and loads the data set containing calibration spectra, as detailed in section 5.1. Following this step the spectra to be analyzed are loaded and manually classified as 'unknown', as illustrated in figure 5.1. The `Manual Control` tab on the GUI allows the user to select a preprocessing method, if desired (section 5.2.3).

Prediction using PCR is initialized in the `PCA/PCR` tab on the GUI. The user may select to specify the number of PCs to use in regression, or to allow the program to determine the optimal number of factors using our statistical cross-validation algorithm. If this option is selected then the user will be alerted if the model is found to produce no statistical significance. Regression results may be saved by returning to the `Load Spectra` tab on the GUI and selecting `Save Data Set`.

Chapter 7

Biofluid Phantom Analysis

In chapter 4.4 we have developed a two step process to determine the suitability of preprocessing methods and output the optimal number of PCs for a robust predictive model. This technique is integrated in our custom GUI, described in chapter 5. A comprehensive guide to fabricate a micro-opto-fluidic device and collect a spectrum is given in chapter 6.

In this chapter we perform a thorough analysis of our statistical algorithm's performance in determining the composition of two simulated biofluids with great potential for meaningful and simplified diagnostics. Portions of this chapter have been accepted for publication, with further publications pending [1, 2].

For a given preprocessing method we perform cross-validation on a known data set and analyze the predicted residual matrix using a statistical F-test. F-tests have previously been used in biological contexts to determine the number of significant factors in a model, but not to determine preprocessing suitability [82, 96, 97]. Our approach is validated using the analysis of two fluids designed to mimic human tears and whole human blood.

To the best of our knowledge this is the first time statistical F-testing is being used to determine the suitability of a preprocessing technique and simultaneously output the optimal number of PCs for a predictive model.

7.1 Human Biofluid Phantoms

Samples to mimic human tears were comprised of lysozyme and glucose dissolved in DIW, each at physiologically relevant levels. D-(+)-Glucose (G8270) and Lysozyme from chicken egg white (62970) were purchased from Sigma-Aldrich. DIW was obtained from a Milli-Q system in TNFC. Lysozyme in human tears is can range between 0 and 10 mg/ml, and is primarily diagnostically-significant in between 2 and 7 mg/mL [47, 98]. For example, the mean lysozyme level in the tears of patients with herpes simplex virus is 2.8 mg/mL and without is 6.1 mg/mL. We must achieve an accuracy which allows us to confidently discern between these values. Lysozyme concentration in our artificial tears were chosen to reflect this range: 0 mg/mL to 10 mg/mL, with a minimum resolution of 0.5 mg/mL. Diabetes blood glucose measurements require a precision of at least 0.14 mg/mL over the range 0.7 to 4 mg/mL; glucose concentrations in human tears are approximately ten times lower than blood, so we require an accuracy of 0.014 mg/mL in the range 0.07 to 0.4 mg/mL to prove our device's capabilities for diabetic tear

glucose determination [99, 100]. Artificial tear glucose concentrations covered the range 0 mg/mL to 10 mg/mL with a minimum resolution of 0.25 mg/mL. This does not reflect the limit which we believe our device can sense and is merely a first step; future implementations of our device will be tested with finer detail in analyte concentration distribution. A full listing of all forty sample compositions is included in appendix A table A.2.

As a substitute for whole-blood we have used a 20% Intralipid fat emulsion (Sigma-Aldrich I141). The scattering coefficient of this media is a good match to that of whole blood, and it is inexpensive, non-toxic, and requires no special handling or disposal [101, 102]. Two solutes are used within intralipid: DIW and IPA. DIW was obtained from TNFC, and IPA (190764) from Sigma-Aldrich. Solutes were selected due to their availability, and to demonstrate device performance in detecting increasingly lower concentrations within an opaque solution, while reliably distinguishing Raman modes of multiple analytes. Full composition distribution is detailed in appendix A, table A.1.

All samples for human tear biophantoms were prepared from common stock solutions, and likewise for whole-blood phantoms. In addition, an effort was made to achieve similar spectrum collection conditions across each data set. As such, the variance in our spectra does not reflect the range which we should expect from real biological samples. Our experiments are a necessary first step towards real-world application, but future implementations of this device will require testing on larger spectrum sets which do not come from the same data distribution, and which have a greater degree of variation in measurement conditions.

7.2 Statistical Principal Component Selection Algorithm Performance on Simulated Biofluids

Here we aim to demonstrate that our technique is capable of reliably producing a robust predictive model in artificial human tears and a whole-blood phantom solution. We shall compare PCR model performance in the case where pre-treatment produces statistical significance in cross-validation, to the case where a preprocessing method is not found to produce significance. The full statistical algorithm is presented in figure 4.7. Within each set K of Raman specta, one spectum K_U acted as the unknown and cross-validation was performed on the remaining K_K, in order to assess the suitability of different preprocessing methods to predict K_U's composition. One spectrum is present for each unique combination of analyte concentrations. In every model present in this paper, $K_U \in K$ and $K_K \subset K$, but $K_U \notin K_K$. To demonstrate the algorithm's efficacy we plot the PRESS values compared to the actual RSS of the unknown spectra. In each case we shall demonstrate that our technique is superior at identifying a suitable a pre-treatment method and number of PCs for an optimal PCR model.

Whole-Blood Phantom: Significance

Figure 7.1 depicts a case in which the preprocessing method shows statistical significance; cross validation model accurately predicts true performance. A Raman data set of 27 unique solutions were designed to mimic optical properties of whole human blood and comprised of intralipid, DIW and IPA. A full list of sample composition is listed in appendix A, table A.1. The unknown sample is composed of 5% IPA, 85% Intralipid, 10% DIW; a cross-validation set is formed of the remaining 26 spectra. Preprocessing treatments applied were RNV at the 75th percentile after baseline removal. Some spectra in the data

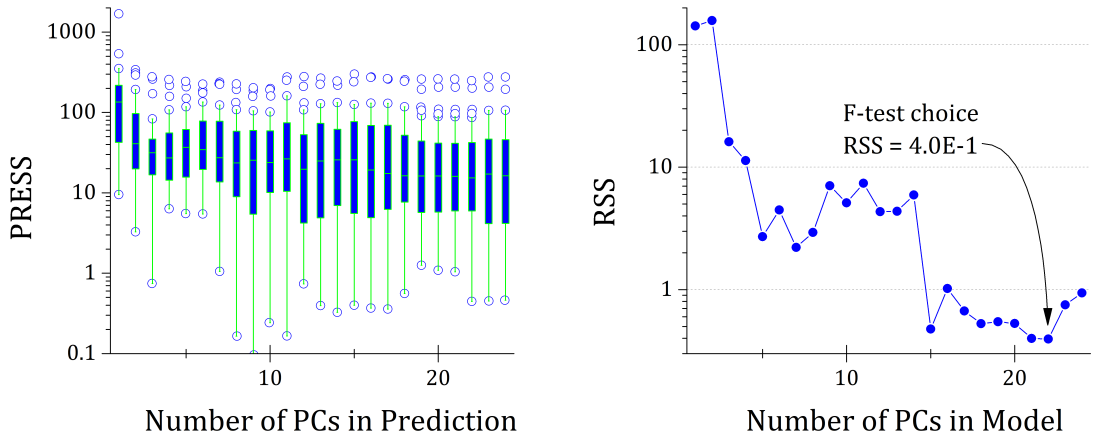

Figure 7.1: Intralipid solution, preprocessed with robust normal variate transform (RNV) (percentile 75) and baseline removal. Predicted residual sum of squares (PRESS) values of cross-validation using 26 spectra (left) display significant variation with the number of principal components (PCs), and identifies 22 PCs for the regression model which is a minima in observed residual sum of squares (RSS) (right).

set were collected with longer exposure times, so amplitude normalization is necessary.

The box plot predicts an improvement of up to one order of magnitude of the median residual prediction. In addition, there are never more than four outliers for each PC during cross-validation. This data set passed the cross-validation test, and our F-test algorithm returned 22 as the optimal number of PCs for the data set based on the PRESS matrix significance. Predicted concentrations with the model are 5.1%, 84.6%, 9.5% respectively. The optimal PC value returned is indeed the minimum within actual RSS values, so we confirm the validity of the model formed with this preprocessing treatment.

Whole-Blood Phantom: No Significance

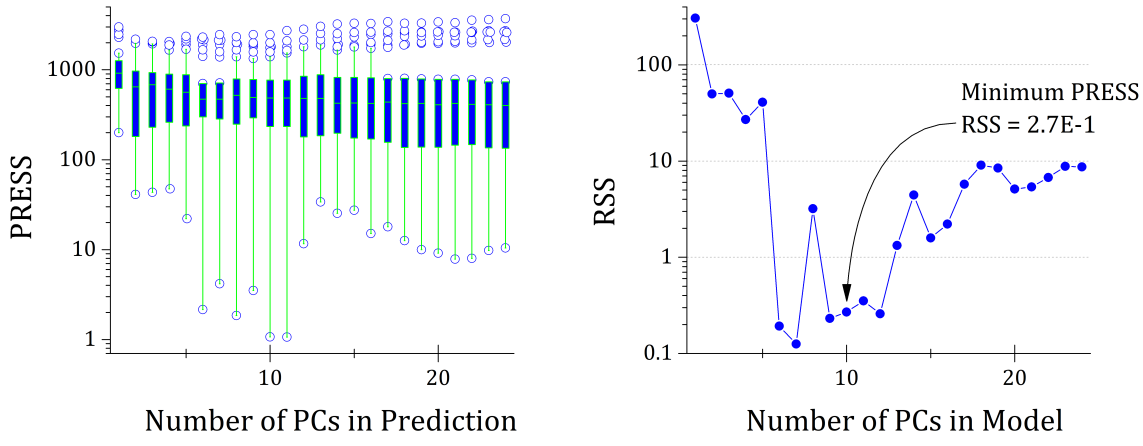

Figure 7.2: Intralipid solution, preprocessed with Savitzky-Golay (SG) smoothing and 2 derivatives. Predicted residual sum of squares (PRESS) values of cross-validation using 26 spectra (left) do not significantly improve or worsen with the number of principal components (PCs). Choosing the PC with minimum sum of PRESS values does not lead to a model which minimizes observed RSS (right).

Figure 7.2 depicts a case in which the preprocessing method fails the significance test; cross validation model fails to return true RSS performance. Solutions in this data set were taken from a set designed to mimic whole human blood; true concentration of the unknown sample is 10% IPA, 85% Intralipid, 10% DIW. A unique set of 26 samples formed the cross-validation set. Preprocessing methods were SG smoothing and second derivative. The box plot shows the median residual prediction improves by only one half order of magnitude as the number of PCs are varied. This preprocessing method did not pass the significance test. We select the PC with lowest sum of PRESS values (10) as the optimal number for the model, but using 6, 7, 9, or 12 PCs would have yielded lower RSS. The minimum sum of PRESS values is not a minima within actual RSS values; this preprocessing method's cross-validation model fails to identify four PC values which would further optimize the PCR model. Predicted concentrations with the model are 10.3%, 85.4%, 5.3%.

Artificial Tear Solution: Significance

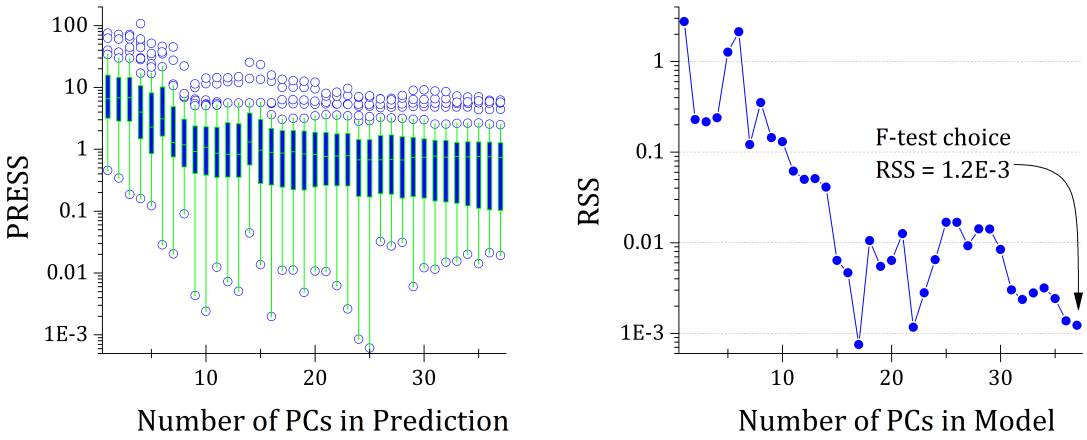

Figure 7.3: Artificial tear solution, preprocessed with baseline and cosmic spike removal. Predicted residual sum of squares (PRESS) values of cross-validation using 39 spectra (left) significantly improve with the number of principal components (PCs), and the algorithm identifies 37 PCs for the regression model which is a minima in observed residual sum of squares (RSS) (right).

A second case in which the preprocessing method shows statistical significance and cross validation predicts true RSS performance is illustrated in Figure 7.3. 40 samples were designed to mimic human tears and consisted of DIW with varying concentrations of lysozyme and glucose, at physiologically relevant levels. A full list of sample composition is listed in appendix A, table A.2. The solution with 0.5 mg/mL glucose and 0.5 mg/mL lysozyme is used as the unknown sample to be predicted; remaining 39 samples from the data set in appendix A table A.2 are used to form the cross-validation model. Spectra have been preprocessed using a baseline and cosmic spike removal. Again we see more than one order of magnitude improvement in the median residual prediction. This data set passed the significance test and returned 37 as the optimal number of PCs. Predicted concentrations are 0.48 mg/mL and 0.52 mg/mL. The predicted optimal number of PCs is a local minima in actual RSS, validating the model and preprocessing method.

Artificial Tear Solution: No Significance

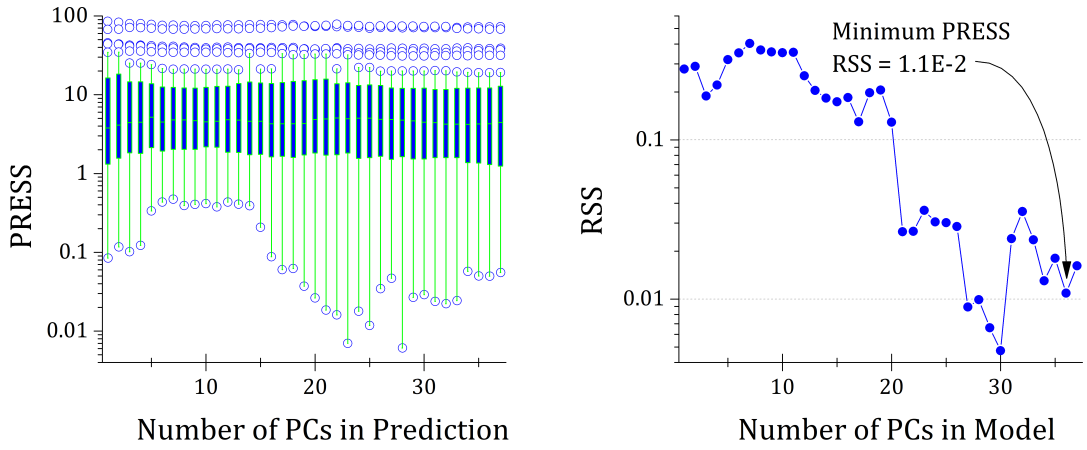

Figure 7.4: Artificial tear solution, preprocessed with Savitzky-Golay (SG) smoothing and 2 derivatives. Predicted residual sum of squares (PRESS) values of cross-validation using 39 spectra (left) neither significantly improve nor worsen with the number of principal components (PCs). Choosing the PC with minimum sum of PRESS values does not minimize observed residual sum of squares (RSS) (right).

Preprocessing fails to produce statistical significance in figure 7.4, leading to a predicted optimal PC which does not optimize the PCR model. Actual composition is 1 mg/mL glucose and 1 mg/mL lysozyme; cross-validation model is formed from the remaining 39 samples listed in appendix A table A.2. Preprocessing methods were SG smoothing and second derivative. Residual prediction improves by less than 0.2 orders of magnitude as the number of PCs are varied. Again we select the PC with lowest sum of PRESS values (36) as the optimal number for the model. Predicted concentrations are 0.94 mg/mL and 1.09 mg/mL. The minimum sum of PRESS does not return a minima in the RSS plot, confirming that this preprocessing technique is inappropriate for the data set.

With our method we seek to contribute a tool which facilitates the most accurate PCR model available; we have shown in figures 7.2 and 7.4 that we can exclude these preprocessing treatments due to their PRESS matrices' lack of statistical significance, which manifests as a model that does not perform well when extended to new spectra. Existing techniques allow the operator to test and assess many preprocessing treatments, but the results do not provide any measure of the PCR model's performance when extended to future spectra. Statistical analysis using our method gives the user this extra information; current decisions about preprocessing method suitability lack the assurance factor that we can provide.

7.3 Biofluid Composition Analysis

A set of spectra for each phantom biofluid were collected using the microfluidic device with a TCT waveguide, in order to demonstrate proof of concept: reasonable signal enhancement, ease of collection, and statistical optimization of the predictive model. For each unique phantom tested, we plot the prediction of the most optimal preprocessing method identified by our algorithm. Appendix B lists all preprocessing treatments which were compared. Optimal preprocessing methods and PC choices for each unknown spectrum were selected with the process outlined below:

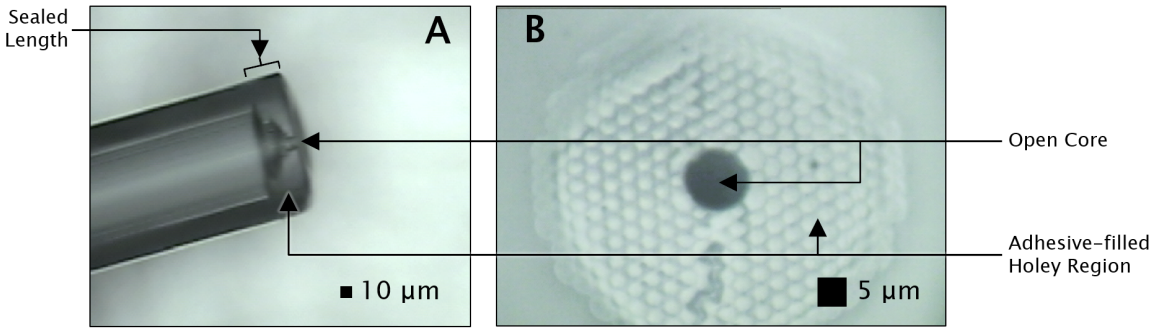

Figure 7.5: Hollow-core photonic crystal fiber (HC-PCF) with adhesive-filled holey region and open core. (A) Side view of the sealed fiber viewed with a 10× lens. (B) Fiber tip viewed with a 100× lens

- Determine all preprocessing techniques which produce statistical significance
- Identify the optimal number of PCs for each significant preprocessing method
- Select the preprocessing method with the lowest RSS value when PCR is performed with the optimal number of PCs. This step may also be applied to cross-validation results of a single analyte if other analytes are of no interest.

Photonic Crystal Fiber Optofluidic Integration

To demonstrate further spectrum enhancement than what may be obtained with a TCT microfluidic device, each simulated human tear sample was collected once again with a HC-PCF microfluidic device. The majority of these spectra were collected by an operator with limited knowledge of the experiment and expected spectra. Optofluidic integration of HC-PCF (HC-1060, NKT Photonics via Thorlabs) required the development of a technique which restricts the fluid from entering the holey region of both ends of the fiber while simultaneously maintaining laser guiding in the fluid-filled core. This process has been developed by Duxuan Wu and will be thoroughly discussed in her upcoming thesis [103]. In brief, this is accomplished by two means.

1. Holey region of the first HC-PCF end is sealed by bringing the tip into contact with a small volume of ultraviolet-curable adhesive (NOA 68T, Norland Products Inc.), followed by a burst of air delivered through the second fiber end via syringe. This procedure drives adhesive out of the core, while retaining a thin layer in the holey region. The adhesive is cured with a tabletop ultraviolet lamp.
2. The holey region of the fiber's second end is collapsed by heat using an arc fusion splicer. This procedure collapses the silica walls of the HC-PCF holey region before the core because the larger relative diameter in the core slows arc heat transfer [104].

We routinely achieve adhesive-sealed lengths below 30 μm using this method; lengths below 20 μm are readily attainable with a small amount of practice. Figure 7.5 shows a HC-PCF with adhesive-filled holey region.

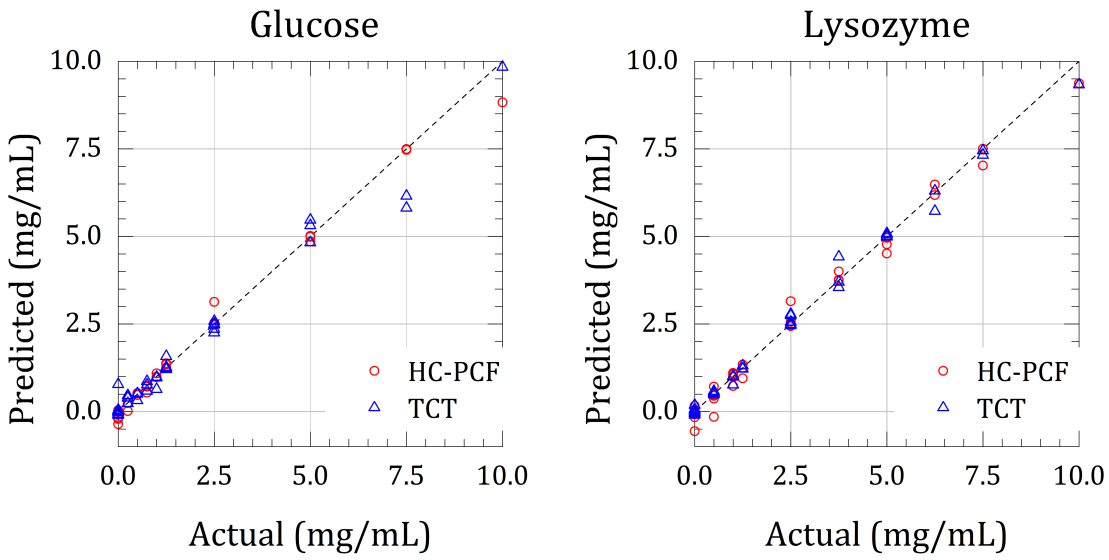

Figure 7.6: Best-performing principal component regression (PCR) prediction results compared to true concentration for 40 artificial tear solutions. Our statistical significance algorithm acting on an independent cross-validation data set is used to optimize the preprocessing method and number of principal components (PCs) for each analyte individually within every sample.

Glucose and Lysozyme Predictions in Simulated Human Tears

Best-performing PCR predictions for each of the 40 samples measured by both TCT and HC-PCF are shown in figure 7.6. Our process has enabled us to obtain a median prediction error in TCTs of 0.04 mg/mL (0.2 mM) for glucose, and 0.05 mg/mL (17.2 M) for lysozyme. These error values fall below the order of magnitude on which lysozyme is physiologically relevant for herpes simplex virus determination, but tear glucose precision falls short of what is needed for diabetes monitoring [47, 98, 99]. Across every sample in this TCT data set, and each preprocessing method which was determined to produce a statistically significant model, we obtained a median error of 0.44 mg/mL (2.4 mM) for glucose and 0.70 mg/mL (241 μM) for lysozyme. Switching to HC-PCFs allows us to achieve comparable spectrum Raman enhancement with acquisition times reduced up to 80×. When spectra were collected with HC-PCF we obtain a median error of 0.02 mg/mL (0.1 mM) for glucose, and 0.06 mg/mL (20.7 μM) for lysozyme. Across all samples in this HC-PCF data set and each preprocessing method which our algorithm identified as potentially suitable, we achieve a median error of 0.33 mg/mL (1.8 mM) for glucose and 0.55 mg/mL (190 μM) for lysozyme.

Our system can reliably achieve diagnostic resolution of 0.88 mg/mL (4.8 mM) for glucose and 1.4 mg/mL (482 μM) for lysozyme with no human intervention. We are confident that the next implementation of the algorithm will automate selection between multiple preprocessing techniques which perform reasonably well, to return the method which is most suitable. This is expected to achieve diagnostic resolutions falling at or near our best-performing results which require human intervention, of 0.04 mg/mL (0.2 mM) for glucose and 0.1 mg/mL (34.4 μM) for lysozyme. The over-arching work, of which this thesis is a part, aims to extend the sensitivity of Raman in biological fluids as far as it can go and we must recognize that we will not reach this goal in one step. The developments within this thesis do not achieve the most sensitive predictions which we believe are feasible using Raman spectroscopy, but

nonetheless demonstrate diagnostic potential and a marked advantage over current methods.

Expected glucose concentrations in tears can vary substantially as a function of the collection method. Some studies report diabetic levels ranging from 0.3 to 0.9 mM, while others report the diabetic range as 1.8 to 4.9 mM [105]. As such it is difficult to absolutely quantify the minimum precision necessary for a Raman-based tear glucose sensing system. With our algorithm's current implementation's glucose resolution at 4.8 mM it can be stated that we do not achieve the accuracy necessary for diagnostics in tears. The resolution of 0.2 mM achieved with manual intervention, however, may be reasonable depending on tear collection method.

Previous studies involving Raman analysis of lysozyme concentrations in aqueous fluids via DCDRS have achieved of errors-of-detection on the order of 0.08 mg/mL (28.6 μM) or lower, similar in magnitude to our own results [30,31]. DCDRS has also been used to quantify aqueous glucose down to a minimum concentration of 0.02 mg/mL (100 μM), exceeding our results but at the high cost of sample destruction and preprocessing time [31]. DCDRS involves depositing a small volume of fluid on to a substrate, evaporating the solvent, and performing Raman spectroscopy on the residual precipitate [30]. This technique provides an enhancement upwards of 3 orders of magnitude to the Raman signal and often yields Raman spectra which resemble aqueous solutions rather than crystalline or denatured samples. It has shown to have an advantage over SERS in terms of reproducibility and stability, but not in magnitude of enhancement [31]. SERS can provide an enhancement upwards of 9 orders of magnitude versus unassisted Raman spectroscopy of aqueous samples, but the sample must be altered with nanostructures which renders it unusable for future study [35]. We have exceeded aqueous glucose errors-of-detection which have previously been reported using SERS (1.8 mM) without these necessary sample modifications [106]. Our methods have additionally demonstrated spectrum stability and reproducibility during lengthy acquisition times and waveguide modifications, further advocating the use of LCW Raman over SERS in this application.

Both sets of experiments on glucose and lysozyme achieve errors in detection which are on the same order of magnitude. The HC-PCF outperforms the TCT in terms Raman enhancement and thereby total collection time, by approximately two orders of magnitude. Figure 7.7 shows the relative Raman signals from a droplet, versus two different waveguides, versus a waveguide inside of our microfluidic device. The Raman intensity obtained from a TCT in our microfluidic device does not decay over the timeframe of spectra collection. The signal from a bare TCT, on the other hand, suffers a steady decline in intensity as the solution evaporates from the focal volume.

With our microfluidic setup a TCT can achieve similar-intensity Raman spectra to that acquired with a HC-PCF with lengthy exposure times, but this may not be an option when rapid diagnosis is essential. If the time constraint is not present then TCTs pose a great cost savings, require no waveguide preparation prior to use, and suffers no signal variation due to preparation parameters. All TCT spectra in this experiment were collected with 240 second exposure times yielding similar Raman intensities. Some intensity variation is expected due to slight coupling differences between microfluidic chips. HC-PCF spectra, on the other hand, have had their exposure times adjusted by the operator in order to compensate for fiber preparation parameters which affect its light-guiding properties. This manual intervention may be undesirable for a completely user-independent measurement and analysis system.

Following our initial statistical analysis, further investigation was carried out on all tear phantom spectra to determine the impact of assessing error using root mean square (RMS) rather than RSS. In

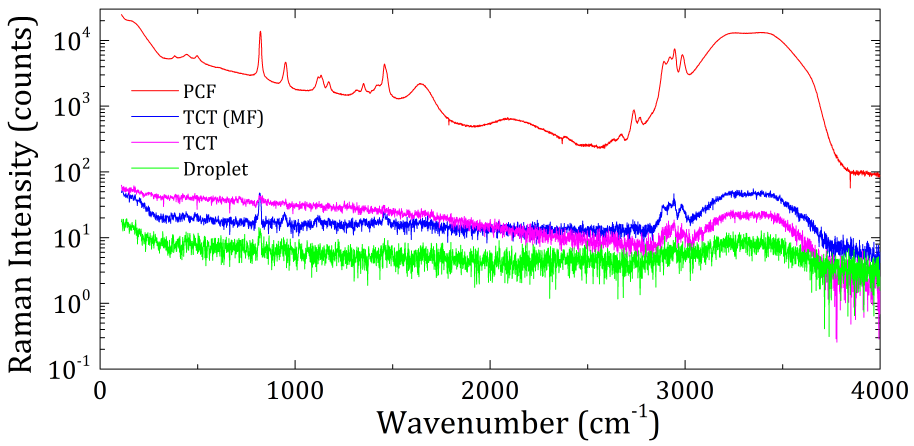

Figure 7.7: Raman spectrum enhancement method comparison. All spectra are obtained with a 1 second exposure and 5 acquisitions from a 10% isopropyl alcohol (IPA) and 90% deionized water (DIW) (% v/v). Signal intensities are plotted between Raman spectra obtained from a droplet directly, versus the enhancement provided from a 4 cm length of Teflon capillary tube (TCT) without microfluidic containment, a 4 cm length of hollow-core photonic crystal fiber (HC-PCF) without microfluidic containment (denoted PCF), and a 4 cm length of TCT with microfluidic containment, denoted TCT (MF).

each instance we determined that both RMS and RSS yielded errors in prediction and cross-validation which were not dissimilar enough to conclude that RMS should be used over RSS or vice versa at this time.

Alcohol Predictions in Simulated Whole Human Blood

Twenty-seven tertiary samples were prepared to test our system's performance within an opaque biofluid phantom mimicking whole human blood, composed of a 20% Intralipid fat emulsion with analytes IPA and DIW. Minimum analyte concentrations were 0.1% (% v/v) IPA and 1.75% DIW. Resulting predicted versus actual concentrations of IPA are illustrated in figure 7.8. Using the same technique outlined above and optimizing the model to predict for IPA yielded a median prediction error of 0.08%. Median error for all samples and each significant preprocessing method is 3.33%.

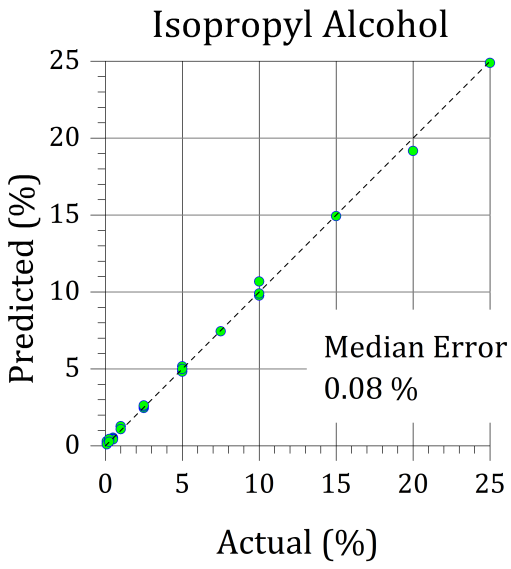

Figure 7.8: True vs predicted concentrations of isopropyl alcohol (IPA) in a 20% Intralipid emulsion, an opaque white solution which mimics the scattering properties of whole human blood. Concentration of alcohol in 27 unique samples is estimated using principal component regression (PCR), with the optimal number of principal components (PCs) determined by our statistically-based algorithm.

Chapter 8

Conclusion

8.1 Summary of Results

Biofluid analysis represents an accessible and economical alternative to clinical laboratory diagnostics. Tears, urine, blood, and saliva are all relatively easy to collect and contain a wealth of insight into a patient's well-being. Raman spectroscopy is an ideal tool for non-destructive analysis of biofluids: it performs excellently in identifying and quantifying substances in solution, and can accomplish this task without direct sample contact, or destruction. Before it can be widely adapted into point-of-care diagnostics tools we require methods which amplify the faint signal and compensate for insignificant variation between biological samples. Without these two major corrections we cannot be certain of the diagnostic relevance of that which we observe. With regards to signal enhancement: current methods either destroy or irreversibly contaminate the sample. To compensate for variation: many standard preprocessing methods are available to achieve this, but the optimal technique varies on a case-to-case basis depending on, analyte, measurement conditions, and end-user expertise. In this thesis we report noninvasive physiological monitoring for the firs time, using a combination of micro-opto-fluidics and machine-learning.

Our micro-opto-fluidic device enhances a Raman spectrum and ensures that the biofluid does not interact with environmental contaminants which may alter the spectrum, obscure analytes of interest, or affect diagnostic efficacy. Additionally, the fluidic configuration eliminates evaporation, ensuring that optimal optical coupling is maintained during prolonged measurements. Environmental confinement also plays a role in operator safety if the sample is at all pathogenic. To the best of our knowledge this is the first instance of a fully-contained microfluidic system with an integrated waveguide for enhanced Raman spectroscopy.

We employed a statistical F-test to analyze the variability within PRESS matrices of biofluid training spectra for PCR. This approach provides a confidence factor that, to the best of our knowledge, is not present in any other technique. Our algorithm is capable of determining optimal preprocessing methods, independent of the operator's experience level. The analysis technique has proven successful at identifying robustness of preprocessing techniques in two classes of artificial biofluids: a phantom of tears, and of whole human blood. The combination of LCWs and a statistical F-test to optimize the PCR model allows us to reliably predict constituent concentrations in tertiary biological phantom solutions with a sensitivity exceeding 0.1 mg/mL. We are confident that this number does not represent

a limitation of the device's sensitivity, but rather represents a step in a larger process which will bring these predictions into the realm of diagnostic relevance.

Using our techniques we achieve lysozyme ang glucose concentration predictions in human tear phantoms which fall in the range of diagnostic significance. For lysozyme this range is approximately 0 to 2.6 mM [107]. Detecting and quantifying this analyte could readily aid diagnostics for herpes simplex virus, Sjögrens syndrome, and kerato-conjunctivitis [98, 108]. Lysozyme has also been investigated as a biomarker of malaria severity; our technique has not yet reached detection levels which would suit this purpose ($<$ 760 nM) [109]. Glucose levels in human urine between healthy and diabetic patients may vary from 2.78 mM to over 5.55 mM; these concentrations could reasonably be measured using our device with a manual intervention resolution of 0.2 mM. Glucose concentrations in other biological fluids such as sweat, saliva, and ocular fluids range from 0.01 mM to 5 mM; further testing and refinement is needed in order for our system to achieve confident glucose predictions on this scale [110]. Saliva in particular warrants special consideration as a significant ($p < 0.001$) correlation has been shown between the glucose levels in blood serum and saliva in diabetic and non-diabetic patients [111]. Our technique is readily adaptable to further investigate increasingly lower concentrations to aid scientific advancement of glucose detection in tears and other human biofluids.

Our techniques allow users of all skill levels to rapidly and confidently collect spectra and optimize their data set. With these tasks simplified more efforts can be devoted to diagnosis, detection, or analysis. We propose that this method successfully satisfies the need for a dependable, automated and sufficiently generic approach for PCR; limitations due to omnipresent biological variation are automatically compensated, allowing for a marked quality increase in robust quantitative analysis of Raman biofluid spectra.

8.2 Future Work

Using an enhanced fluidic Raman technique and further algorithm optimization, we forecast that we will achieve and exceed the resolution necessary for widespread diagnostics. The performance which we present in this thesis attains mM level of precision which is sufficient for certain analytes, but we wish to push the sensitivity beyond this, into μM and below. We expect that extending this method to analyze human biofluids will bring an unavoidable set of complications. Our artificial biofluid samples were prepared from common stock solutions and as such exhibit a much greater degree of similarity than we should expect to find in human samples. Real biofluids may contain hundreds of analytes with overlapping Raman modes, and variation will be present within spectra sets due to external factors such as patient hydration. A carefully-constructed design-of-experiments is likely necessary to pre-validate certain preprocessing methods for a biofluid, to expedite the selection process. Certain preprocessing techniques are mutually exclusive: a baseline correction and derivatives preprocessing, for example, both aim to remove common backgrounds. As such it is not logical to apply these methods in sequence and we must teach the algorithm to recognize cases such as this. Quality of spectra may also be enhanced by selecting gratings which will provide us greater resolution in wavenumbers in order to cope with complex fluids where many modes are present in a narrow spectral range.

We expect that the device can reasonably be extended to a portable system in which the microfluidic chip and laser objective can be fixed relative to each other and dampened from external vibrations in a simple manner. Our isolation configuration poses a great benefit to reducing unwanted background or

environmental interference which can be prevalent in portable Raman systems [112].

Our algorithm successfully automates selection of the optimal number of PCs for a preprocessing method and eliminates unsuitable preprocessing treatments. This achieves a tremendous reduction in the number of decisions which require human intervention. Our human tear phantom cross-validation training data set of 39 spectra may form a model with up to 37 PCs for each possible preprocessing method. Twenty-eight different preprocessing treatments were assessed, resulting in 1036 possible unique predictive models. If even one preprocessing method is identified as unsuitable, we have reduced the number of decisions which require manual intervention to 27, eliminating 97.3% of cases. The future of this algorithm will fully automate preprocessing treatment selection and reduce the number of decisions which require manual intervention to zero.

Bibliography

[1] Emily E. Storey and Amr S. Helmy. Optimized Pre-processing and Machine Learning for Quantitative Raman Spectroscopy in Biology. *Journal of Raman Spectroscopy*, 2019. Accepted for publication 3 March 2019.

[2] Emily E. Storey, Duxuan X. Wu, and Amr S. Helmy. Point-Of-Care Noninvasive Biofluid Diagnostics using Raman. 2019. In Preparation to Submit on or before 16 April 2019.

[3] Emily E Storey, Manuchehr Ebrahimi, Basil G Eleftheriades, Bhargava Ravoori, Steven Rutledge, Tuyen Tran, Marie Tripp, and Amr S Helmy. Semiconductor Contaminant Quantification via Raman Spectroscopy. In *Semiconductor Research Corporation (SRC) TechCon 2017*, Austin, Texas, USA, 2017.

[4] Emily E Storey, Duxuan X Wu, and Amr S Helmy. Optofluidic Analysis System with Machine Learning for User-Independent Biofluid Diagnostics. In *Conference on Lasers and Electro-Optics (CLEO) 2019*, San Jose, California, USA, 2019. Accepted to present in May 2019.

[5] Emily E Storey, Duxuan X. Wu, and Amr S Helmy. Enhanced Raman Analysis of Biofluids on Microfluidic Waveguides on Chip. In *Ontario Networking Event (ONE) in Biophysics 2018*, University of Toronto Mississauga, Ontario, Canada, 2018.

[6] Jeyse Aliana Martins Bispo, Elzo Everton de Sousa Vieira, Landulfo Silveira, and Adriana Barrinha Fernandes. Correlating the amount of urea, creatinine, and glucose in urine from patients with diabetes mellitus and hypertension with the risk of developing renal lesions by means of Raman spectroscopy and principal component analysis. *Journal of Biomedical Optics*, 18(8):087004, aug 2013.

[7] Dahu Qi and Andrew J. Berger. Chemical concentration measurement in blood serum and urine samples using liquid-core optical fiber Raman spectroscopy. *Applied Optics*, 46(10):1726, apr 2007.

[8] Jin Zhang, William Hodge, Cindy Hutnick, and Xianbin Wang. Noninvasive Diagnostic Devices for Diabetes through Measuring Tear Glucose. *Journal of Diabetes Science and Technology*, 5(1):166–172, jan 2011.

[9] Global Report on Diabetes. `https://apps.who.int/iris/handle/10665/204871`, 2016. Accessed 5 April 2019.

[10] Kenny Kong, Catherine Kendall, Nicholas Stone, and Ioan Notingher. Raman spectroscopy for medical diagnostics From in-vitro biofluid assays to in-vivo cancer detection. *Advanced Drug Delivery Reviews*, 89:121–134, jul 2015.

[11] Ewen Smith and Geoffrey Dent. *Modern Raman Spectroscopy - A Practical Approach*. John Wiley & Sons, Ltd, Chichester, UK, dec 2004.

[12] Greta Del Mistro, Silvia Cervo, Elena Mansutti, Riccardo Spizzo, Alfonso Colombatti, Pietro Belmonte, Renzo Zucconelli, Agostino Steffan, Valter Sergo, and Alois Bonifacio. Surface-enhanced Raman spectroscopy of urine for prostate cancer detection: a preliminary study. *Analytical and Bioanalytical Chemistry*, 407(12):3271–3275, may 2015.

[13] Hyangah Chon, Sangyeop Lee, Soo-Young Yoon, Eun Kyu Lee, Soo-Ik Chang, and Jaebum Choo. SERS-based competitive immunoassay of troponin I and CK-MB markers for early diagnosis of acute myocardial infarction. *Chem. Commun.*, 50(9):1058–1060, 2014.

[14] Gwénaël Gouadec and Philippe Colomban. Raman Spectroscopy of nanomaterials: How spectra relate to disorder, particle size and mechanical properties. *Progress in Crystal Growth and Characterization of Materials*, 53(1):1–56, mar 2007.

[15] R. H. Rickman and P. R. Dunstan. Enhancement of lattice defect signatures in graphene and ultrathin graphite using tip-enhanced Raman spectroscopy. *Journal of Raman Spectroscopy*, 45(1):15–21, jan 2014.

[16] Annika M K Enejder, Tae-Woong Koo, Jeankun Oh, Martin Hunter, Slobodan Sasic, Michael S Feld, and Gary L Horowitz. Blood analysis by Raman spectroscopy. *Optics Letters*, 27(22):2004, nov 2002.

[17] Jacob Filik and Nicholas Stone. Analysis of human tear fluid by Raman spectroscopy. *Analytica Chimica Acta*, 616(2):177–184, jun 2008.

[18] Elena Ryzhikova, Oleksandr Kazakov, Lenka Halamkova, Dzintra Celmins, Paula Malone, Eric Molho, Earl A Zimmerman, and Igor K Lednev. Raman spectroscopy of blood serum for Alzheimer's disease diagnostics: specificity relative to other types of dementia. *Journal of Biophotonics*, 8(7):584–596, jul 2015.

[19] Samjin Choi, Sung Woon Moon, Jae-Ho Shin, Hun-Kuk Park, and Kyung-Hyun Jin. Label-Free Biochemical Analytic Method for the Early Detection of Adenoviral Conjunctivitis Using Human Tear Biofluids. *Analytical Chemistry*, 86(22):11093–11099, nov 2014.

[20] Ming-Tse Kuo, Chi-Chang Lin, Hsin-Yu Liu, and Hsien-Chang Chang. Tear Analytical Model Based on Raman Microspectroscopy for Investigation of Infectious Diseases of the Ocular Surface. *Investigative Opthalmology & Visual Science*, 52(7):4942, jun 2011.

[21] Yujun Song, Yu-Yen Huang, Xuewu Liu, Xiaojing Zhang, Mauro Ferrari, and Lidong Qin. Point-of-care technologies for molecular diagnostics using a drop of blood. *Trends in Biotechnology*, 32(3):132–139, mar 2014.

[22] F.L. Pedrotti, L.S. Pedrotti, and L.M. Pedrotti. *Introduction to Optics*. Pearson Prentice Hall, 2007.

[23] Peter Vandenabeele. *Practical Raman spectroscopy : an introduction*. Wiley, Chichester, West Sussex, United Kingdom, 2013.

[24] Maher S Amer. Chapter 2. Raman Spectroscopy; the Diagnostic Tool. In *Raman Spectroscopy, Fullerenes and Nanotechnology*, pages 43–108. Royal Society of Chemistry, Cambridge, 2010.

[25] David J Griffiths. *Introduction to Electrodynamics*. Always learning. Pearson, 2013.

[26] Derek A Long. *The Raman effect: a unified treatment of the theory of Raman scattering by molecules. 2002*, volume 8. John Wiley & Sons, Ltd, Chichester, UK, apr 2002.

[27] Gàbor Keresztury. Raman Spectroscopy: Theory. In John M. Chalmers, editor, *Handbook of Vibrational Spectroscopy*. John Wiley & Sons, Ltd, Chichester, UK, aug 2006.

[28] Alois Bonifacio, Silvia Cervo, and Valter Sergo. Label-free surface-enhanced Raman spectroscopy of biofluids: fundamental aspects and diagnostic applications. *Analytical and Bioanalytical Chemistry*, 407(27):8265–8277, nov 2015.

[29] Christy L Haynes, Chanda Ranjit Yonzon, Xiaoyu Zhang, and Richard P Van Duyne. Surface-enhanced Raman sensors: early history and the development of sensors for quantitative biowarfare agent and glucose detection. *Journal of Raman Spectroscopy*, 36(6-7):471–484, jun 2005.

[30] Jacob Filik and Nicholas Stone. Drop coating deposition Raman spectroscopy of protein mixtures. *The Analyst*, 132(6):544, may 2007.

[31] Dongmao Zhang, Yong Xie, Melissa F Mrozek, Corasi Ortiz, V Jo Davisson, and Dor Ben-Amotz. Raman Detection of Proteomic Analytes. *Analytical Chemistry*, 75(21):5703–5709, nov 2003.

[32] D. Brutin, B. Sobac, B. Loquet, and J. Sampol. Pattern formation in drying drops of blood. *Journal of Fluid Mechanics*, 667:85–95, jan 2011.

[33] James M. Cameron, Holly J. Butler, David S. Palmer, and Matthew J. Baker. Biofluid spectroscopic disease diagnostics: A review on the processes and spectral impact of drying. *Journal of Biophotonics*, 11(4):e201700299, apr 2018.

[34] W. Bou Zeid and D. Brutin. Influence of relative humidity on spreading, pattern formation and adhesion of a drying drop of whole blood. *Colloids and Surfaces A: Physicochemical and Engineering Aspects*, 430:1–7, aug 2013.

[35] Jacky S.W. Mak, Steve A Rutledge, Rashid M Abu-Ghazalah, Fatemeh Eftekhari, Juan Irizar, Natalie C.M. Tam, Gang Zheng, and Amr S Helmy. Recent developments in optofluidic-assisted Raman spectroscopy. *Progress in Quantum Electronics*, 37(1):1–50, jan 2013.

[36] Gianluca Persichetti and Romeo Bernini. Water monitoring by optofluidic Raman spectroscopy for in situ applications. *Talanta*, 155:145–152, aug 2016.

[37] The Chemours Company. Teflon AF Product Information. `https://www.chemours.com/Teflon_Industrial/en_US/assets/downloads/teflon-af-product-information.pdf`, 2016. Accessed 5 April 2019.

[38] Robert Altkorn, Michelle Duval Malinsky, Richard P Van Duyne, and Ilia Koev. Intensity Considerations in Liquid Core Optical Fiber Raman Spectroscopy. *Applied Spectroscopy*, 55(4):373–381, apr 2001.

[39] Fatemeh Eftekhari, Juan Irizar, Laila Hulbert, and Amr S Helmy. A comparative study of Raman enhancement in capillaries. *Journal of Applied Physics*, 109(11):113104, jun 2011.

[40] Steven L. Jacques and Brian W. Pogue. Tutorial on diffuse light transport. *Journal of Biomedical Optics*, 13(4):041302, 2008.

[41] Steven Rutledge. Post Synthesis Rapid Thermal Annealing and Characterization of Colloidal Nanoparticles. Masters of applied science, University of Toronto, 2009.

[42] Matthew Barker and William Rayens. Partial least squares for discrimination. *Journal of Chemometrics*, 17(3):166–173, mar 2003.

[43] William L Clarke, Daniel Cox, Linda A Gonder-Frederick, William Carter, and Stephen L Pohl. Evaluating Clinical Accuracy of Systems for Self-Monitoring of Blood Glucose. *Diabetes Care*, 10(5):622–628, sep 1987.

[44] Andrew J Berger, Tae-Woong Koo, Irving Itzkan, Gary Horowitz, and Michael S Feld. Multicomponent blood analysis by near-infrared Raman spectroscopy. *Applied Optics*, 38(13):2916, may 1999.

[45] Martin Prince, Renata Bryce, Emiliano Albanese, Anders Wimo, Wagner Ribeiro, and Cleusa P Ferri. The global prevalence of dementia: A systematic review and metaanalysis. *Alzheimer's & Dementia*, 9(1):63–75.e2, jan 2013.

[46] Aisling M. Mann and Brian J. Tighe. Tear analysis and lenstear interactions. *Contact Lens and Anterior Eye*, 30(3):163–173, jul 2007.

[47] Jacob Filik and Nicholas Stone. Investigation into the protein composition of human tear fluid using centrifugal filters and drop coating deposition Raman spectroscopy. *Journal of Raman Spectroscopy*, 40(2):218–224, feb 2009.

[48] Wan-Sun Kim, Jae-Ho Shin, Hun-Kuk Park, and Samjin Choi. A low-cost, monometallic, surface-enhanced Raman scattering-functionalized paper platform for spot-on bioassays. *Sensors and Actuators B: Chemical*, 222:1112–1118, jan 2016.

[49] W Ranjith Premasiri, Richard H Clarke, and M Edward Womble. Urine analysis by laser Raman spectroscopy. *Lasers in Surgery and Medicine*, 28(4):330–334, apr 2001.

[50] Na Chen, Ming Rong, Xiaoguang Shao, Heng Zhang, Shupeng Liu, Baijun Dong, Wei Xue, Tingyun Wang, Taihao Li, and Jiahua Pan. Surface-enhanced Raman spectroscopy of serum accurately detects prostate cancer in patients with prostate-specific antigen levels of 4–10 ng/mL. *International Journal of Nanomedicine*, Volume 12:5399–5407, jul 2017.

[51] Silvia Chiappin, Giorgia Antonelli, Rosalba Gatti, and Elio F De Palo. Saliva specimen: A new laboratory tool for diagnostic and basic investigation. *Clinica Chimica Acta*, 383(1-2):30–40, aug 2007.

[52] Muhammad Ashraf Nazir. Prevalence of periodontal disease, its association with systemic diseases and prevention. *International journal of health sciences*, 11(2):72–80, 2017.

[53] Eliaz Kaufman and Ira B Lamster. Analysis of saliva for periodontal diagnosis. A review. *Journal of Clinical Periodontology*, 27(7):453–465, jul 2000.

[54] Suk Ji and Youngnim Choi. Point-of-care diagnosis of periodontitis using saliva: technically feasible but still a challenge. *Frontiers in Cellular and Infection Microbiology*, 5:65, sep 2015.

[55] S Gonchukov, A Sukhinina, D Bakhmutov, T Biryukova, M Tsvetkov, and V Bagratashvily. Periodontitis diagnostics using resonance Raman spectroscopy on saliva. *Laser Physics Letters*, 10(7):075610, jul 2013.

[56] Marina Borro, Andrea Botticelli, Federica Mazzuca, Elisa Concetta Onesti, Giovanna Gentile, Adriana Romiti, Bruna Cerbelli, Eva Mazzotti, Luca Marchetti, Luana Lionetto, Maurizio Simmaco, and Paolo Marchetti. Pre-treatment assay of 5-fluorouracil degradation rate (5-FUDR) to improve prediction of 5-fluorouracil toxicity in gastro-esophageal cancer. *Oncotarget*, 8(8):14050–14057, feb 2017.

[57] Stuart Farquharson, Alan D Gift, Chetan Shende, Paul Maksymiuk, Frank E Inscore, and John Murran. Detection of 5-fluorouracil in saliva using surface-enhanced Raman spectroscopy. *Vibrational Spectroscopy*, 38(1-2):79–84, jul 2005.

[58] Stuart Farquharson, Alan Gift, Chetan Shende, Frank Inscore, Beth Ordway, Carl Farquharson, and John Murren. Surface-enhanced Raman Spectral Measurements of 5-Fluorouracil in Saliva. *Molecules*, 13(10):2608–2627, oct 2008.

[59] PDQ Supportive and Palliative Care Editorial Board. Oral Complications of Chemotherapy and Head/Neck Radiation (PDQ®): Patient Version, 2002.

[60] George M. Whitesides. The origins and the future of microfluidics. *Nature*, 442(7101):368–373, jul 2006.

[61] Thomas Sanladerer. Building the cheapest possible prusa i3 mk2 clone: [02] frame and motion! `https://youtu.be/J6_z0YMhYdM?t=663`. Accessed 5 April 2019.

[62] Ian T Jolliffe and Jorge Cadima. Principal component analysis: a review and recent developments. *Philosophical Transactions of the Royal Society A: Mathematical, Physical and Engineering Sciences*, 374(2065):20150202, apr 2016.

[63] Paul Geladi and Bruce R Kowalski. Partial least-squares regression: a tutorial. *Analytica Chimica Acta*, 185(C):1–17, 1986.

[64] I.T. Jolliffe. *Principal Component Analysis (Springer Series in Statistics)*. Springer, 2002.

[65] M Andrecut. Parallel GPU Implementation of Iterative PCA Algorithms. *Journal of Computational Biology*, 16(11):1593–1599, nov 2009.

[66] Svante Wold, Kim Esbensen, and Paul Geladi. Principal component analysis. *Chemometrics and Intelligent Laboratory Systems*, 2(1-3):37–52, aug 1987.

[67] Roozbeh Razavi-Far, Enrico Zio, and Vasile Palade. Efficient residuals pre-processing for diagnosing multi-class faults in a doubly fed induction generator, under missing data scenarios. *Expert Systems with Applications*, 41(14):6386–6399, oct 2014.

[68] Martin Andersson. A comparison of nine PLS1 algorithms. *Journal of Chemometrics*, 23(10):518–529, oct 2009.

[69] C M Andersen and R Bro. Variable selection in regression-a tutorial. *Journal of Chemometrics*, 24(11-12):728–737, nov 2010.

[70] R Bro, K Kjeldahl, A K Smilde, and H A L Kiers. Cross-validation of component models: A critical look at current methods. *Analytical and Bioanalytical Chemistry*, 390(5):1241–1251, mar 2008.

[71] Li Wang, Hongzhi Liu, Li Liu, Qiang Wang, Shurong Li, and Qizhai Li. Prediction of peanut protein solubility based on the evaluation model established by supervised principal component regression. *Food Chemistry*, 218:553–560, mar 2017.

[72] Srujana Adusumilli, Deepak Bhatt, Hong Wang, Vijay Devabhaktuni, and Prabir Bhattacharya. A novel hybrid approach utilizing principal component regression and random forest regression to bridge the period of GPS outages. *Neurocomputing*, 166:185–192, oct 2015.

[73] M Zeaiter, J.-M. Roger, and V Bellon-Maurel. Robustness of models developed by multivariate calibration. Part II: The influence of pre-processing methods. *TrAC Trends in Analytical Chemistry*, 24(5):437–445, may 2005.

[74] Jan Gerretzen, Ewa Szymańska, Jeroen J. Jansen, Jacob Bart, Henk-Jan van Manen, Edwin R. van den Heuvel, and Lutgarde M. C. Buydens. Simple and Effective Way for Data Preprocessing Selection Based on Design of Experiments. *Analytical Chemistry*, 87(24):12096–12103, dec 2015.

[75] Philip Heraud, Bayden R Wood, John Beardall, and Don McNaughton. Effects of pre-processing of Raman spectra onin vivo classification of nutrient status of microalgal cells. *Journal of Chemometrics*, 20(5):193–197, may 2006.

[76] Q Guo, W Wu, and D.L Massart. The robust normal variate transform for pattern recognition with near-infrared data. *Analytica Chimica Acta*, 382(1-2):87–103, feb 1999.

[77] J.T. McClave and T.T. Sincich. *Statistics*. Pearson Education, 2012.

[78] Rasmus Bro and Age K Smilde. Centering and scaling in component analysis. *Journal of Chemometrics*, 17(1):16–33, jan 2003.

[79] Mary Beth Seasholtz and Bruce R Kowalski. The effect of mean centering on prediction in multivariate calibration. *Journal of Chemometrics*, 6(2):103–111, mar 1992.

[80] Abraham Savitzky and M. J. E. Golay. Smoothing and Differentiation of Data by Simplified Least Squares Procedures. *Analytical Chemistry*, 36(8):1627–1639, jul 1964.

[81] Per Waaben Hansen. Pre-processing method minimizing the need for reference analyses. *Journal of Chemometrics*, 15(2):123–131, feb 2001.

[82] Giancarlo Diana and Chiara Tommasi. Cross-validation methods in principal component analysis: A comparison. *Statistical Methods & Applications*, 11(1):71–82, feb 2002.

[83] Jianhua Zhao, Haishan Zeng, Sunil Kalia, and Harvey Lui. Wavenumber selection based analysis in Raman spectroscopy improves skin cancer diagnostic specificity. *Analyst*, 141(3):1034–1043, 2016.

[84] Michel J Anzanello, Rafael S Ortiz, Renata Limberger, and Kristiane Mariotti. PLS-DA wavenumber selection for the categorization of medicine samples based on multiple criteria. *Forensic Science International*, 242:111–116, sep 2014.

[85] Roger M. Jarvis and Royston Goodacre. Genetic algorithm optimization for pre-processing and variable selection of spectroscopic data. *Bioinformatics*, 21(7):860–868, apr 2005.

[86] Jianhua Zhao, Harvey Lui, David I. McLean, and Haishan Zeng. Automated Autofluorescence Background Subtraction Algorithm for Biomedical Raman Spectroscopy. *Applied Spectroscopy*, 61(11):1225–1232, nov 2007.

[87] Juan José González-Vidal, Rosanna Pérez-Pueyo, and María José Soneira. Automatic morphology-based cubic p-spline fitting methodology for smoothing and baseline-removal of Raman spectra. *Journal of Raman Spectroscopy*, 48(6):878–883, jun 2017.

[88] N.K. Lünsdorf and J.O. Lünsdorf. Evaluating Raman spectra of carbonaceous matter by automated, iterative curve-fitting. *International Journal of Coal Geology*, 160-161:51–62, apr 2016.

[89] MicroChem. SU-8 2000 Permanent Epoxy Negative Photoresist Processing Guidelines. `https://microchem.com/pdf/SU-82000DataSheet2000_5thru2015Ver4.pdf`. Accessed 5 April 2019.

[90] Anthony Grimes, David N Breslauer, Maureen Long, Jonathan Pegan, Luke P Lee, and Michelle Khine. Shrinky-Dink microfluidics: rapid generation of deep and rounded patterns. *Lab Chip*, 8(1):170–172, 2008.

[91] Dow Chemical Company. SYLGARD 184 Silicone Elastomer. `https://consumer.dow.com/content/dam/dcc/documents/en-us/productdatasheet/11/11-31/11-3184-sylgard-184-elastomer.pdf`, 2017. Accessed 5 April 2019.

[92] Khalil Khanafer, Ambroise Duprey, Marty Schlicht, and Ramon Berguer. Effects of strain rate, mixing ratio, and stressstrain definition on the mechanical behavior of the polydimethylsiloxane (PDMS) material as related to its biological applications. *Biomedical Microdevices*, 11(2):503–508, apr 2009.

[93] Aung K. Soe and Saeid Nahavandi. Degassing a PDMS mixture without a vacuum desiccator or a laboratory centrifuge and curing the PDMS chip in an ordinary kitchen oven Chips and Tips, 2011.

[94] David C. Duffy, J. Cooper McDonald, Olivier J. A. Schueller, and George M. Whitesides. Rapid Prototyping of Microfluidic Systems in Poly(dimethylsiloxane). *Analytical Chemistry*, 70(23):4974–4984, dec 1998.

[95] Elveflow. Corona plasma treater for PDMS bonding. `https://www.elveflow.com/microfluidic-flow-control-products/soft-lithography-products/corona-plasma-treater-for-pdms-bonding/`, 2019. Accessed 5 April 2019.

[96] Edmund R Malinowski. StatisticalF-tests for abstract factor analysis and target testing. *Journal of Chemometrics*, 3(1):49–60, jan 1989.

[97] Richard B Keithley, Regina M Carelli, and R Mark Wightman. Rank Estimation and the Multivariate Analysis of in Vivo Fast-Scan Cyclic Voltammetric Data. *Analytical Chemistry*, 82(13):5541–5551, jul 2010.

[98] E Eylan, D Ronen, A Romano, and O Smetana. Lysozyme tear level in patients with herpes simplex virus eye infection. *Investigative ophthalmology & visual science*, 16(9):850–3, sep 1977.

[99] D K Sen and G S Sarin. Tear glucose levels in normal people and in diabetic patients. *British Journal of Ophthalmology*, 64(9):693–695, sep 1980.

[100] K. M. Daum and R. M. Hill. Human tear glucose. *Investigative Ophthalmology and Visual Science*, 22(4):509–514, 1982.

[101] Nienke Bosschaart, Gerda J. Edelman, Maurice C. G. Aalders, Ton G. van Leeuwen, and Dirk J. Faber. A literature review and novel theoretical approach on the optical properties of whole blood. *Lasers in Medical Science*, 29(2):453–479, mar 2014.

[102] Rene Michels, Florian Foschum, and Alwin Kienle. Optical properties of fat emulsions. *Optics Express*, 16(8):5907, apr 2008.

[103] Duxuan Wu. Title To Be Announced. Masters of applied science, University of Toronto, 2019. Unpublished.

[104] Limin Xiao, Wei Jin, M S Demokan, Hoi L Ho, Yeuk L Hoo, and Chunliu Zhao. Fabrication of selective injection microstructured optical fibers with a conventional fusion splicer. *Optics Express*, 13(22):9014, 2005.

[105] N. J. van Haeringen and E. Glasius. Collection method dependant concentrations of some metabolites in human tear fluid, with special reference to glucose in hyperglycaemic conditions. *Albrecht von Graefes Archiv für Klinische und Experimentelle Ophthalmologie*, 202(1):1–7, 1977.

[106] Karen E Shafer-Peltier, Christy L Haynes, Matthew R Glucksberg, and Richard P Van Duyne. Toward a Glucose Biosensor Based on Surface-Enhanced Raman Scattering. *Journal of the American Chemical Society*, 125(2):588–593, jan 2003.

[107] Yoshiki Ohashi, Murat Dogru, and Kazuo Tsubota. Laboratory findings in tear fluid analysis. *Clinica Chimica Acta*, 369(1):17–28, jul 2006.

[108] Peter T Janssen and O.Paul van Bijsterveld. The relations between tear fluid concentrations of lysozyme, tear-specific prealbumin and lactoferrin. *Experimental Eye Research*, 36(6):773–779, jun 1983.

[109] Mauro Prato, Manuela Polimeni, and Vivian Tullio. Human Lysozyme in Malaria Patients: Possible Role as Biomarker for Disease Severity. In *Human and Mosquito Lysozymes*, pages 83–90. Springer International Publishing, Cham, 2015.

[110] Danielle Bruen, Colm Delaney, Larisa Florea, and Dermot Diamond. Glucose Sensing for Diabetes Monitoring: Recent Developments. *Sensors*, 17(8):1866, aug 2017.

[111] Shruti Gupta, Simarpreet Virk Sandhu, Himanta Bansal, and Deepti Sharma. Comparison of Salivary and Serum Glucose Levels in Diabetic Patients. *Journal of Diabetes Science and Technology*, 9(1):91–96, jan 2015.

[112] Luis Fermín Capitán-Vallvey and Alberto J. Palma. Recent developments in handheld and portable optosensingA review. *Analytica Chimica Acta*, 696(1-2):27–46, jun 2011.

Appendix A

Simulated Biofluid Compositions

Table A.1: Composition of intralipid-based samples designed to mimic the optical properties of whole human blood

Sample Number	Concentration (% v/v)		
	Intralipid	IPA	DIW
1	65	25	10
2	75	20	5
3	80	15	5
4	90	10	0
5	85	10	5
6	80	10	10
7	90	7.5	2.5
8	95	5	0
9	90	5	5
10	85	5	10
11	80	5	15
12	75	5	20
13	97.5	2.5	0
14	95	2.5	2.5
15	92.5	2.5	5
16	99	1	0
17	95	1	4
18	90	1	9
19	99.5	0.5	0
20	95	0.5	4.5
21	90	0.5	9.5
22	99.75	0.25	0
23	98	0.25	1.75
24	95	0.25	4.75
25	99.9	0.1	0
26	98	0.1	1.9
27	95	0.1	4.9

Table A.2: Composition of samples designed to mimic human tears

Sample Number	**Concentration in DIW (mg/mL)**	
	Glucose	**Lysozyme**
1	10	0
2	5	0
3	0	0
4	5	5
5	0	5
6	0	10
7	7.5	0
8	2.5	0
9	7.5	2.5
10	5	2.5
11	2.5	2.5
12	0	2.5
13	2.5	5
14	2.5	7.5
15	0	7.5
16	1.25	0
17	2.5	1.25
18	1.25	1.25
19	0	1.25
20	1.25	2.5
21	2.5	3.75
22	1.25	3.75
23	0	3.75
24	1.25	5
25	1.25	6.25
26	0	6.25
27	1	0
28	0.75	0
29	0.5	0
30	0.25	0
31	1	0.5
32	0.75	0.5
33	0.5	0.5
34	0.25	0.5
35	0	0.5
36	1	1
37	0.75	1
38	0.5	1
39	0.25	1
40	0	1

Appendix B

Preprocessing Methods

1. Raw spectra
2. Standard Normal Variate transform
3. Mean-centered
4. First Derivative
5. Second Derivative
6. Third Derivative
7. Savitzky-Golay Smoothing (window 75 points, polynomial order 3)
8. Savitzky-Golay Smoothing (window 75 points, polynomial order 3), Standard Normal Variate transform
9. Savitzky-Golay Smoothing (window 75 points, polynomial order 3), Mean-centering
10. Savitzky-Golay Smoothing (window 75 points, polynomial order 3), First Derivative
11. Savitzky-Golay Smoothing (window 75 points, polynomial order 3), Second Derivative
12. Savitzky-Golay Smoothing (window 75 points, polynomial order 3), Third Derivative
13. Baseline removed
14. Baseline removed, Standard Normal Variate transform
15. Baseline removed, Mean-centered
16. De-spiked (window 10 points)
17. Baseline removed, Savitzky-Golay Smoothing (window 75 points, polynomial order 3)
18. Baseline removed, De-spiked (window 10 points)
19. Robust Normal Variate transform (50th percentile)
20. Robust Normal Variate transform (75th percentile)
21. Robust Normal Variate transform (85th percentile)
22. Robust Normal Variate transform (90th percentile)
23. Robust Normal Variate transform (95th percentile)
24. Baseline removed, Robust Normal Variate transform (50th percentile)
25. Baseline removed, Robust Normal Variate transform (75th percentile)
26. Baseline removed, Robust Normal Variate transform (85th percentile)
27. Baseline removed, Robust Normal Variate transform (90th percentile)
28. Baseline removed, Robust Normal Variate transform (95th percentile)